Photocatalytic Degradation of Plant-generated Ethylene over Titanium Dioxide Thin Films

Kinetic Modelling and Photoreactor Design

Stroe, Rodica Elisabeta

Publication date:
2020

Document Version
Publisher's PDF, also known as Version of record

PHOTOCATALYTIC DEGRADATION OF PLANT-GENERATED ETHYLENE OVER TITANIUM DIOXIDE THIN FILMS

KINETIC MODELLING AND PHOTOREACTOR DESIGN

BY
RODICA – ELISABETA STROE

DISSERTATION SUBMITTED 2020

AALBORG UNIVERSITY
DENMARK

PHOTOCATALYTIC DEGRADATION OF PLANT-GENERATED ETHYLENE OVER TITANIUM DIOXIDE THIN FILMS

KINETIC MODELLING AND PHOTOREACTOR DESIGN

by

Rodica – Elisabeta Stroe

AALBORG UNIVERSITY
DENMARK

Dissertation submitted 2020

Dissertation submitted: January 2020

PhD supervisor: Professor Lasse A. Rosendahl,
Aalborg University

PhD committee: Associate Professor Thomas Condra (chairman)
Aalborg University

Professor Bengt Andersson
Chalmers University of Technology

Prof.Dr.ir. Philippe Heynderickx
Ghent University, Incheon Global Campus

PhD Series: Faculty of Engineering and Science,
Aalborg University

Department: Department of Energy Technology

ISSN (online): 2446-1636
ISBN (online): 978-87-7210-589-5

Published by:
Aalborg University Press
Langagervej 2
DK – 9220 Aalborg Ø
Phone: +45 99407140
aauf@forlag.aau.dk
forlag.aau.dk

Printed in Denmark by Rosendahls, 2020

TO MY PARENTS

AND

GRANDPARENTS

For the way they raised me, and the love they gave me

ENGLISH SUMMARY

This thesis addressed the possibility of employing the UV-A-mediated oxidation of volatile organic compounds (VOCs) over titanium dioxide (TiO_2) thin films for controlling the levels of ethylene (C_2H_4) in the postharvest industry. An intrinsic hormone of fruits, vegetables and flowers, C_2H_4 can quickly shift to being a pollutant, as its presence in concentrations above a certain threshold accelerates their degradation. Thus, it possesses the ability of minimizing their shelf life and substantially contributing to food loss and waste. The photocatalytic degradation of C_2H_4 over TiO_2 thin films has been kinetically studied and a photoreactor has been designed and investigated for oxidizing low levels of C_2H_4.

According to the Food and Agriculture Organization (FAO), one-third of the food produced for human consumption, on a weight basis, is either lost or wasted, on a global scale. Food loss is multifaceted, being specific to the different regions of the world and varying across the whole food supply chain and commodity types, while leading to substantial economic, environmental and even social impacts. Regardless of origin and location, in a society, where one in nine people is undernourished, the fact that 1.3 billion tons of food never make it to the plate is tragic.

The postharvest industry being the main target, case studies have been set up in the form of measurement campaigns conducted in both a typical Danish storage facility and a transportation truck, where fresh produce were stored and transported, respectively. Data collected showed that C_2H_4 concentrations range from 0.5 to 1.5 ppm, values dictated by types of stored commodities, working shifts and amount of produce. Research studies have shown that C_2H_4 sensitivity levels, although commodity-specific, are high for the majority of perishables, resulting in degradation signs even at C_2H_4 levels as low as 0.01 ppm. Thus, it can be concluded, based on the measurement campaigns, that controlling C_2H_4 in the final stages of the cold chain can prolong the shelf life of fresh produce and flowers. In addition, these campaigns set a good baseline for subsequent kinetic studies and photoreactor design.

Several substrate candidates with different TiO_2 coating thicknesses were evaluated in terms of photocatalytic activity, while observing the resulted morphological structure, with the purpose of selecting the appropriate catalyst for oxidizing C_2H_4. A kinetic analysis was carried out experimentally in a batch reactor, deriving kinetic parameters, which enabled the implementation of the reaction in a Computational Fluid Dynamics (CFD) simulation. Moreover, it was desired to couple the kinetics to the species and radiation transport. Therefore, the reaction was monitored under varying conditions of C_2H_4 concentration and incident surface radiation.

Reactor design options were discussed and design criteria were decided upon, focusing on enhancing the conversion through maximizing radiation distribution and

the contact of pollutant species with active surfaces via turbulent mixing. A full-scale 3D CAD model is presented. This was employed for two purposes: manufacturing the prototype of the reactor and conducting parametric studies through CFD. A comprehensive model was set up, including fluid flow under turbulent regime, species transport with surface reaction and radiation transport. The simulation case studies were compared in terms of turbulent mixing, radiation distribution, residence time and conversion.

DANSK RESUME

I denne afhandling adresseres muligheden for at benytte UV-A-medieret oxidation af flygtige organiske stoffer over tynde film af titanium dioxide (TiO_2) til at kontrollere mængden af ethylene (C_2H_4) i postharvest industry. C_2H_4, et intrinsic hormon fra frugt, grønsager og blomster, kan være en forurenende agent i industrien, da tilstedeværelsen over en vis koncentrations, kan accelerere nedbrydningen. Dette betyder, at hormonet potentielt kan forkorte holdbarheden på frugt, grønsager og blomster og herved bidrage væsentligt til madspild. Fotokatalytisk nedbrydning af C_2H_4 over tynde film af titanium dioxide (TiO_2) er en mulig måde hvorpå koncentrationen af hormonet kan reduceres, og kan studeres kinetisk. I denne afhandling er en fotoreaktor blevet designet, og dens evne til at oxidere lave mængder af C_2H_4 undersøgt.

Ifølge Fødevare- og Landbrugsorganisationen (FAO) er en tredjedel (baseret på vægt) af fødevarer på verdensplan, der er produceret til forbrugsmarkedet enten tabt eller spildt. Madspild er kompleks, idet det er specifikt for de forskellige regioner i verden og som varierer i hele forsyningskæden af fødevarer og varetyper, mens det medfører betydelige økonomiske, miljømæssige og endda samfundsmæssige virkninger. Det er tragisk at i venden, hvor en ud af ni er underernæret, er der 1,3 milliarder ton mad aldrig kommer på tallerkenen.

Da postharvest industry er det vigtigste mål, der er oprettet casestudier i form af målekampagner, som blev gennemført i et typisk dansk lagerfacilitet og en lastbil, hvor ferske varer blev opbevaret og transporteret. De indsamlede data viste, at C_2H_4-koncentrationer varierede fra 0,5 til 1,5 ppm, værdier dikteret af de forskellige typer af råvarer, arbejdsskift og mængden af produkter. Forskningsundersøgelser har vist, at C_2H_4-følsomhedsniveauet, selvom den er varespecifik, er høj for størstedelen af letfordærvelige ting, hvilket resulterer i nedbrydningstegn, selv ved C_2H_4-niveauer helt ned til 0,01 ppm. Det kan således konkluderes, baseret på målekampagnerne, at kontrol af C_2H_4 i de sidste stadier af den kolde kæde kan forlænge holdbarheden af friske produkter og blomster. Derudover gav disse kampagner en god basis for efterfølgende kinetiske undersøgelser og fotoreaktordesign.

Flere substratkandidater med forskellige TiO_2-coatingtykkelser blev i denne afhandling evalueret på baggrund af fotokatalytisk aktivitet, imens resultatet af den morfologiske struktur blev monitoreret med det formål at vælge den passende katalysator til oxidation af C_2H_4. En kinetisk analyse blev udført eksperimentelt i en batchreaktor, hvorved kinetiske parametre blev afledt, hvilket muliggjorde implementeringen af reaktionen i en Computational Fluid Dynamics (CFD) simulering. Derudover ønskedes det at parre kinetikken til arten og strålingstransport.

Derfor blev reaktionen overvåget under forskellige betingelser med C_2H_4-koncentration og indfaldende overfladestråling.

Reaktordesignmuligheder blev diskuteret, og designkriterier blev besluttet, hvor der blev fokuseret på at øge omdannelsen gennem maksimal strålefordeling og kontakt af forurenende arter med aktive overflader via turbulent blanding. En fuldskala 3D CAD-model præsenteres. Denne blev anvendt til to formål: fremstilling af reaktorens prototype og udførelse af parametriske undersøgelser gennem CFD. Der blev oprettet en omfattende model, herunder væskestrøm under turbulent regime, artstransport med overfladeaktion og strålingstransport. Simulations case-studier blev sammenlignet med hensyn til turbulent blanding, strålefordeling, opholdstid og konvertering.

THESIS DETAILS

Thesis title:	Photocatalytic Degradation of Plant-generated Ethylene over Titanium Dioxide Thin Films
PhD Student:	Rodica – Elisabeta Stroe
Supervisor:	Prof. Lasse A. Rosendahl

Some data in this thesis relies on the information from the following submitted or published papers, during the PhD period:

A. R.E. Stroe, L.A. Rosendahl, *"Kinetic study of the photocatalytic oxidation of ethylene over TiO_2 thin films"*, IOP Conf. Series: Materials Science and Engineering 628 (2019) (ISSN: 1757-899X), doi:10.1088/1757-899X/628/1/012009

B. R.E Stroe, C. L. Byg, L. A. Rosendahl, J. A. Hansen, *"Kinetic modelling of the photocatalytic degradation of fresh produce-generated C_2H_4 over TiO_2 thin films"* – under review at the international journal of Reaction Kinetics, Mechanisms and Catalysis

The results of the aforementioned papers have been orally presented at:

1. The 1st International Conference on Applied Catalysis & Chemical Engineering (ACC 2019), April 8-10, 2019, Dubai, UAE – poster presentation

2. The 4th International Conference on Energy Materials and Applications (ICEMA 2019), May 11-13, 2019, Beijing, China – 10 minutes oral presentation. Best Presentation Award

3. The 3rd International Conference on Applied Surface Science (ICASS2 019), June 17-20, 2019, Pisa, Italy – 10 minutes oral presentation

In addition, the following paper was completed during the PhD period, unrelated to the PhD project:

1. I.F. Grigoras, R.E. Stroe, I.M. Sintamarean, L.A. Rosendahl, *"Effect of biomass pretreatment on the product distribution and composition resulting from the hydrothermal liquefaction of short rotation coppice willow"*, Bioresource Technology 231 (2017), pp. 116-123, http://dx.doi.org/10.1016/j.biortech.2017.01.056

PREFACE

This dissertation was submitted to the Doctoral School of Engineering and Science at Aalborg University in partial fulfilment of the requirements for the Ph.D. degree. The work presented in this dissertation has been carried out between September 2016 and December 2019. The work was financed by the Innovation Fund Denmark, grant no. 5158-000007, as part of the large -scale project "*FRESH – Fresh produce through Reduction of Ethylene during Storage and Handling"*.

The work presented in this thesis is based on data from submitted or published papers, conference contributions, but it also contains data not yet published. Nevertheless, the thesis can stand on its own.

The thesis focuses on various aspects of the photocatalytic process investigated, rather than an in-depth study of a single sub-process. In addition, a study on the losses experienced by the postharvest industry was of interest. As part of it, direct measurement campaigns were conducted, rather than presenting data from literature. Thus, the investigation carried out focuses upon fresh produce losses in the postharvest stage of the supply chain, photocatalytic coatings, kinetic modelling, photocatalytic reactor design, and CFD modelling. Hence, a full-circle study was achieved, from problem core to potential solution.

Acknowledgements

First and foremost, I would like to thank my family for their endless support and love, and for always empowering me to trust myself.

My sincere gratitude goes to my supervisor, Lasse Rosendahl, for giving me the opportunity to be part of the FRESH project, for his guidance, positive attitude, and advice, both on a professional and personal level.

My work would not have been complete without the contributions of the FRESH partners and would like to thank the following:

- Maj Fredriksen, Sascha Louring, Christian S. Jeppesen, Casper L. Byg, and Jacob A. Hansen from the Danish Technological Institute for the fruitful meetings, for their help in conducting the storage facility measurement campaigns, for providing the experimental setup, and the catalyst.
- Umair L. Qureshi and Gustavo Kemmerich, from Blue Ocean Robotics, for their involvement in the design stage of the reactor, and for manufacturing the prototype.

- Salling Group A/S, PKM A/S, and Alex Andersen A/S for providing data on the postharvest losses recorded. Special thanks goes to Aarstiderne A/S for allowing the measurement campaigns to be conducted at their storage facility in Barrit, Denmark.

The Innovation Fund Denmark is acknowledged for their financial support.

I would like to acknowledge Ronnie Andersson for welcoming me at the Department of Chemistry and Chemical Engineering, Chalmers University of Technology. His knowledge in chemical reactor modelling and his shared CFD experience were of great help.

Special thanks goes to my colleagues at the Department of Energy Technology, in particular Karina K. Ludvigsen, Ionela Grigoras, Stelian Nasui, Tamas Kerekes, and Thomas Condra for their joyful spirit, and Ionut Vernica for sharing my sense of humour and being the best office mate one could ask for.

Last but not least, a soulful “Thank you!” goes to my friends, Ana-Cristina Vintura, Oana Tacu, Kenneth Kastaniegaard, Mircea Danalache, and Teodor Retevoi, for loving me, making me a better person, and for their continuous friendship, despite busy schedules, time, and distance.

Rodica-Elisabeta Stroe
December 2019

NOMENCLATURE

h	Planck constant, h = 6.626e-34 J·s
E	Photon energy, eV
r	Reaction rate, ppm/s
C	Concentration, ppm; kmol $m^{-3}s^{-1}$
t	Time, s
$\dot{q}$	Volumetric flow rate, cm^3/min or m^3/h
k_r	Reaction rate constant, ppm/s
K_{abs}	Adsorption equilibrium constant, ppm^{-1}
W	Catalyst weight, g
F	Molar flow rate, mol/g s
k_{app}	Apparent first order rate constant, s^{-1}
RH	Relative humidity, %
$\dot{m}$	Mass flow rate, kg/s
p	Pressure, Pa
U	Velocity magnitude, m/s
δ	Diffusion distance, cm^2
$\mathcal{D}_{AB}$	Diffusion coefficient, cm^2/s
T	Temperature, K
M	Molecular weight, g/mol
σ	Collision diameter, Å
Ω	Collision integral, dimensionless
C_0	Initial concentration of C_2H_4, ppm
I_{UV}	Surface incident UV radiation, W/m^2
R^2	Coefficient of determination, R-squared
D	Diameter, m
L	Length, m
r_r	Reaction rate of prototype reactor, ppm/min
$r_{r,adj}$	Adjusted reaction rate of prototype reactor, ppm/min
X	Conversion, [%]
P_k	Production of turbulent kinetic energy, [kg/m s^3]
$r_{r,CFD}$	Reactor reaction rate implemented in CFD model, [kmol/m^2 s]
k	Turbulent kinetic energy, [m^2/s^2]
$\boldsymbol{x}$	Direction vector
P	Pressure, [Pa]
$\boldsymbol{u}$	Velocity fluctuation vector
Pr_k, Pr_ω	Turbulent Prandtl number for k and ω, respectively, [-]
$\mathcal{D}_\omega$	Cross-diffusion term
y	Species mass fraction
S	Source term
$\vec{\boldsymbol{p}}$	Position vector
$\vec{\boldsymbol{s}}$	Direction vector
$\vec{\mathbf{s}}'$	Scattering direction vector

s	Path length, [m]
a	Absorption coefficient, [-]
n	Refractive index, [-]
I	Radiation intensity, [W/m^2]
Int	Turbulent intensity, [-]
l	Turbulent length scale, [m]
D_h	Hydraulic diameter, [m]
A_{cell}	Area of computational domain grid cell, [m^2]
V_r	Reactor volume, [m^3]
$A_{perf.plate}$	Total area of perforated plates, [m^2]
N_θ, N_ϕ	Number of polar and azimuthal angle, used for angular discretization
$N_{\theta p}$, $N_{\phi p}$	Number of pixels for solid angle discretization
y^+	Dimensionless wall distance, [-]

Greek letters

ν	Photon frequency, Hz
Φ	Heat flux, W/m
δ_c	Coating thickness, μm
τ	Residence time, [s]
γ	Power law exponent, [-]
ω	Specific dissipation rate, [1/s]
ρ	Density, [kg/m^3]
δ_{ij}	Kronecker delta
μ	Dynamic viscosity, [kg/ m s]
μ_T	Turbulent viscosity, [kg/m s]
α, β	Model constants, [-]
σ_s	Scattering coefficient, [-]
σ	Stefan-Boltzmann constant, σ = 5.672e-08 W/m^{2}K^4
Φ	Phase function, [-]
Ω	Solid angle, [rad]
θ	Polar angle, [rad]
ϕ	Azimuthal angle, [rad]
χ	Standard deviation, [-]

Acronyms

FLW	Food Loss and Waste
FSC	Food Supply Chain
FL	Food Loss
FW	Food Waste
FAO	Food and Agriculture Organization of the United Nations
GDP	Gross Domestic Product
FVC	Food Value Chain

GHG	Greenhouse gas
Eq.	Equivalents
UNFCCC	United Nations Convention on Climate Change
SDG	Sustainable Development Goal
Ind. Asia	Industrialised Asia
Veg.	Vegetables
S&SE	South and South East
SSA	Sub-Saharan Africa
SR	Starchy Roots
LA	Latin America
NA	North Africa
WA	Western Asia
CA	Central Asia
Oce.	Oceania
PHL	Postharvest losses
CA	Controlled Atmosphere
MA	Modified Atmosphere
MAP	Modified Atmosphere Packaging
VOC	Volatile Organic Compound
WP	Work Package
UV	Ultraviolet
VUV	Vacuum ultraviolet
FTIR	Fourier-Transform Infrared Spectroscopy
CFD	Computational Fluid Dynamics
LH	Langmuir-Hinshelwood
TCE	Trichloroethylene
DKK	Danish crown (currency)
BC	Boundary condition
No.	Number
SST	Shear-Stress Transport
C1	1 μm coating
C3	3 μm coating
XRD	X-ray Powder Diffraction
SEM	Scanning Electron Microscopy
ODE	Ordinary Differential Equation
PTR-MS	Proton-Transfer-Reaction Mass Spectroscopy
DOE	Design of Experiments
DOM	Discrete Ordinate Model
SST	Shear-Stress Transport
RANS	Reynolds-Averaged Navier-Stokes

Species

CO_2	Carbon Dioxide
CH_4	Methane
N_2O	Nitrous Oxide
C_2H_4	Ethylene
O_2	Oxygen
CO_2	Carbon Dioxide
H_2O	Water
$KMnO_4$	Potassium permanganate
O_3	Ozone
TiO_2	Titanium Dioxide
NO_x	Nitrogen Oxides
N_2	Nitrogen (diatomic nitrogen)
CO	Carbon Monoxide
H_2S	Hydrogen Sulphide
S	Sulphur
SO_2	Sulphur Dioxide
e^-	Electron
h^+	Electron hole
OH	Hydroxyl group
$OH^\cdot$	Hydroxyl radical
C2H4O	Ethylene Oxide
$C_2H_4OH^\cdot$	1-Hydroxyethyl radical
SnO_2	Stannic oxide
Al	Aluminium

Subscripts

s	**Surface**
in	Inlet
out	Outlet
sp	Species
n	Species placeholder
c	Coating
app	Apparent
LH	Langmuir-Hinshelwood
r	Reactor
i, j	Tensor index notation

TABLE OF CONTENTS

CHAPTER 1. INTRODUCTION

"Men came to want more than they needed, and this altered the intrinsic value of things."

John Locke
Second Treatise of Government, 1690

1.1. FOOD LOSS AND WASTE – AN ENVIRONMENTAL AND ECONOMIC HOTSPOT

Today days resources are already scarce and the situation is expected to become worse in the following years. Therefore, energy, water, and land cannot be misused, but must be valued efficiently and sustainably. Food loss and waste (FLW) represent a severe depletion of financial, technical and natural resources invested in land use, production, harvesting, handling, processing, packaging, transportation and retail of food. Food loss (FL) is defined as a quantitative and qualitative decrease in food. Its main cause is the inefficiency of the food supply chain (FSC), given by the poor infrastructure and logistics, lack of technology, deficient knowledge and management capacity of the supply chain parties, as well as no market access (1). Food waste (FW) is a component of food loss and refers, according to the Food and Agriculture Organization (FAO) of the United Nations, to *"the discarding or alternative (nonfood) use of food that is safe and nutritious for human consumption along the entire food supply chain"* (2). It has been observed throughout the years that the two components defined above differentiate themselves through their position in the FSC. Namely, FL is predominantly encountered between production and distribution, while FW in retail, food-service sector and at the consumer level (2).

According to FAO, on a global level one-third of the food produced for human consumption (3), relative to weight, is either lost or wasted, summing up to approx. 1.3 billion tons per year (4), thus leading to substantial economic, environmental and even social cost. The amount of food lost is specific to the different regions of the world and varies with the different track of the food value chain (FVC). However, it is noteworthy that food is lost and/or wasted from the commencing agricultural production to its end use – household consumption. Thus, it entails a "waste" of economic and natural resources and it brings along a social impact.

Agriculture is seen as the world's largest employer. Therefore, the high volume of wastage occurring in this sector have a major social impact in the developing countries. The effects are most significant on labour productivity and on wages, which consequently retards the expansion of the consumer market. This can be regarded as

a vicious cycle, difficult to exit, that reduces the resource availability at both ends – producers and consumers.

The economic cost of FLW was estimated in 2016 to mount up yearly to $940 billion on a global scale. A significant postharvest loss has been reported in the Sub-Saharan region of roughly $7.7 billion per year, equivalent to approx. 2.1% of the region's gross domestic product (GDP) (5). In addition to this economic cost, it has been highlighted that FLW often translates into higher demand and consequently to higher prices. Moreover, it has been observed that in non-competitive markets it is the consumer who ultimately pays for the inefficient production process of the food system. Figure 1-1 places vegetables at the top of the list of contributors to the economic cost of FLW with a staggering 23% out of the total cost, followed by meat with 21%, fruits (19%) and cereals (18%). Although meat only accounts for 4% out of the total FLW relative to weight, it covers 21% of the total economic cost of wastage due to its high production cost per kilogram. In contrast, cereals contribute to the total cost of wastage by a high volume of loss.

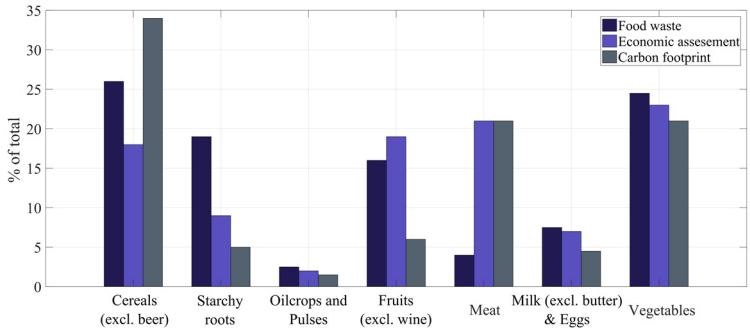

Figure 1-1 Contribution of commodities to food waste, to economic cost and corresponding carbon footprint. Adapted from (1).

In the developed countries food is lost at high volumes at the consumption level, wasted on the plate. Relevant examples are North America, industrialized China, and Europe, where out of the individual total of kcal lost and wasted, 61%, 46%, and 52%, respectively, is generated by the consumer, as depicted in Figure 1-2. The percentage is lower at the production stage, most likely due to more advanced technologies and qualified workers – below 25% for the aforementioned territories. On the other hand, in developing regions of the world, important quantities of food are wasted during the production-to-processing stages of the FVC, and less at the consumer level. This is mainly due to crops that go unused or unprocessed because of poor storage conditions or farmer's inability to get their goods to market. This is the case of Africa, West and Central Asia, Latin America, South, and Southeast Asia. FLW goes as low as 5% of total kcal lost at the consumer level in South Africa. However, a significant 39% is lost during production. A discrepancy is again obvious when the share of total

available food that is lost corresponding to each region is evaluated. Developed countries rank first, North America and Oceania leading with 42%, while developing countries keep the amount of wasted food at lower levels, with a miniumum of 15% lost by Latin America (6). Regardless of food loss origin and location, in a world where one in nine people is undernourished and one in three suffers from some form of malnutrition (7), the fact that 1.3 billion tons of food never gets to be consumed is outrageous. Moreover, this not only means missed opportunities for the economy and food security, but also a waste of all the natural resources used in the whole FVC.

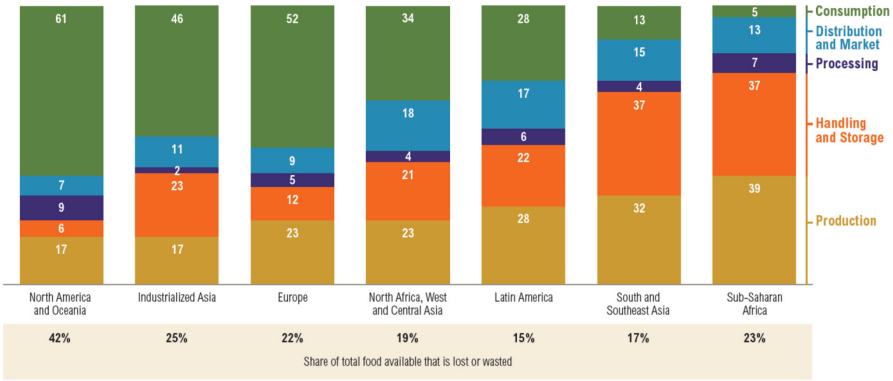

Figure 1-2 Percentage of food lost (kcal lost and wasted) per regions of the world relative to each stage of the food value chain. (6)

Throughout their extensive research, FAO has quantified the carbon footprint of food waste as the most notable impact on the environment. A product's carbon footprint is defined as the amount of greenhouse gases (GHG) emitted throughout its life cycle, expressed in kilograms of CO_2 equivalents (eq.). This includes the GHG emissions during the agricultural phase, on-farm energy use and non-energy-related emissions, such as livestock-generated methane (CH_4) and nitrous oxide (N_2O). If one were to consider FLW as a country, it would be the third-largest GHG emitter on the planet with approx. 4.4 GT CO_2 eq. in the year 2011, only surpassed by China and the United States, based on country data from 2012. To put into perspective, according to the United Nations Framework Convention on Climate Change (UNFCCC), the aforementioned amount of emissions sums up to more than twice the total GHG emissions of all USA road transportation in 2010 (1.5 GT CO_2 eq.) (1).

Returning to Figure 1-1, food wastage per commodity group, alongside its corresponding carbon footprint is emphasized. It is readily seen that the leading contributors to the carbon footprint are cereals, covering 34% of the total GHG emissions, followed by meat and vegetables, each with 21%. It is interesting to judge the impact of carbon footprint by normalizing the GHG emissions by the percentage of food waste. It becomes thus obvious that a low amount of waste does not necessarily translate into low GHG emissions, this being the case of the commodity

"meat" - although its contribution to food waste is relatively low the intensity of their carbon footprint, due to waste, is highest. Fruits and vegetables taken as a unity surpass cereals in terms of FLW and take the second place as the biggest GHG emitter. When field-grown, these commodities emit relatively low amounts of GHG, mostly originating from the use of diesel and nitrogen fertilizers throughout their agricultural phase. Commodities such as potatoes or starchy roots are efficiently cultivated, due to a high yield per unit area. So what causes such a high carbon footprint? The reason lies in the growth of fruits and vegetables in heated greenhouses, where heat production is the key parameter for such products' environmental impact.

Other important environmental factors to which FLW contributes are water usage/footprint, land usage, and closely connected to the latter, biodiversity decrease. These key quantifiable environmental factors are presented in a cross-analysis (1), categorized by commodity and world region pairs, together with the data on carbon footprint, detailed in the previous paragraphs. The cross-analysis is summarized in Table 1-1. This gives an overview on the impact of FLW on natural resources, and points out the different environmental regional hotspots. Noteworthy is cereal wastage in Asia, which cannot be overlooked, as it is a major environmental hotspot due to its impacts on natural resources (water and land) and carbon emissions. Similarly, vegetables emerge as a hotspot through the high GHG emissions in several regions - industrialized Asia, Europe, South and Southeast Asia, and moreover through the high FLW volume in industrialized Asia. As previously mentioned, the high carbon footprint is most likely caused by the growth in heated greenhouses all year around. Not lacking environmental importance are fruits, which distinguish themselves through both relatively high wastage volume and negative effect upon water resources.

All things considered, reducing food loss and waste can be an all-around win: it can help feed more people, it can financially aid farmers, companies, as well as households, and last but not least it can take off some of the pressure on climate and natural resources. This did not go unnoticed. In September 2015 world-wide awareness was raised towards the issue of FLW and it was ramped up on the global agenda at the United Nations General Assembly. The result was the adoption of 17 Sustainable Development Goals (SDGs) as part of the 2030 Agenda for Sustainable Development. These goals target to end poverty and hunger, protect the planet, and ensure welfare for all populations and generations to come (8). The goals came into effect on the 1st of January 2016. FLW is addressed by SDG 12, which aims at ensuring "*sustainable consumption and production patterns*". The third target of SDG 12 (SGD Target 12.3) seeks to *"halve per capita global food waste at the retail and consumer levels and reduce food losses along production and supply chains, including postharvest losses"* (8), by 2030.

Table 1-1 Cross-analysis of environmental factors grouped by "region - commodity" pairs. Percentage of total contribution. Rank noted in bold. Abbreviations to be found in the nomenclature. Adapted from (1).

Region * commodity	Volume		Carbon		Water		Arable land		Non-arable land	
Ind. Asia * Veg.	11.2%	**1**	10%	**3**						
Ind. Asia * Cereals	7.8%	**2**	14.4%	**1**	13.2%	**2**	5.4%	**5**		
S&SE Asia * Cereals	7.8%	**3**	11.1%	**2**	24.2%	**1**	9.3%	**2**		
SSA * SR	5.3%	**4**								
Ind. Asia * SR	4.5%	**5**								
Europe * SR	4%	**6**								
S&SE Asia * Veg.	3.9%	**7**	2.8%	**10**						
S&SE Asia * Fruits	3.6%	**8**			4.5%	**4**				
LA * Fruits	3.4%	**9**			3.3%	**6**				
Europe * Cereals	3.3%	**10**	3.3%	**9**						
Europe * Veg.	3.1%		4.2%	**8**						
NA, WA & CA * Veg.	2.7%				2.7%	**10**				
Ind. Asia * Fruits	2.7%				3.2%	**7**				
Europe * Fruits	2.6%				3%	**9**				
Europe * Meat & Milk	2.3%		5.2%	**5**			5.1%	**7**		
S&SE Asia * Meat & Milk	2.3%				3.4%	**5**	5.4%	**4**	16.7%	**2**
NA, WA & CA * Cereals	2%				7.8%	**3**	3.8%	**8**		
NA, Oce. * Meat & Milk	2%		5.2%	**6**			3.7%	**10**	8.4%	**5**
LA * Meat & Milk	1.5%		4.9%	**7**			6.9%	**3**		
Ind. Asia * Meat & Milk	1.5%		5.3%	**4**			11.5%	**1**	11.3%	**4**
S&SE Asia * Oilcrops & Pulses	1.3%				3.2%	**8**				
SSA * Cereals	1.3%						3.7%	**9**		
NA, WA & CA * Meat & Milk	0.9%								33.2%	**1**
SSA * Meat & Milk	0.5%						5.4%	**6**	13.1%	**3**
Total top 10	**55%**		**64%**		**68%**		**60%**		**83%**	

1.2. FRESH PRODUCE DEGRADATION

In the previous section, it was emphasized that one of the main contributors to global FLW is the spoilage of fruits and vegetables. Data gathered by FAO, presented in Figure 1-3, show that losses in the agricultural stage dominate the three industrialized regions, Europe, North America and Oceania, and industrialized Asia. Most likely, this is not due to inefficient agricultural processes (as is the case of the developing countries), but because the postharvest produce is not certified in terms of the high quality standards imposed by retailers. Once the retailers accept the fresh produce, losses still occur during postharvest processing and distribution, albeit their high quality. Looking at the FSC tracks between agriculture and consumption as one single key parameter, it becomes quite clear, that for all the regions considered in Figure 1-3, high volumes of fresh produce, from 8 to 20%, degrade before even reaching retail or the consumer. Moreover, waste at the end of the supply chain is also considerable in all three aforementioned regions, with 12-20% of purchased goods by mass being disposed of by the consumer.

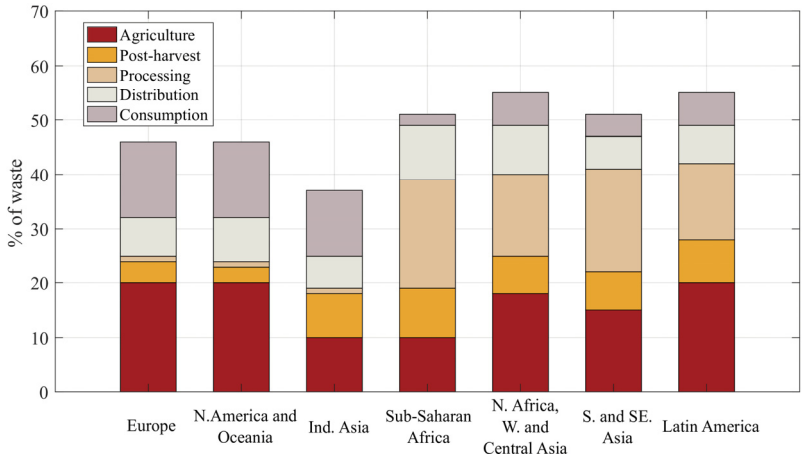

Figure 1-3 Percentage of food waste per region of the world corresponding to fresh produce.

From here on the term "postharvest" will be used when referring to the three following FSC tracks: postharvest, processing, distribution. The facts presented above underline the necessity of tackling food losses in the postharvest stage. To do so, the main drivers of postharvest losses (PHL) must be identified. The supply chain of fresh produce is complex and eminently dependent on environmental circumstances. In addition to this, the products are highly perishable and heterogeneous in nature. High volumes of PHL are a result of inadequate logistics and quality control mechanisms. The former include poor demand forecasting techniques, faulty inventory control systems (9), and lack of coordination along the FSC (3). Examples of inadequate quality control actions are lack of or insufficient atmospheric conditions control

(temperature, humidity, contaminants) (10), deficient packaging (3) and poor quality control (9).

Even after harvest, fruits and vegetables are alive, containing 65-95% water, continuing their physiological processes, such as respiration, transpiration and ethylene (C_2H_4) biosynthesis. Their postharvest life depends on the rate at which resources, in the form of stored food reserves and water, are used up. Once these are exhausted the produce dies and decays. Three major causes of enhanced degradation have been identified (11):

- Physiological deterioration – abnormal physiological degradation occurs when the produce undergoes high temperatures, low humidity levels or contamination.
- Mechanical damage – careless handling can lead to internal bruising, splitting and skin breaks, which in turn results in an increased water loss and enhanced physiological deterioration.
- Diseases and pests.

Taking part in physiological deterioration is the contamination with C_2H_4. But how can C_2H_4 be a contaminant, when the plants produce it naturally? This will be addressed in the following section.

1.2.1. ETHYLENE – ORIGIN AND IMPACT

Ethylene can originate from two different sources: natural (plants and plant products, such as fruits, vegetables, and flowers) and anthropogenic (air pollution, such as exhaust gases, cigarette smoke). C_2H_4 is regarded as a plant hormone and is produced by nearly all vascular plants at low concentrations, with enhanced production rate during ripening of fresh produce, aging in flowers and as a response to environmental stressors, such as bruising and cutting. It is being released at different rates depending on the produce and is responsible for the accelerated softening and ripening of fruits and senescence of flowers during transportation and storage, thus it is the main driver of postharvest life-shortening and accelerated deterioration. Considering this, unless intentionally added to the environment enclosing fresh produce, C_2H_4 is regarded as a contaminant/pollutant and exposure should be controlled and minimized.

The production rate of C_2H_4 of postharvest fresh produce highly depends on the commodity type and temperature, as does C_2H_4 sensitivity. In this sense, produce can be divided into two groups:

- “climacteric” – ripen after harvest. Go through two stages: preclimacteric and climacteric. During the first stage, the produce remains firm, C_2H_4 production is low and removal of C_2H_4 prolongs this stage. On the other hand, high C_2H_4 production and rapid ripening define the climacteric stage. An external source of C_2H_4 will initiate the autocatalytic C_2H_4 production, accelerating this phase. Examples: tomatoes, potatoes, avocados, apples, pears.

- "nonclimacteric" – ripening does not occur postharvest. Presence of C_2H_4 will shorten shelf life. Examples: leafy vegetables, strawberries, oranges, grapes.

As nonclimacteric fruits do not ripen postharvest, their C_2H_4 production rate is lower than 1 μL $kg^{-1}h^{-1}$ at 20ºC. In contrast, climacteric produce C_2H_4 at rates between 1-10 μL $kg^{-1}h^{-1}$ during their first postharvest stage, while the rate increases up to 10 times, when the produce ripens (12). Thus, the high production rate of climacteric produce can be problematic for sensitive commodities. Table 1-2 gives a few examples of C_2H_4 production rates, sensitivity levels and effects corresponding to common produce.

Table 1-2 C_2H_4 production rates, sensitivity and reaction to C_2H_4. Reproduced from (12).

Fresh produce	C_2H_4 production rate, μL $kg^{-1}h^{-1}$	C_2H_4 sensitivity level	Main response
Cherries	Very low < 0.01	L	Softening
Potato	Very low < 0.01	M	Sprouting
Cut flowers	Very low < 0.01	H	Sleepiness, leaf curl
Cucumber	Low 0.1 – 1	H	Yellowing
Banana	Moderate 1 – 10	H	Decay
Tomato	Moderate 1 – 10	H	Shrink, decay
Avocado	High 10 – 100	H	Decay
Apple	Very high > 100	H	Scald, lose crunch

Note: Sensitivity [ppm] – H = High (0.01 – 0.5), M = Moderate (0.5 – 3), L = Low (3 – 5)

As listed in Table 1-2, the range of C_2H_4 sensitivity is wide, from 0.01 to 5 ppm. This is particularly problematic as typical values for C_2H_4 concentrations in cold storage facilities can rise up to approx. 3.5 ppm, while in transportation trucks to approx. 2.5 ppm (12,13).

All things considered, it becomes quite clear that C_2H_4 is a real issue and contributor to global food waste. Its control and removal constitutes a pivotal parameter for the postharvest industry, particularly for transportation and storage stages of the cold chain, in terms of prolonged shelf life, quality and losses minimization.

1.2.2. ETHYLENE CONTROL

Control, removal, and inhibition of C_2H_4 in the fresh produce postharvest supply chain have received extensive attention throughout the past decades, resulting in widespread research and development of various techniques for C_2H_4 management. In this section, the C_2H_4 control strategies used in the present days are briefly presented.

For a better overview, the C_2H_4 control and removal are divided into two main categories: plant level action and environment level actions. The chart in Figure 1-4 gives a good overview on these techniques. As plant-level actions are out of the scope

of the present study, no further information will be given on these The interested reader is directed to (12).

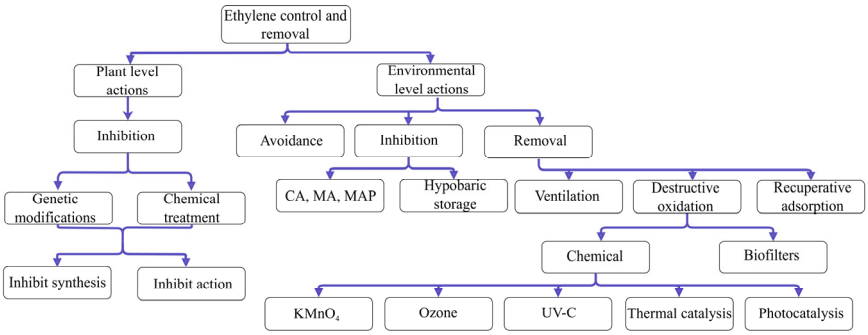

Figure 1-4 C_2H_4 management techniques. CA – Controlled atmosphere, MA – Modified atmosphere, MAP – Modified atmosphere packaging. Adapted from (12).

The most straightforward method of removal is ventilation. However, ventilation brings along extra energy consumption and cost, especially considering the cooling of the air and maintaining proper humidity levels. In addition, another major drawback is the fact that ambient air is contaminated with C_2H_4 from outside sources, such as pollution generated by exhaust gases of internal combustion engines. As a result, from a practical point of view ventilation is incompatible with controlled atmosphere (CA) and modified-atmosphere (MA) storage solutions.

CA storage involves altering the typical composition of the air surrounding the fresh produce by maintaining O_2 levels below 8% and CO_2 levels between 1-25%. These optimum levels slow the physiological processes of respiration and C_2H_4 production, reduce C_2H_4 action, retard degradation, and control insects, thus extending the postharvest life of the produce. MA is a type of CA, where postharvest products are stored in a favourable atmosphere other than air, by generally using the produce respiration and passive technologies. An example is the wrapping of boxes in polyethylene films, which act towards keeping the produced CO_2 inside, while hindering extra O_2 to enter. Both CA and MA have proven themselves to be efficient methods of controlling C_2H_4, but their commercial application has been troublesome due to the relatively high cost. More on CA storage can be found in (14). Another particular type of CA is the modified atmosphere packaging (MAP) technique. MAP involves sealing actively respiring fresh produce in polymer film packaging to modify levels of both O_2 and CO_2 within the package enclosure.

Hypobaric storage relies on Dalton's Law, according to which a reduction in pressure would consequently cause a reduction in O_2 partial pressure and thus in its availability to the flowers, fruits or vegetables in that storage. Lowered pressure removes C_2H_4 and other volatile organic compounds (VOCs), while low levels of O_2 decreases respiration and C_2H_4 production. Ventilating air at pressure below 50 kPa and high

humidity levels comes at high costs and restrictive safety considerations. A historic and technological detailed overview is given in (15).

One of the easiest methods to eliminate C_2H_4 and prevent its impact on perishable produce is to scrub it from storage facilities and transportation environments, either by destructive or recuperative methods. Destructive methods offer the possibility of continuously and irreversibly removing C_2H_4, as it is the case of oxidation. When O_2 is the oxidizing agent, C_2H_4 is degraded according to reaction (1.1).

$$C_2H_4 + O_2 \rightarrow CO_2 + H_2O \qquad (1.1)$$

This reaction is thermodynamically favored, with a Gibbs free energy of -1331 kJ/mol and has to be initiated thermally (> 800ºC), catalytically (100-800ºC), photochemically by UV light, or photocatalytically by UV light on a semiconductor material. Both photo-activated reactions can operate at ambient or sub-ambient temperatures. Regardless of the activation method, the contaminated air needs to be circulated through the scrubber for effective degradation. Some of the popular oxidation technologies are:

- $KMnO_4$-based scrubbers;
- Biofilters;
- Ozone degradation;
- Photochemistry under UV-C light;
- Vacuum UV (VUV) photolysis;
- Catalytic degradation;
- Photocatalysis under UV-A light.

The C_2H_4-scavenger, $KMnO_4$, cannot be used in contact with food, due to its high toxicity. Ozone (O_3) is a powerful oxidant, but highly unstable and decomposes to O_2 rapidly, while at the same time being a hazard as it causes serious and irreversible damage to both human and plant tissue.

Non-destructive techniques of C_2H_4 removal are the recuperative methods, operating on the principle of adsorption. Adsorption mechanisms can be employed to achieve a selective separation process for removing small quantities of an adsorbate from a fluid stream. The most commonly used C_2H_4 adsorbents are zeolites (aluminosilicate minerals characterized by a 3D framework structure with interconnected cages and channels) and carbon-based materials (activated carbon, charcoal, carbon spheres). Compared to oxidative methods, recuperative methods exhibit a low removal capacity. Moreover, adsorbers transfer C_2H_4 to another phase rather than degrading it, thus additional disposal or handling is necessary.

Photocataytic degradation of VOCs has been established as one of the most desirable, yet challenging goals in the research and development of environmentally friendly and cost effective catalysts.

1.3. PROJECT OBJECTIVES

It has been emphasized that food waste is a critical issue for both the economy and the environment, with fresh produce being one of the main contributors and C_2H_4 one of the main drivers. Researching has led to the development of several methods for C_2H_4 control and removal, at either plant or environmental level.

This project aims at employing the process of photocatalytic oxidation over titanium dioxide (TiO_2) thin films for the degradation of C_2H_4. One of the main objectives was the derivation of a kinetic rate law describing the degradation under varying C_2H_4 concentration conditions of interest and irradiation levels. Derived mathematical models aided the simulation of a continuous flow reactor, enabling the identification of enhancing and retarding process conditions for C_2H_4 conversion.

1.3.1. THE FRESH PROJECT

This PhD dissertation is part of the *"Fresh produce through Reduction of Ethylene during Storage and Handling"* (FRESH) project. The FRESH project is a larger Danish research project with the vision to minimise food waste by enabling efficient monitoring and control of C_2H_4 levels, thereby avoiding premature ripening and spoilage, and thus, prolonging the in-store shelf life and quality of produced goods.

The overall research and innovation goals for this project were:

- Development of tailored and scalable photocatalytically active surfaces for degradation of C_2H_4
- Designing air-cleaning solutions relying on CFD models implementing photocatalytic surface reactions and UV irradiation in advanced flow models.
- Integration of state-of-the-art sensors in a wireless network solution.
- Scaling and integration of the design, surfaces and sensors to achieve a full-size air cleaning and monitoring solution.
- Test and evaluation of elements and prototype units at end-users.

The principal activities of the FRESH project, corresponding to the aforementioned objectives, were divided into 6 interconnected work packages (WP), as displayed in Figure 1-5.

The FRESH project brought several partners from the industry together, in addition to Aalborg University and the Danish Technological Institute (DTI). The latter contributed with knowledge in the field of nanotechnology, with focus on coating technologies. The industry partners offered data on the average produce losses registered, in terms of commodity type and average amount. Moreover, the partners involved in the postharvest industry gave significant insight into their expectations and needs in terms of an air-cleaning device. These partners were:

- Salling Group A/S (Dansk Supermarked Group at the start of the project): Large logistics chain.
- Aarstiderne A/S: Meal box preparation and delivery.
- PKM A/S: Plant production and temporary storage.
- Alex Andersen A/S: Fresh produce transportation.
- Develco Products A/S: Customized wireless products, IoT solutions.

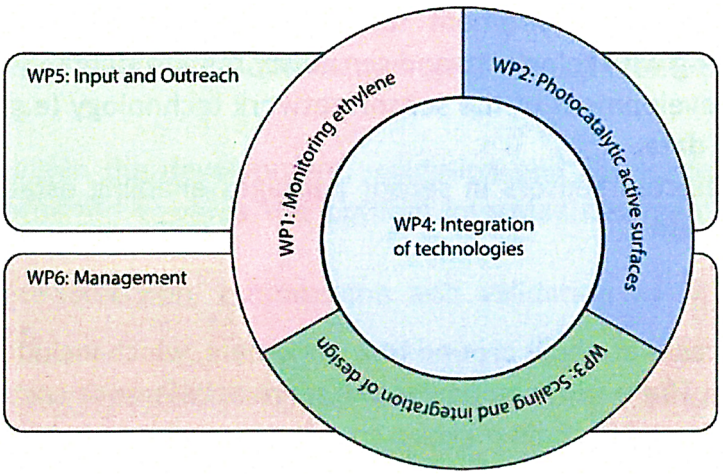

Figure 1-5 FRESH work packages.

The work conducted for this PhD thesis is an integrating part of the FRESH project's main goals, with activities in WP3. The studies presented in this thesis contributed to the design of an air-cleaning solution by deriving a kinetic model for the photocatalytic reaction and integrating it into flow models, allowing the investigation of the influence of process parameters on the degradation of pollutant.

The project goals are elaborated with the following objectives:

1. Study on postharvest fresh produce
   a. Collect data on fresh produce spoilage
   b. Analysis of typical storage and transportation conditions

2. Choice of catalyst coating
   a. Identify substrate material candidates
   b. Coat substrate materials with TiO_2
   c. Determine properties of resulted catalysts
3. Kinetic modelling of photocatalytic reaction
   a. Experimentally monitor photocatalytic reaction
   b. Derive kinetic parameters

4. Photocatalytic reactor design
    a. Establish design criteria
    b. Prototype manufacturing and operation
    c. Parametric study by CFD

Hence, this is a multidisciplinary project, in which multiple partners both from the academic and the industrial sectors were involved. Despite the broad goals of the project, the main focus of this work has been to investigate, design and optimise an air-cleaning solution for the post-harvest industry through CFD simulations.

1.4. METHODOLOGY

The methods used to reach the four main objectives are described in the following.

Study on postharvest fresh produce

The initial focus is on establishing the spoilage hotspots the Danish postharvest industry has to deal with. Data on type and amount of fresh produce waste is gathered from the project partners. Study cases and measurements campaigns are established at a storage facility and in a transportation truck to monitor typical values of relative humidity, temperature, concentrations of CO_2 and C_2H_4.

Choice of catalyst coating

Titanium dioxide, from clusters to colloids to powders and large single crystals, is defined as being an ideal photocatalyst (16), thus it is being used as a semiconductor for this application. As it can come in many forms (anatase, rutile, brookite etc.) and can be coated on a multitude of substrate materials, several TiO_2 coatings differentiating themselves by substrate material are examined, to select the appropriate catalyst. Analytical techniques are employed to characterise the coated substrates in terms of TiO_2 form, thickness, and photocatalytic activity.

Kinetic modelling of photocatalytic reaction

The TiO_2 mediated photocatalytic oxidation of C_2H_4 is kinetically described to derive dependencies on pollutant concentration and available radiation intensity.
An experimental batch reactor is employed to monitor the degradation of C_2H_4 in time, while key parameters such as incident surface radiation and initial C_2H_4 concentration are varied. Data previously gathered during the measurement campaign helped in the design of the experiments, by providing relevant concentration levels, relative humidity and temperature values under which the reaction has to be performed. Experimental concentration data are analysed and the reaction laws most commonly

used to describe photocatalytic processes are evaluated in terms of goodness of fit to the experimental degradation. These are the popular Langmuir-Hinshelwood kinetics and the fundamental zero and first-order reaction laws.

Photocatalytic reactor design

A photocatalytic reactor is designed with application in the postharvest industry, to be installed in storage facilities, transportation trucks, and even retail stores. Design criteria are established to maximise the contact between pollutant species and active surface as well as the radiation distribution. The reactor geometry is 3D modelled in Autodesk Inventor and subsequently used for manufacturing and flow simulations coupled with species and radiation transport, using ANSYS Fluent.
A parametric study is carried out, observing the reactor's behaviour under different flow conditions and geometry alterations, to establish an optimal design and enhanced conversion. Again, thanks to the storage campaigns carried out, the simulation cases can be defined realistically.

1.5. OUTLINE OF SUMMARY REPORT

The dissertation consists of summary report and Papers A and Paper B, which describe some topics in more detail, while some research activity conducted in relation to the dissertation is only described in the summary report. This section gives the reader an overview of the structure of this dissertation. The chapters are briefly summarised in the following.

Chapter 2 gives an introduction to the process of photocatalysis, from fundamentals to reaction kinetics, and presents the current state of the art of environmental air remediation through UV-mediated catalysis.

Chapter 3 presents the case studies conducted at a Danish storage facility and a transportation truck, with emphasis on the measured levels of C_2H_4, temperature and relative humidity. The chapter includes results described in Paper B.

Chapter 4 focuses on the photocatalytic reaction – choice of catalyst, kinetic modelling via experimental reaction monitoring and dependence to species concentration and surface incident radiation. The chapter includes results published in Paper A and B.

Chapter 5 presents the photoreactor designed for postharvest application as well as the parametric study conducted through CFD.

Chapter 6 contains a discussion, concluding remarks and future work perspectives.

CHAPTER 2. TITANIUM DIOXIDE PHOTOCATALYSIS

2.1. TITANIUM DIOXIDE

Titanium dioxide (TiO_2) belongs to the family of transition metal oxides. Mineral sources are rutile, ilmenite, anatase, and brookite, with rutile being the most stable TiO_2 form, but anatase the most active. It has been industrialized at the beginning of the 20^{th} century, when toxic lead oxides started being replaced with TiO_2 as pigment in white paint, plastics, and paper. Younger applications are present in sectors such as textiles, food (as colouring), leather, pharmaceuticals (tablet coating, toothpaste, sunscreen, cosmetics), and different titanate pigments. (16)

TiO_2 quickly became a popular material due to its non-toxicity, low cost, chemical stability, and other beneficial properties. More recently, TiO_2 application has been extended to state-of-the-art technologies. Due to its high refractive index, it is a good candidate for anti-reflection coatings in silicon solar cells and thin-film optical devices. Its conductivity dependence on gas compositions is an excellent property for use in gas sensors and detection of O_2 and CO at high temperatures, > 600ºC (17,18). Thanks to its homeocompatibility with the human body, TiO_2 is used as a biomaterial, as bone substituent and reinforcing mechanical supports (19,20).

TiO_2 is also used in catalytic reactions, having the ability to hold a multitude of roles – promoter, semiconductor, carrier for metals and metal oxides, additive and catalyst (21). Reactions using TiO_2 as a catalyst are (16):

- Selective reduction of NO_x to N_2;
- Effective decomposition of VOCs;
- Hydrogen production by gas shift production;
- Fischer-Tropsch synthesis;
- CO oxidation by O_2;
- H_2S oxidation to S;
- Reduction of SO_2 to S by CO
- Photocatalytic reactions.

Photocatalytic reactions will be detailed in the following section.

2.2. FUNDAMENTALS OF PHOTOCATALYSIS

The basic principle that photocatalysis relies on is the formation of an electron-hole (e^- – h^+) pair, as a result of the absorption of a photon with an energy ($h\nu$) equal or greater than the semiconductor's band gap. The principle is graphically summarised by Figure 2-1. The photogeneration of an e^- – h^+ pair (a) is a well-known process in both direct and indirect semiconductors (22). As the photon is absorbed, a photogenerated hole is created in the valence band, h^+_{VB}, and a photogenerated electron is formed in the conduction band, e^-_{CB}:

$$Photocatalyst \xrightarrow{h\nu} e^-_{CB} + h^+_{VB} \qquad (2.1)$$

where h – Planck constant, h = 6.626e-34 J·s
ν – photon frequency, Hz

In Eq. (2.1) the product $h\nu$ represents the photon energy and it is referred to as the Einstein-Planck relation, $E=h\cdot\nu$, [eV]. The formed entities are highly reactive, thus being involved in all subsequent chemical processes simultaneously oxidizing and reducing the corresponding species present in the system.

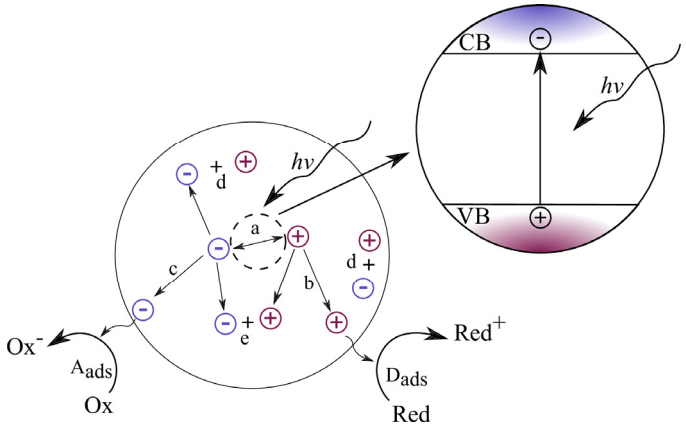

Figure 2-1 Central photon-mediated processes on semiconductor particle. (a) e^--h^+ generation; (b) oxidation of donor; (c) reduction of acceptor; (d) and (e) recombination at surface and in bulk, respectively. Re and Ox – oxidative and reductive species. Reproduced from (16).

Photogenerated e^- react with the corresponding species, (c), an acceptor, which typically is O_2 in environmental photocatalysis, forming a powerful superoxide and finally being transformed into H_2O. Their counterparts, the photogenerated h^+, depending on their oxidizing potential oxidise the targeted molecules (also named donors), usually an organic compound acting as a pollutant (b). If the oxidation

proceeds to complete degradation, with CO_2 and H_2O as final products, the compound is said to have been mineralised.
The h^+ species are delocalized and free to move in the crystal structure of the semiconductor (23), thus these move towards the surface of the catalyst, being transferred to the corresponding chemical species for oxidation. Unfortunately, details on how the h^+ entities diffuse to the surface, the speed at which they travel through the lattice, or which crystallographic direction is favourable are research topics still actively debated (23). Regardless of the pathway, two mechanisms can take place: (1) entities are transferred to adsorbed species, oxidising it immediately (direct photocatalysis, Eq. (2.2)), or (2) entities react with adsorbed H_2O molecules, producing hydroxyl radicals ($OH^{\cdot}$) , which subsequently react with the adsorbed pollutant resulting in oxidation (indirect photocatalysis, Eq. (2.3)):

$$h_{VB}^{+} + Pollutant \rightarrow Pollutant_s^{\cdot +} \quad (2.2)$$

$$h_{VB}^{+} + OH^{\cdot} \rightarrow OH_s^{\cdot} \quad (2.3)$$

In both equations the subscript "s" denotes the creation of surface groups, hence these can be considered to be surface trapped species.
Mechanism 2 is the typical pathway followed by the photodegradation of C_2H_4 over TiO_2 (24–26). The photo-oxidation of C_2H_4 is thus mediated by the action of $OH^{\cdot}{}_s$ and its rate will inevitably depend on the rate at which the radicals migrate to meet the pollutant or how fast the latter can diffuse to the surface trapped radicals (23). The photogenerated $OH^{\cdot}$ radicals are able to react with the pollutant in two different regimes: as adsorbed species on the catalyst surface, or as free radicals in the bulk solution.

2.3. REACTION MECHANISM

Regardless of the mechanism regime followed, the photocatalytic process leads to complex subsequent reactions. Whether oxidation takes place directly or indirectly manner is still an open question for many systems. Moreover, a definite approach considering initial e^- - h^+ transfer steps is still lacking. (23)

Regarding the UV-activated photocatalytic oxidation of C_2H_4 over TiO_2, no consensus has been reached in terms of a general valid mechanism, to the author's knowledge. However, several studies (24–31) have been carried out to establish a reaction pathway. According to the findings reported by Park et. al (29) C_2H_4 is first oxidised to CO, by the formation of ethylene oxide (C_2H_4O) radicals, which are subsequently oxidised to CO_2. Under conditions of excess O_2, C_2H_4 will be completely oxidised into CO_2. A slightly different pathway was proposed by Yamazaki et. al (27) according to which the absorbed species C_2H_4 and OH react to produce C_2H_4OH radicals, that further react with adsorbed O_2 reaching the mineralisation stage to CO_2. Moreover, it was concluded in this study that the rate-determining step is the reaction

between the C_2H_4OH radical and adsorbed O_2. In the following, one of the recently proposed mechanism by will be presented, resulted from the experimental study of Hauchecorne et. al (26). The authors have derived a reaction pathway starting from the assumption that mainly OH·s perform the oxidation. Their experimental setup consisted of an FTIR (Fourier-transform infrared spectroscopy) in situ reactor, which offered the possibility of observing the reactions occurring at the catalytic surface in real-time. The catalyst in the form of grinded TiO_2 pressed on a 13 mm disk, irradiated by UV-A light, was employed to oxidise a gaseous solution with concentrations of C_2H_4 ranging from 5000 to 10000 ppm. Interestingly it was concluded that the reaction pathway includes the formation of intermediate formic acid and formaldehyde. The latter was bound in two different forms – coordinatively and as bidentate. The oxidizing agent was established to be multiple OH· radicals, but the authors consider that in this sense more research is needed. The proposed reaction mechanism is summarised in Eqs. (2.4) – (2.12).

$$TiO_2 + h\nu \rightarrow e^- + h^+ \quad (2.4)$$

$$H_2O + h^+ \rightarrow OH^{\cdot} + H^+ \quad (2.5)$$

$$C_2H_4 + Ti_5O_4H_4 + 2OH^{\cdot} \rightarrow 2CH_2 + Ti_5O_4H_2 + H_2O \quad (2.6)$$

$$2CH_2 + Ti_5O_4H_2 + 2OH^{\cdot} \rightarrow 2CH_2 + Ti_5O_4 + 2H_2O \quad (2.7)$$

$$2CH_2 + Ti_5O_4 + 2OH^{\cdot} \rightarrow 2CH_2O + Ti_5O_4H_2 \quad (2.8)$$

$$2CH_2O + Ti_5O_4H_2 + 2OH^{\cdot} \rightarrow 2HCO + Ti_5O_4H_2 + 2H_2O \quad (2.9)$$

$$2HCO + Ti_5O_4H_2 + 4OH^{\cdot} \rightarrow 2HCO_2 + Ti_5O_4H_2 + 2H_2O \quad (2.10)$$

$$2HCO_2 + Ti_5O_4H_2 \rightarrow 2CO_2 + Ti_5O_4H_4 \quad (2.11)$$

$$C_2H_4 + 12OH^{\cdot} \rightarrow 2CO_2 + 8H_2O \quad (2.12)$$

As aforementioned, a consensus has not been yet reached in terms of the pathway followed by the photoreaction degrading C_2H_4 over TiO_2, mediated by UV-A light. On the other hand, when discussing the rate laws that can be successfully used to characterise and estimate the photodegradation of C_2H_4 over TiO_2 the science community seems to agree and often draws to the same conclusions. This will be discussed in the following.

2.4. REACTION KINETICS

Langmuir-Hinshelwood (LH) kinetics is the most commonly applied reaction law to express the kinetics of the heterogeneous catalytic process. This approach describes the catalyst surface as an array of equivalent sites, which do not interact either before or after chemisorption (32) and accounts for the affinity of the species to the catalyst coating, through the Langmuir adsorption equilibrium constant. Equation (2.13) describes the usual kinetic expression of the LH model.

$$r = \frac{dC}{dt} = \frac{k_r K_{abs} C}{1 + K_{abs} C} \quad (2.13)$$

where r – reaction rate
C – concentration of species
t – reaction time
k_r – reaction rate constant
K_{abs} – adsorption equilibrium constant

The LH rate law can take multiple forms, depending on the complexity of the kinetics that one desires to achieve, that is single-site or multiple-site adsorption and monomolecular or multi-molecular adsorption. Due to this, parameters of (2.13) have not been defined in terms of units.

Sirisuk et al. (31) have studied the photocatalytic degradation of C_2H_4 over TiO_2 thin films supported on glass rings, to conduct kinetic studies. They have employed a tubular photoreactor to monitor the conversion of C_2H_4 under different catalyst thicknesses and catalyst weight to flow rate ratios, with and without thermal management. Both the increase in catalyst thickness and the increase in temperature enhanced the reaction rate. For deriving kinetic parameters, the researchers have employed a simple single-site monomolecular LH rate model, as given in (2.13), integrating it into the design equation of an ideal plug flow reactor. A similar approach was adopted by Vincent et al. (33). After linearization, the rate law resulted in:

$$\frac{W}{F} = \frac{1}{k_r K_{abs} C} ln\left(\frac{C_0}{C}\right) + \frac{1}{k_r}\left(\frac{C_0 - C}{C_0}\right) \qquad (2.14)$$

where W – catalyst weight, g
F – molar flow rate, mol/s
k_r – reaction rate constant, mol/g s
K_{abs} – adsorption equilibrium constant, L/mol
C – concentration of species, mol/L

Obee and Hay (34) used the single-site bimolecular LH rate expression, given in (2.15), to model the photocatalytic oxidation of C_2H_4 over TiO_2-coated glass plates, while at the same time investigating the effect of relative humidity and temperature on the derived kinetics. The kinetics in this study account for the competition on vacant active sites between H_2O and C_2H_4.

$$r = k_0 \frac{K_E X_E}{(1 + K_E X_E + K_W X_w)} \qquad (2.15)$$

The variables in (2.15) are equivalent to those previously defined, where “E” and “W” stand for C_2H_4 and H_2O, respectively.
A slightly different kinetic approach has been applied in (35) and (36), where the

photocatalytic oxidation of toluene and formaldehyde has been modelled by means of LH kinetics in the form of dual-site bimolecular adsorption:

$$r = k_0 \frac{K_1 X_C}{(1 + K_1 X_C + K_2 X_w)} \frac{K_4 X_W}{(1 + K_3 X_C + K_4 X_w)} \quad (2.16)$$

Cao et al. (37) concluded that the oxidation data corresponding to the photodegradation of 1-butene over stannic oxide (SnO_2) and TiO_2 is best represented by a single-site bimolecular LH mechanism.
The kinetic study conducted by Zhang and Liu (38) revealed, based on a comparison of three different LH kinetics types, that the bimolecular competitive adsorption LH mechanism can successfully estimate the photo-oxidation of hexane over TiO_2.
A complex kinetic modelling was achieved by Puma et al. (39), using the well-researched photocatalytic oxidation of trichloroethylene (TCE) in air over TiO_2 by deriving a model based on chlorine atom attack of the TCE molecule and 17-equation reaction mechanism. The rate law obtained has the form of LH kinetics that takes into account the affinity of H_2O for the active sites, and is applicable to different reactor geometries working with the same TiO_2 coating and under same operating conditions.

The LH expression given in (2.13) can be evaluated in terms of concentration and be simplified accordingly.
Firstly, let us assume a high molar concentration of the model compound. In the context of air contamination, this is regarded as a high concentration as 1 kmol/m^{3}s equals to 10^6 ppm. Thus, it can be stated that $K_{abs}C \gg 1$ and (2.13) becomes a fundamental zero-order reaction rate, (2.17), according to which the kinetics are independent of the concentration of species. This may rise due to catalyst saturation or due to limitations in radiation supply or mass transfer.

$$r = \frac{dC}{dt} = k_r \quad (2.17)$$

Secondly, let us assume a very low concentration of the pollutant, as it is in the case of C_2H_4 levels in storage facilities of approx. 3 ppm, corresponding to a molar concentration of 3e-06 kmol/m^{3}s. Under this condition, the denominator in (2.13) is negligible and the LH rate law can be reduced to a pseudo-first-order rate law. The product $k_r K_{abs}$ is being treated in (2.18) as a single term, k_{app}, called apparent first-order rate constant.

$$r = \frac{dC}{dt} = k_{app} C \quad (2.18)$$

Ching et al. and Shiraishi et al. (40, 41) have successfully applied a pseudo-first order rate law to model the photocatalytic degradation of low levels of formaldehyde over TiO_2 powder. The same reduction to a first-order rate was adopted by Pathak et al. (42) to evaluate the degradation of C_2H_4 by VUV radiation for fresh produce storage

applications. Van Walsem et al. (43) have investigated a novel multitube photoreactor through CFD simulations and FTIR experimental monitoring, to be used for the degradation of acetaldehyde in air under UV irradiation. An investigation of the photocatalytic degradation of indoor air pollutants was carried out by Héquet et al. (44). The model VOCs were toluene, *n*-decane, and TCE. Their degradation was studied both as individual contaminants and in mixture and was compared quantitatively by employing a first-order reaction rate, as it was observed that the conversion of toluene and *n*-decane follows a mono-exponential decay path.

The applicability of the LH model, as well as its reducing to a pseudo-first-order reaction rate, to the photocatalytic degradation of C_2H_4 over TiO_2 thin films, will be addressed in Chapter 4.

CHAPTER 3. POSTHARVEST STUDIES

3.1. LOSSES EVALUATION

The present subchapter will address the fresh produce losses that four of the industrial FRESH partners need to deal with during storage and transportation. Each partner offers a different perspective on losses, as these are involved in different areas of the postharvest industry of fresh produce:

- Salling Group A/S (Dansk Supermarked Group at the start of the project): Large logistics chain. Losses at local storage and in-transport of fresh produce.
- Aarstiderne A/S: Meal box preparation and delivery. Storage losses.
- PKM A/S: Plant production and temporary storage. Losses in greenhouses.
- Alex Andersen A/S: Fresh produce transportation. In-transport losses of plants/flowers.

The data presented are a result of the economic feasibility study conducted to evaluate the viability of the solutions developed through the FRESH project. The knowledge gathered through these studies brings value to the subsequent design process. A succinct report will be given in the following.

Salling Group A/S

Interviews and measurement campaigns at Salling Group A/S have identified the critical stages in the logistic chain to be:

- In-store local storages, where small units store a mixture of fresh produce
- Long in-transport from Southern Europe (3 – 6 days of transport)

Table 3-1 Commodities handled at Dansk Supermarked with corresponding waste percentage and C_2H_4 sensitivity. "-" – low, "+" – high, "++" – very high.

Commodity	Average waste, %	C_2H_4 sensitivity
Pear	36	+
Basil	19	-
Potato	18	-
Bell pepper	18	-
Avocado	28	+
Mushroom	25	-
Cucumber	22	++
Broccoli	22	++
Asparagus	18	-
Lettuce	15	++
Tomato	14	+

The annual value of waste of C_2H_4-sensitive commodities, listed in Table 3-1, in Salling Group A/S stores sums up to 60 million Danish Crowns (DKK), distributed to over 600 stores. Unfortunately, it was difficult to assess what fraction of this loss can be attributed to C_2H_4.

As the option of air-exchange is limited in many stores, a combination of C_2H_4-warning systems combined with an air-cleaning unit to keep levels of C_2H_4 sufficiently low can be an option for Salling Group A/S.

Aarstiderne A/S

At Aarstiderne, the goods are also managed in two different storage sections. The so-called "private" sector is dedicated to goods to be delivered to private costumers. Here the storage period is short as goods are quickly packed for delivery, thus no concerning levels of C_2H_4 have been registered. In the "wholesale" section, measuring campaigns (detailed in section 3.2) have revealed relatively high levels of C_2H_4 (0.5-1.5 ppm).

The value of the goods stored in the engross area sums up to 35 million/year of which approx. 5-10% was lost, translating into 1.74 – 3.5 million/year. As previously assumed, if 10% of the loss is related to C_2H_4 exposure, the yearly losses would mount up to 175,000 – 350,000 DKK. Table 3-2 presents the commodities commonly handled at Aarstiderne, giving the frequency at which these are present in the storage units and their sensitivity to C_2H_4. The produce generating the most C_2H_4, apples and pears, are stored separately, as to protect the rest of commodities.

Table 3-2 Commodities handled at Aarstiderne, with corresponding presence frequency and C_2H_4 sensitivity. "-" – low, "+" – high, "++" – very high.

Commodity	Average relative frequency, %	C_2H_4 sensitivity
Bananas	100	+
Grapes	25.35	-
Lettuce	13.04	++
Mango	15.39	++
Pineapple	15.02	-
Tomatoes	11.84	+
Broccoli	9.22	++
Watermelon	10.18	+
Peach	6.93	+
Cucumber	5.70	++
Mushroom	5.83	-
Clementine	4.83	+

Aarstiderne A/S showed interest in benefiting from both an air-cleaning unit and a warning system, based on C_2H_4 sensors.

PKM A/S

At PKM A/S, the plants are packed and loaded on transportation racks, which are kept in a cooled local storage. However, due to logistics reasons, oftentimes the goods are temporarily stored in the packaging area for 6-12 hours. C_2H_4 measurements have shown very little to no C_2H_4 in the cold storage, but higher levels in the packaging area, which can lead to significant deterioration of the product quality.

The waste occurs at both production and storage stages of the chain, with a loss corresponding to 5-7% and 10-12%, respectively, out of the total produced goods – 20 million plant pots per year. The waste during production is not C_2H_4-related, due to non-sensitivity in the young stage. Therefore, only the storage phase was of interest, due to the development of C_2H_4 sensitivity in mature plants. A waste fraction of 10-12% of 20 million plants with a production cost of 5.50 DKK represents a cost corresponding to 11-13 million DKK yearly, which translates to a loss in profit of 4 – 4.8 million DKK. A very conservative estimate of the influence of C_2H_4 exposure is that 10% of the loss derive from this exposure. Hence, the value of products lost due to exposure amounts to 1.1 – 1.3 million DKK per year with a profit loss of 400,000 – 480,000 DKK/year.

Thus, due to the high sensitivity of plants to C_2H_4, PKM A/S could benefit from using an air-cleaning unit in their packaging area.

Alex Andersen A/S

At Alex Andersen, several measurement campaigns, detailed in section 3.2, have revealed a good C_2H_4 control with low levels of C_2H_4. The exception is transportation trucks on board of ferries, where highly exhaust-gas-contaminated environmental air pollutes the internal air. Hence, the project partner would benefit only from a monitoring system, which would help in documenting the low C_2H_4-levels.

Although, Alex Andersen has shown good C_2H_4 control, this is not necessarily the case for other carriers not specialised in flower transport. Losses arising from C_2H_4 exposure can be relevant when transporting mixed goods or during long-haul transport. Thus, air-cleaning devices implemented in transportation trucks are still a viable solution with potential.

3.2. STORAGE AND TRANSPORTATION

Investigations, hereafter called campaigns, were conducted on a transportation truck from Alex Andersen A/S and in a typical storage facility at Aarstiderne A/S. The campaigns had as main objective to measure average C_2H_4 concentrations generated by fruits and vegetables during a timeframe of several days. The secondary objectives were to determine average temperature and relative humidity (RH) values. The necessity of having this data is twofold: first, for design purposes and secondly, for kinetic modelling. These two steps are interconnected as the prototype is dimensioned and designed according to the operating conditions, and at the same time, its optimisation depends on the kinetics of the photocatalytic reaction, which are implemented after an experimental kinetic study has been conducted. The kinetic study will be based on the values determined on field, in order to emulate real conditions at the highest possible extent.

3.2.1. TRANSPORTATION CAMPAIGN

This measurement campaign aimed to record the C_2H_4 concentration during short term transports of fruits and vegetables in truck trailers used by Alex Andersen A/S. Figure 3-1 and Figure 3-2 show the layout of the truck and the enclosure with stacked flower cases, during one of the typical flower transportations, respectively. The trailer dimensions are 13.95 x 2.55 x 2.75 m, resulting in a volume of approx. 100 m^3.

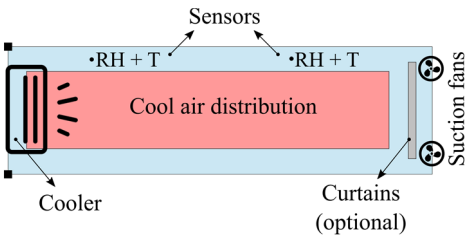

Figure 3-1 Transportation truck layout.

Figure 3-2 Typical flower cargo.

A battery-driven C_2H_4 sensor prototype, developed by Develco Products especially for the project, was installed in a case, together with an environmental sensor, recoding temperature and RH. The data was logged on an SD-card every 15 seconds. During flower transport the temperature was kept at approx. 14ºC and RH at 90%,

while the measured C_2H_4 concentration was low, as previously mentioned – approx. 0.01 – 0.025 ppm. As these levels were considered too low, compared to reported levels in storage facilities, further focus was not placed on flower transport, but mainly on fruits and vegetables. During fresh produce transportation the temperature was 5ºC and RH 80%.

Therefore, the campaign was carried out in trailers of various fruits and vegetables from the end of August to end of September 2018. The trucks drove up to 24 hours/day in Denmark, time in which several transports took place and during which the sensor was not shut off. The individual transport was reported to last between 6-8 hours. The typical process of a transport haul is as follows: loading, transport, partial unloading followed by several stops with unloading until the trailer is empty. Unfortunately, the different stages were not tracked and there was no data provided on location, type of produce transported and at which capacity, thus it was not possible to correlate these to the data recorded.

Two continuous intervals of 48 and 132 hours were successfully recorded, hence a total of 180 hours of logged data were acquired, with 105 were registered to be at low temperature, meaning that the sensors were in a cooled environment or inside the trailer. Figure 3-3 and Figure 3-4 display the measured C_2H_4 concentration, RH, temperature, and pressure for the 48 and the 132 hours sessions recorded, respectively. It was easy to pinpoint when the sensor was not placed among produce, as the pressure did not fluctuate, RH decreased and the temperature rose above 18ºC, these values being a good sign of the sensors being in an indoor environment, such as an office. To indicate the period under which the sensor was not together with the produce the data corresponding to this was plotted with grey color. During the measurement campaign, the C_2H_4 was predominantly below 0.1 ppm, thus the levels are not high enough to present a concern in most of the transport. However, in the short dataset (Figure 3-3a) there are two periods where C_2H_4 levels exceed 0.3 ppm – over 3 hours, starting at timestamp 29 hours, and over 1 hour, starting at timestamp 45 hours. Similarly, the long dataset (Figure 3-4a) presents three instances where C_2H_4 concentration exceeds 0.3 ppm.

It must be noted that the sensor used to record the C_2H_4 concentration is cross-sensitive to other VOCs that are likely to be present, released by the produce or from diesel exhaust. Consequently, the actual concentration might be lower. However, it can be stated that the presented data introduce a worst-case scenario for the transportation of fresh produce.

To conclude, the measured C_2H_4 levels are low throughout most of the transport period, regardless of short-term or long-term transports, as shown by the two measuring sessions conducted. During the 105 hours in which the produce were under transportation, the concentration is significant only 5 times, with a peak at 0.7 ppm reached once. Hence, most produce will not be damaged in these situations, due to the

generally low levels and low temperatures. Therefore, based on the data it can be deduced that C_2H_4 is not a general problem in this kind of transportation.

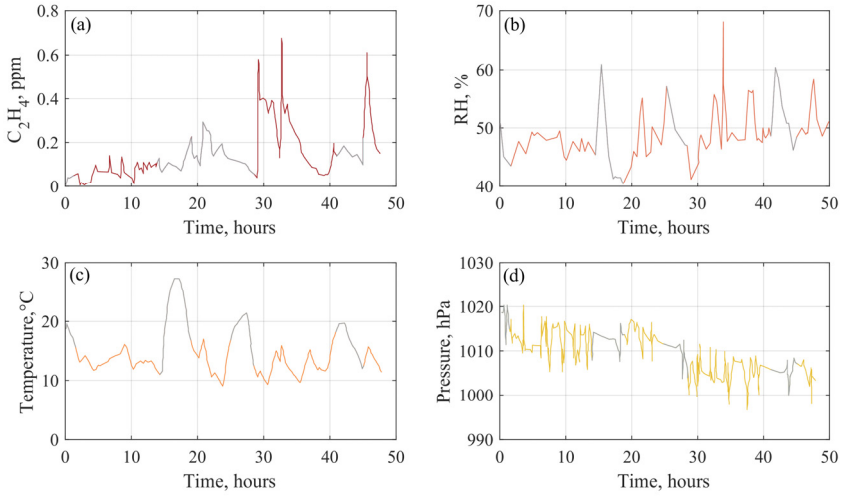

Figure 3-3 Measured C_2H_4 concentration (a), RH (b), temperature (c), and pressure (d) during a 48 hours transport session. Grey-coloured data indicate sensor outside truck or storage.

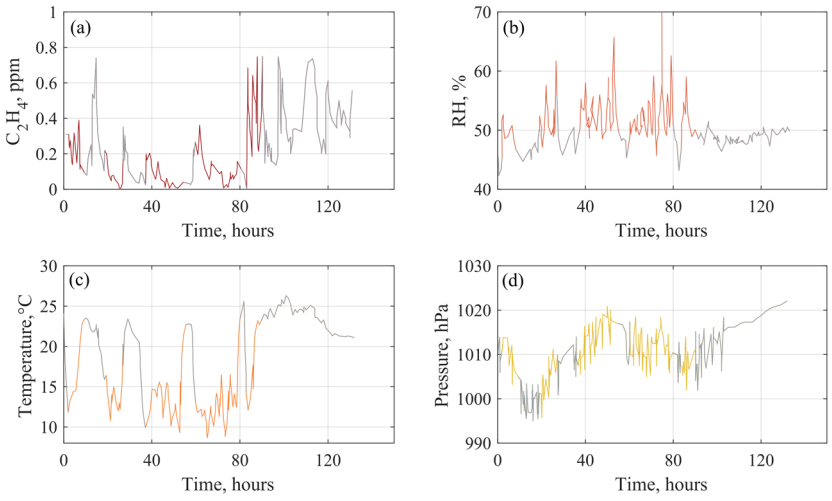

Figure 3-4 Measured C_2H_4 concentration (a), RH (b), temperature (c), and pressure (d) during a 128 hours transport session. Grey-coloured data indicate sensor outside truck or storage.

3.2.2. STORAGE CAMPAIGN

The storage facility measurement campaigns were conducted at Aarstiderne A/S, located in Barrit, Denmark. Two campaigns were carried out:

- A short-term campaign at the fresh produce bag level
- A long-term campaign at the facility environmental level.

Short-term campaign

The short-term campaign implied the recording of C_2H_4 levels at the bag level for three different fresh produce boxes that Aarstiderne is commercialising:

- Large fruit box – approx. 6 kg of 5-6 different fruits.
- Mixed box – approx. 4 kg of mixed fruits and vegetables.
- Vegetables box – approx. 4 kg of mixed vegetables.

Figure 3-5 shows the placement of the F950 handheld ethylene analyser from Felix Instruments, used to record the levels of C_2H_4 generated by the produce in the three types of boxes packed in a plastic bag, ready to be shipped.

The recorded C_2H_4 concentrations are plotted in Figure 3-6 and Figure 3-7. The general trend of the concentration is to increase as time passes, however this trend is not linear. Because different types of produce are packed inside the bags, C_2H_4 production rates will vary, both in terms of amount produced but also release time. In addition to this, depending on the produce, C_2H_4 is absorbed at a certain rate or not at all. A difference between produce was presented in 1.2.1, page 25.

Figure 3-5 Bag of mixed fresh produce and sensor used to record the generated C_2H_4 levels.

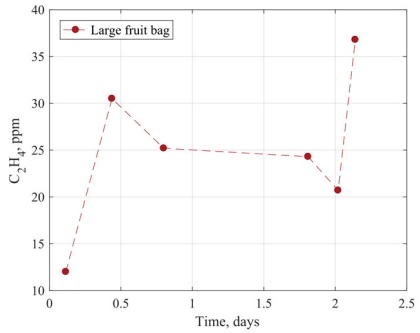

Figure 3-6 C_2H_4 levels generated by fruits packed in a large plastic bag during 2 days.

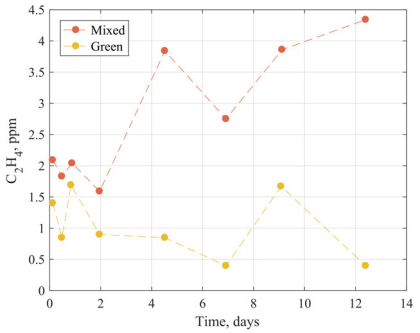

Figure 3-7 C_2H_4 levels generated by mixed fruits and vegetables packed in plastic bags during 12 days.

The high concentration of C_2H_4 released from the large fruits bag can be connected to the larger mass packed inside compared to the bags monitored in Figure 3-7. A second reason can be the type of fruits, which most frequently are climacteric. These have a high C_2H_4 release rate when ripening, as they go through a ripening stage even postharvest.

These short-term campaigns give an insight into the concentrations of C_2H_4 being generated at the fresh produce case level and being released in the storage facility enclosure when these are not packed. The next stage was to monitor the C_2H_4 levels in the whole environment of the facility, summarised in the following.

Long-term campaigns

As previously described, the long-term campaigns are mainly aimed at monitoring the C_2H_4 concentration and storage conditions at the environment level in the facility at Aarstiderne A/S. The layout of the whole storage facility and representative pictures of the storage room, where sensors were placed, can be found in Appendix A.

Paper B presents the methodology employed for recording data over the 12-days campaign, the processed results and their discussion. The main findings are briefly addressed in the following.
Figure 3-8 visually presents the concentrations of C_2H_4 and CO_2 over the 12 days, with clear delimitations between different activities taking place in the enclosure. Of most importance is the average concentration of C_2H_4, that the fresh produce were exposed to – 0.7 ppm, peaking at 1.5 ppm. These levels increase the potential for premature ripening and spoilage for most of the produce, as a large variety is highly sensitive to C_2H_4 even at low levels, facts emphasised also in Table 1-2. The temperature and RH averaged at 5.1ºC and 81%, respectively.

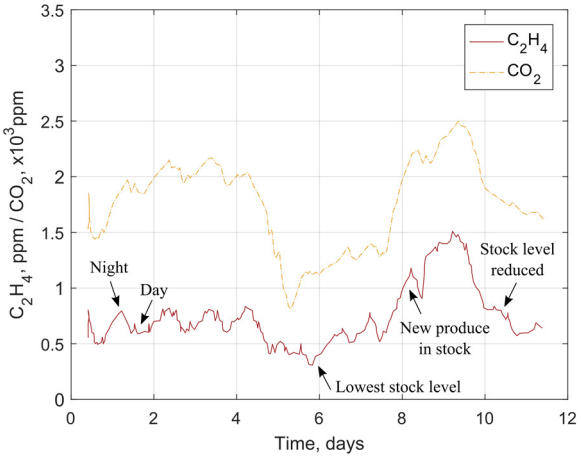

Figure 3-8 C_2H_4 and CO_2 concentration monitored throughout 12 days. Reprinted from Paper B.

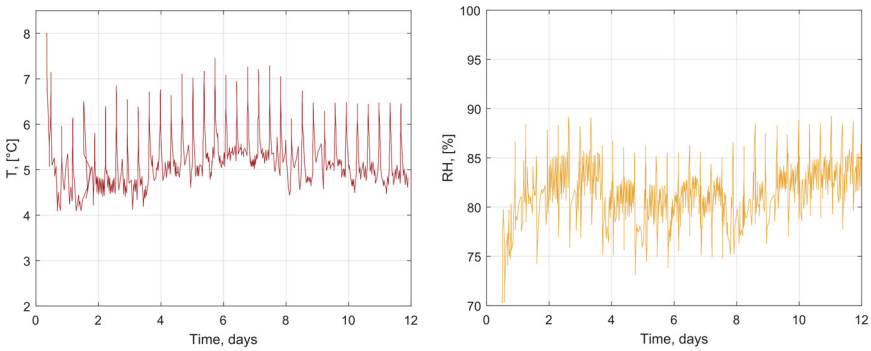

Figure 3-9 Recorded temperature (a) and RH (b) throughout measurement campaign. Reprinted from Paper B.

These field-determined values were further used to experimentally determine the kinetics of the photocatalytic reaction of C_2H_4 over TiO_2 thin films. Before getting to this, a simple 3D CFD simulation of a typical storage facility has been created to observe the transport of species and establish potential design criteria for the photoreactor. The optimal placement of an air-cleaning unit was of interest.

3.2.3. SPECIES TRANSPORT

At this stage, the photoreactor was targeted to be installed on the facility's ceiling or on the sidewalls at a sufficient height to be above the stacked cases of fresh produce. The risk at this point is that the targeted C_2H_4 will not diffuse to the needed area, due

to the slow diffusion of species in air and due to low ventilation. Inside the enclosure, the ventilation cannot be intensified, as this can negatively affect the working environment of employees. A quick estimation of diffusion time of species was made, making use of Einstein's diffusion equation (45):

$$t = \frac{\delta^2}{2\mathcal{D}_{AB}} \qquad (3.1)$$

where t – diffusion time, s
δ – diffusion distance, cm^2
$\mathcal{D}_{AB}$ – binary diffusivity of species A in species B, cm^2/s

To determine the diffusivities of both C_2H_4 and CO_2 in air at 5ºC the Chapman-Enskog kinetic theory for binary mixtures was applied, according to:

$$\mathcal{D}_{AB} = 0.0018583\sqrt{T^3\left(\frac{1}{M_A}+\frac{1}{M_B}\right)}\frac{1}{p\sigma_{AB}^2\Omega_{\mathcal{D}_{AB}}} \qquad (3.2)$$

where T – Temperature, K
M_i – Molecular weight, g/mol
p – Pressure, atm
σ – Collision diameter, Å
Ω – Collision integral, dimensionless

The parameters σ_{AB} and $\Omega_{D,AB}$ are determined by Lennard-Jones parameters of species A and B. For further details, the reader is referred to (46).

As the height of the storage facility is 4.7 m, the diffusion time was evaluated across a distance of 4.5 m, taking into account the space occupied by a potential cleaning unit. Figure 3-10 plots the diffusion time of the C_2H_4 and CO_2, via (3.1) and shows that under conditions of pure diffusion C_2H_4 and CO_2 travel the distance to the top of the facility in approx. 10 and 15 days, respectively. This confirms the potential risk of the species not reaching the cleaning unit, and thus the active surfaces where C_2H_4 can be degraded. The situation presented here can be regarded as a worst-case scenario, since no flow entrainment was considered, only pure diffusion.

To go a step further, and evaluate the enclosure environment under more realistic conditions, the flow pattern entrained by the ventilation system was modelled, thus giving an insight into how this affects the C_2H_4 diffusion and convection from the generating surfaces to the top of the enclosure. A 3D geometry was generated in Autodesk Inventor 14 based on the layout presented in Appendix A, complying with the enclosure's dimensions of 12x18x4.7 m^3, and accounting for the presence of stacks of different sizes. The geometry is presented in Figure 3-11.

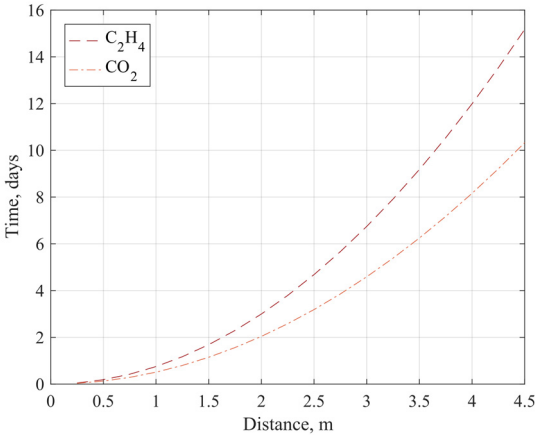

Figure 3-10 Diffusion time of C_2H_4 and CO_2 across the height of the storage.

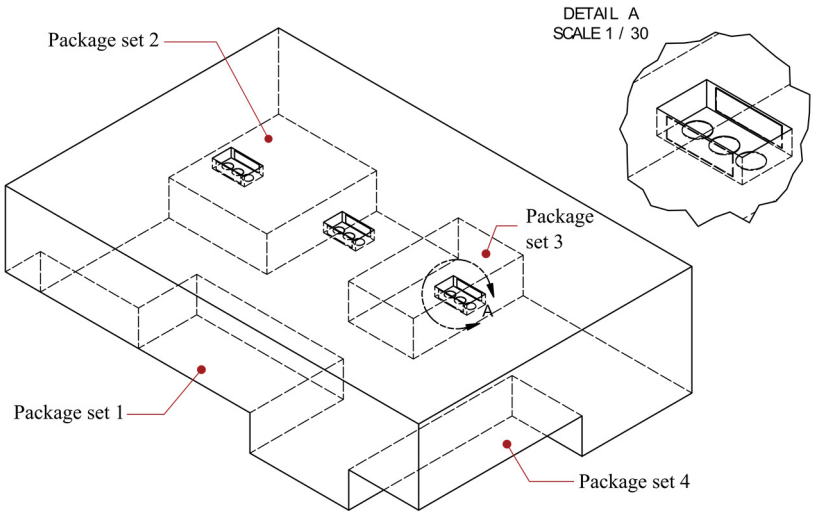

Figure 3-11 Storage facility geometry with zoomed view of modelled ventilation units. Scale 1:80.

The ventilation system resembles the one mounted on the ceiling of the room, namely three different units with two side air inlets and three fans at the bottom. The data-sheet, found in Appendix B, was used to dimension these, as well as to determine the air flow rate of the inlet. No doors were included in the computational domain, thus there is no exchange of air with adjacent rooms.

The meshing strategy adopted was based on an unstructured mesh, generated using ICEM CFD. To capture the slow diffusion of species an inflation layer, consisting of 8 stages, was placed at the C_2H_4-generating surfaces, namely on the top surface of the stacks. In addition, a high-density mesh was generated in areas where high gradients are expected, which are at the ventilation units. Furthermore, wastage of computational effort was targeted by avoiding unnecessary refinement in interior regions of minimal interest. As only the transport trends of the species were of importance, no extra focus has been put on generating the mesh and no high accuracy was targeted. The description of the meshing strategy is well represented in Figure 3-12, which shows a vertical cut through the meshed computational domain, capturing both a ventilation system and two sets of packages. The mesh generated in Figure 3-12 has a coarse refinement and is built out of 1.2 million cells. The aforementioned high-density regions are to be observed around the sets of packages and a ventilation unit.

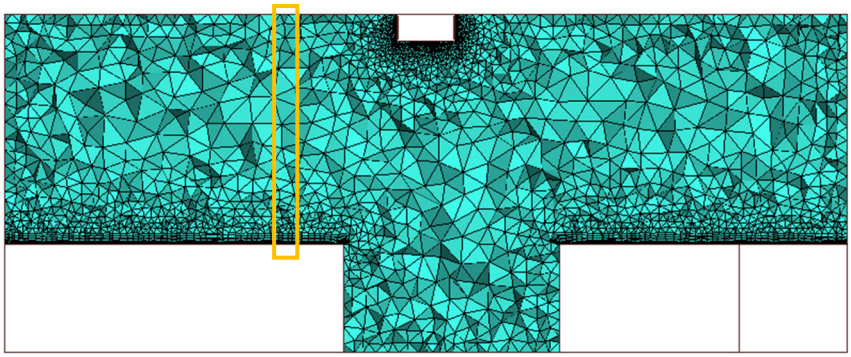

Figure 3-12 Cross-section of the meshed computational domain. Orange rectangle: data extraction location.

The flow problem was defined both in terms of air flow and species transport. The species involved were air and C_2H_4. The flow domain had ten inflows and nine outflows. Thus, suitable fluid flow boundary conditions (BC) were defined to accommodate the fluid behaviour upon entering and leaving the domain. As indicated in the data sheet, the ventilation unit has an input airflow of 4010 m^3/h, which corresponds to a mass flow rate, $\dot{m}_{air,\,in}$, of 0.70683 kg/s, or to a velocity of 1.68 m/s. This data on the air entering the enclosure has been used to define the mass flow inlet BC. The circular outlets, corresponding to the ventilation units, were defined as simple pressure outlets with zero static pressure, $p_{static,\,out}$. Hence, the BC for each ventilation unit are:

$$\begin{cases} \dot{m}_{air,in} = 0.706833\ kg/s \\ p_{static,out} = 0\ Pa \end{cases} \qquad (3.3)$$

where $\dot{m}_{air,\,in}$ – air inlet mass flow rate, kg/s
$p_{static,\,out}$ – outlet static pressure, Pa

The fluid material is composed of air, CO_2 and C_2H_4. As already mentioned, the species sources are defined at the top of each package set as mass flow inlets with specified species mass fraction to correspond to the overall generation rate of C_2H_4 and CO_2. It was reported that approx. 2400 kg of apples were stored during the first day of the campaign. Hence, for the simulation, it was assumed that inside the room 2400 kg of Golden Delicious apples generate C_2H_4 and CO_2. At 5ºC this type of apples have the following C_2H_4 and CO_2 generation rates (47):

Table 3-3 Species generation rates for apples at 5ºC (47).

	C_2H_4 generation rate	Respiration rate
Per 1 kg	2 – 25 µL/h	4 – 8 mL CO_2/h
Chosen rate [per kg]	20 µL/h	6 mL CO_2/h
Per 2400 kg	1.56e-08 kg/s	7.908e-06 kg/s

It was assumed that there are four packages of fruits generating C_2H_4, summing up to a total of 2400 kg of apples. To account for the difference in packages layout seen at the facility (Appendix A), the four sets, displayed in the geometry (Figure 3-11) contained a different amount of produce. Thus, different mass flow rates of species were defined, summing the C_2H_4 generation rate and the respiration rate (CO_2 generation), as follows:

Table 3-4 Mass flow rates for species inlets.

	Set 1	Set 2	Set 3	Set 4
$\dot{m}_{sp,\,in}$, [1e-07 kg/s]	19.809	29.7135	19.809	9.9045

Mass fractions of C_2H_4 and CO_2 were calculated based on the total mass flow rate and respiration rate per kg of produce. The C_2H_4 mass fraction was determined by subtracting the CO_2 mass fraction from unity. Thus,

$$\begin{cases} w_{C_2H_4} = 0.001969 \\ w_{CO_2} = 0.998031 \end{cases} \quad (3.4)$$

The processes taking place in the computational domain are regarded as being isentropic, meaning that these are adiabatic and reversible, thus there is no heat exchange and no energy transformation due to friction or dissipative effects. As a result of this assumption, the temperature is globally set to 278.15 K (5ºC) and there is no heat exchange with the external environment through the solid walls that border the flow geometry. In addition, the no-slip boundary condition is assumed at the walls. Therefore, the wall boundaries conditions can be expressed as:

$$\begin{cases} \Phi = 0\ W/m^2 \\ U = 0\ m/s \end{cases} \quad (3.5)$$

where Φ – heat flux, , W/m^2

U – velocity magnitude, m/s

The gravitational energy was neglected and due to C_2H_4 and air having similar densities, 1.18 kg/m^3 and 1.269 kg/m^3, respectively, the buoyancy force can be excluded from calculations.

The inlet flow conditions result in a turbulent flow, with a Reynolds number of approx. 52 000, entering the domain, thus the turbulent characteristic of the flow was modelled using the Shear-Stress Transport (SST) k-ω model, combining the k-ε and the k-ω models. The robustness and accuracy of the k-ω model in the near-wall region are blended with the freestream independence of the k-ε model in the far-field. An argument for using the SST k-ω model is the slow diffusion time of species being generated at the packages surfaces.

The evolution of C_2H_4 along the height of the modelled facility was evaluated after a converged steady-state solution was obtained. The C_2H_4 concentration is extracted from a plane, which sections the computational domain in half, including two sets of packages, two air inlets and one outlet. In addition, to display C_2H_4 concentration along the height of the room, data was extracted along the z-axis, at the location identified in Figure 3-12 with an orange rectangle.

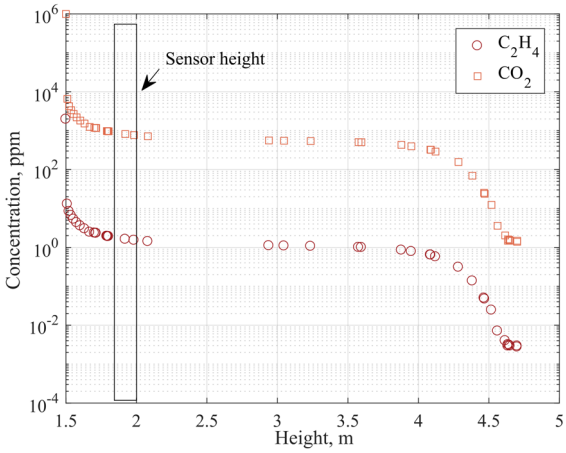

Figure 3-13 Distribution of species concentration along the height of the facility. 1.5 m and 4.7 m correspond to package surface and facility ceiling, respectively. Black rectangles shows the height of the C_2H_4 sensor during measurements.

The height, at which the C_2H_4 sensor was placed, during the measurements campaigns, was here taken into account to point out the agreement between the measured and the modelled concentration levels. Indeed, the average measured C_2H_4 concentration was 0.7 ppm, but it peaked at 1.5 ppm. Simulations showed a concentration of approx. 1 ppm at the height of interest. Deviations may occur due to

lack of air exchange with adjacent rooms, variations in stored produce and lack of daily activities inside the facility for the modelled enclosure. Nevertheless, it can be stated that the model was able to estimate the concentration of C_2H_4 to be managed.

3.3. CONCLUDING REMARKS

The investigations on the postharvest losses has led to three main results:

- The postharvest losses registered by the partners involved in the project are significant; both in the form of produce volume and profit. Thus, losses due to C_2H_4 is an issue they actively encounter, although it was not possible to quantify the fraction of losses attributed to C_2H_4. An air-cleaning device, capable of lowering C_2H_4 levels was considered to be of interest especially for the storage of fresh produce. The measurement campaigns showed that harmful levels arise in storages, rather than during short-haul transportation.
- The measurement campaigns conducted at Aarstiderne storage facility revealed average C_2H_4 levels of 0.7 ppm with peaks of 1.5 ppm. Correlating with the reported losses and the existing research it can be concluded that these levels negatively influence the shelf life of the stored fresh produce and flowers. Therefore, the postharvest industry can benefit from air-cleaning solutions, managing the C_2H_4 levels.
- CFD simulations confirmed a potential risk in utilizing an air-cleaning device in large enclosures, with minimal ventilation. It has been shown that C_2H_4 diffuses slowly. No flow entrainment leads to a troublesome degradation process, as C_2H_4 molecules might not be present at the active surface for oxidation. Using the already existing ventilation system, employed for cooling, not air exchange, constitutes a possible solution. However, it is expected for the degradation process to be inefficient, due to the slow diffusion of species or a very dilute flow to the device.

This concludes the study on postharvest storage conditions. The data gathered and generated here will be further used for a kinetic study of the photocatalytic reaction, to derive a rate law that describes the reaction, under varying conditions.

CHAPTER 4. KINETIC MODELLING

A kinetic study of the photocatalytic reaction of C_2H_4 over TiO_2 thin films is conducted, with the main goal of deriving a mathematical expression describing the degradation of pollutant with time, which can be readily implemented for photoreactor modelling. Part of this chapter is based on Paper B.

Prior to discussing the kinetic modelling of the reaction, the choice of photocatalyst will be addressed.

4.1. CHOICE OF PHOTOCATALYST

The technology chosen for degrading the plant-generated C_2H_4 employs TiO_2 as a catalyst. TiO_2 comes in different forms, whether it comes as a powder or catalyst support. In addition to this, several catalyst properties can enhance its potential of degrading VOCs, such as crystal structure, hydrophilicity, available surface area, substrate type and coating thickness (in case of immobilised catalyst). Although powdered catalysts exhibit a better photocatalytic activity, due to their large surface area, which translates in increased active sites number, immobilised catalysts are of interest because they exclude the necessity of filtering out the catalyst from the bulk flow, as it is the case of slurry reactors, for example.

To better understand the catalyst used, studies have been made in terms of crystal form and photocatalytic activity at the Danish Technological Institute, partner to the FRESH project.

Different substrate materials, albeit being coated with the same active material, can give rise to different supported photocatalysts. A reason for this can be the interaction of conductive substrate materials with the e^- from the e^--h^+ pairs, generated in the TiO_2 layer. As a result, the lifetime of holes is prolonged, by hindering the inevitable recombination process.
Moreover, in the case of photocatalytic surfaces it is important to consider which thickness of the catalyst layer will offer the best compromise between mechanical stability, deposition time and activity. Since the photogenerated e^- and h^+ have a limited lifetime and diffusion length, regardless of radiation wavelength and intensity, the activity is expected to be influenced by the thickness, with an optimum. This is attributed to a limited diffusion of the reactant gas through the catalyst film, regardless of wavelength and radiation intensity. This means that an increased thickness allows pollutant molecules to be exposed to a higher amount of oxidizing species, h^+, up to a certain limit. On the other hand, too low of a thickness leaves too many photons unabsorbed, and thus causes a decrease in activity. (48)

Different substrate materials were coated with TiO_2 of different thicknesses, δ_c. The substrates considered are listed in Table 4-1.

Table 4-1 Substrate material candidates.

Substrate	Property
Aluminium	Non-reflective, insulating surface due to natural oxide layer
Highly polished aluminium	Reflective, insulating surface due to natural oxide layer
Anodised aluminium	Insulating
Steel slide	Conductive

The porous TiO_2 thin films were deposited by reactive, pulsed DC magnetron sputtering using an industrial CemeCon CC800/9 SinOx coating unit with a chamber size of 850 x 850 x 1000 mm^3. The sputtering chamber was equipped with four magnetrons, at which a pulsed DC power of 2 kW was applied. The depositions were carried out in an Ar/O_2 atmosphere, where O_2 acts as the reactive agent for the TiO_2 film formation at a total pressure of approx. 400 mPa. To obtain stoichiometric TiO_2 thin films, the Ar/O_2 gas flow ratio was 350/150 cm^3/min. The substrates to be coated were mounted on a rotating sample stage, performing a two-fold planetary rotation, to ensure a uniform coating. Prior to the deposition, the chamber pressure was set to 4 mPa and the substrates were heated to the deposition temperature of approx. 423 K. The temperature was controlled by a resistive heater. Heating the plates beforehand alleviates the stress that will inevitably build up in the film. The deposition rate was 2.4 nm/min, and the films were synthesized at different thicknesses, depending on the deposition time. Two deposition processes were conducted, in order to coat the substrate candidates at the desired two thicknesses. Only the coating time differed for the two depositions, thus the procedure details given above are valid for both. The coating time of the two processes differed by a factor of three. The coating chamber consisted of six plate-towers, which were raised by three thin segments each, as shown in Figure 4-1. The substrates considered for the study were mounted onto the plate-towers, visible in Figure 4-1.

The thicknesses of the coatings were determined by Scanning Electron Microscopy (SEM) analysis. Cross-sectional area and top views are presented in Figure 4-2, both at 50k magnification. The coating that spent less time in the deposition chamber had a thickness of δ_c = 1.1 µm while the second surface, which was held in the chamber three times longer, had a thickness of δ_c = 3.1 µm. Hereafter, the 1.1 and 3.1 µm coatings will be referred to as “C1” and “C3”, respectively.

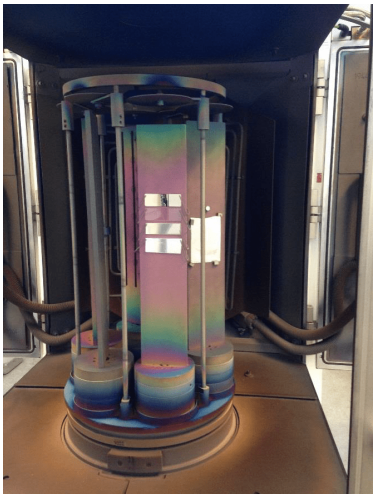

Figure 4-1 Coating chamber used for 1 and 3 µm thick depositions. Six plates onto which substrates are mounted.

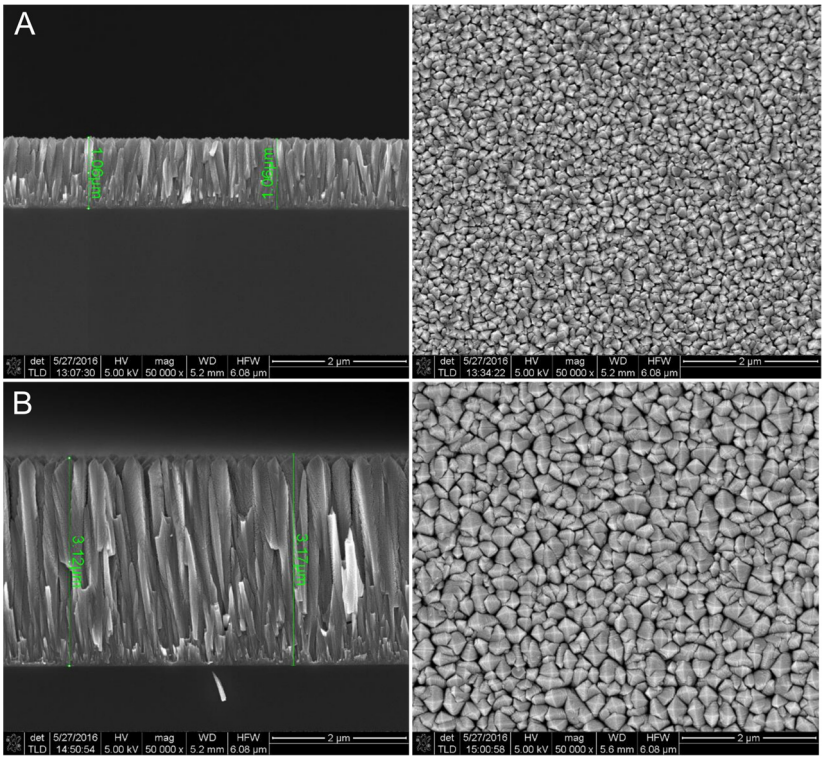

Figure 4-2 SEM analysis of coatings. (A) 1.1 µm. (B) 3.1 µm. Left column: cross-sectional area; right column: top view.

Two characterisation methods were employed to investigate the crystal structure of the coatings – X-ray Powder Diffraction (XRD) and Raman spectroscopy. It is desired for the coatings to exhibit anatase crystal structure, as the rutile form is less photocatalytically active.
C3 has not been investigated by XRD. As listed in Table 4-1 three Al-based substrates were coated, but only the simple Al plate underwent XRD investigations. It was assumed that the substrates will give rise to similar characteristics, regardless of nature. Thus, XRD obtained at 5 degrees grazing angle revealed only anatase peaks, in addition to expected substrate peaks, for C1 deposited on steel foil and aluminium plate. The XRD results are plotted in Figure 4-3.

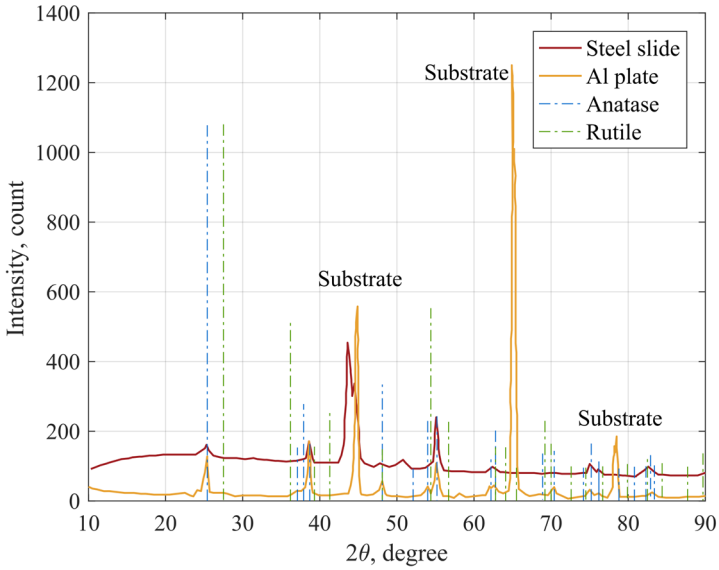

Figure 4-3 XRD at 5 degrees grazing angle characterisation of aluminium and steel foil substrates coated with 1 μm TiO_2. (-··-) Theoretical anatase and rutile peaks.

The assumption previously made was confirmed by Raman spectroscopy at 785 nm wavelength. Indeed, anatase peaks define the coatings, independent of substrate material and coating thickness. Raman spectroscopy revealed only anatase peaks for both thicknesses and all substrate types, as shown in Figure 4-4 and Figure 4-5. The Raman signal is sensitive to the focusing of the sample. However, the signals were significantly more intense for the thick coating. Moreover, considerable background signal was identified for the thin coating on Al-based substrate. It was unclear whether this was due to the nature of the substrate or if it can be associated with coating features. Nevertheless, the fact that this background signal was reduced in the case of the thick coating suggests it may indeed originate from the substrate.

Based on XRD and Raman spectroscopy it can be concluded that the substrate has no influence on the crystal structure of the TiO_2 coatings.

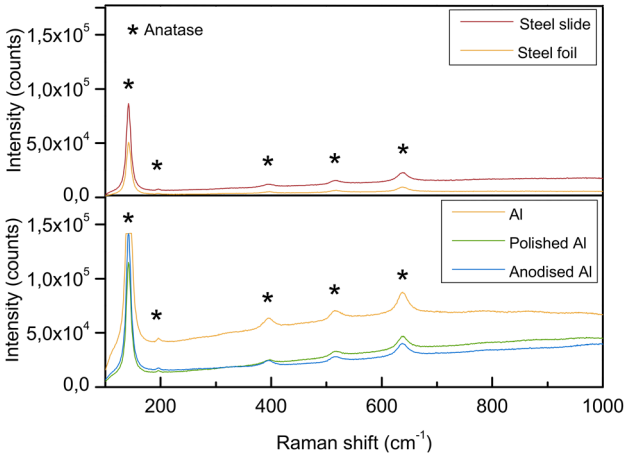

Figure 4-4 Raman spectroscopy plots of substrate materials coated with a 1.1 μm thick TiO_2 coating (C1).

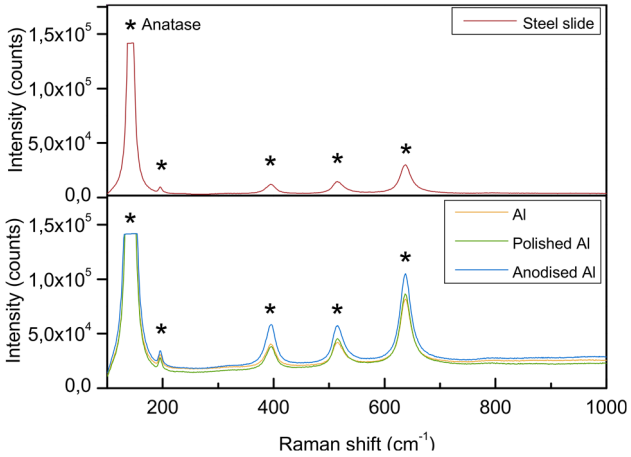

Figure 4-5 Raman spectroscopy plots of substrate materials coated with a 3.1 μm thick TiO_2 coating (C3).

The same substrate candidates, with δ_c = 1.1 and δ_c = 3.1 μm, are compared in terms of photocatalytic activity, in order to judge whether the substrate plays a role and observe if the activity can be enhanced with different substrates and increased δ_c. The photocatalytic activity is quantified based on the evolution of CO_2, due to lack of an C_2H_4 sensor at that time. The experimental conditions and procedure can be evaluated in Table 4-2.

Table 4-2 Experimental conditions for the photocatalytic activity investigations of substrate.

Sample area [cm^2]	17.5
Air-C_2H_4 ratio [cm^3/min]	125/250
RH [%]	~ 19
UV-A wavelength, λ_{UV} [nm]	365
UV-A intensity, I_{UV} [W/m^2]	67

The photocatalytic activity was evaluated in a batch reactor. The reactor used will be described at a later point, in the next chapter.

Figure 4-6 plots the photocatalytic activity based on production of CO_2, as a results of catalyst irradiation. The substrate material appears to have no significant effect on the oxidation potential of the catalyst. Nevertheless, increasing δ_c enhances the potential.

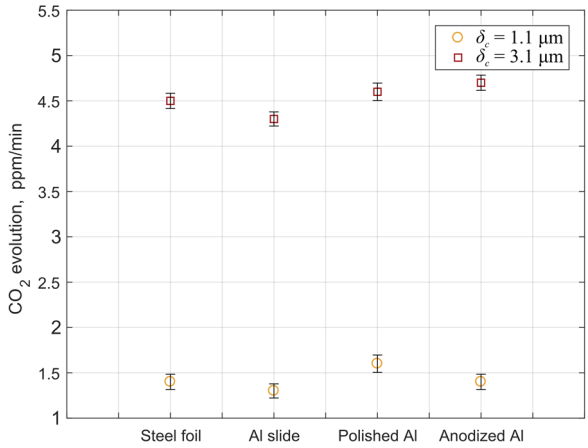

Figure 4-6 Quantified photocatalytic activity based on CO_2 production for different substrate materials coated with a 1.1 and 3.1 µm thick TiO_2 layer.

The choice of catalyst layer comes down to a trade-off between deposition time, mechanical stability and optical properties. As optical properties have not been evaluated, the choice of catalyst was based on the experimentally determined activity. Considering deposition time and cost, as well as the key factor of photocatalytic activity, the catalyst further used is a 1.1 µm TiO_2 coated Al plate. This photocatalyst was used to determine reaction kinetics and for the construction of the photoreactor prototype.

In the following, the experiments conducted for deriving reaction kinetics will be addressed.

4.2. REACTION KINETICS

Similar to the previous section, the present one will be a mixture of results published in Paper B and results that have been an essential part of the research, although unpublished.

First, the experimental setup and procedure used for monitoring the photodegradation of C_2H_4 over TiO_2 thin films will be briefly presented.

4.2.1. EXPERIMENTAL METHODS

A comprehensive view of the experimental setup employed throughout the kinetics studies is pictured in Figure 4-7 and the equipment used is listed in Table 4-3. The main element of the experimental setup is the photocatalytic oxidation (PCO) unit (7). The PCO unit is a stainless steel batch reactor with a borosilicate glass top to allow irradiation of the catalyst. Its volume is 6.68e-04 m^3. Other elements are the CO_2 (8) and VOC sensors, humidifier (2), mass flow controllers (MFC) (5), O_2 and C_2H_4+N_2 gas bottles (1), UV-A source composed of 6 LEDs (6) and a UV sensor (9). For extra details on the used equipment and a schematic view of the setup, the reader is referred to Paper B, Section 2.2.

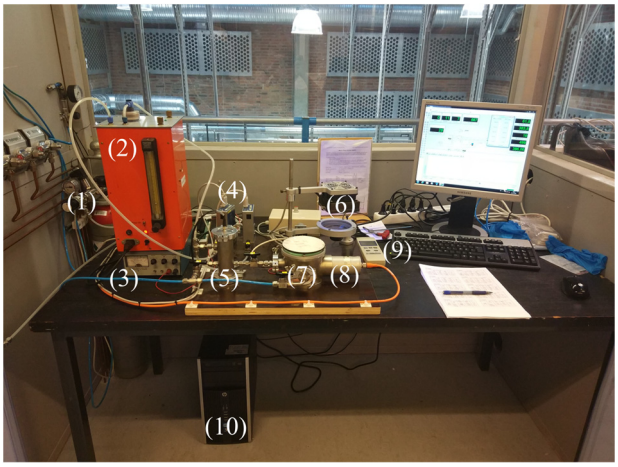

Figure 4-7 Experimental setup. Numbered equipment defined in text.

Two variations of this setup were used. In the initial phase of the kinetic study, the setup had no VOC sensor. Also, the catalyst was placed on a substrate table, over the CO_2 sensor, to achieve a higher surface incident radiation, as shown in Figure 4-9. The TiO_2-coated Al plate had a surface area of 50 x 35 mm^2. Due to the lack of a VOC sensor, the photocatalytic reaction was evaluated in terms of products, namely production of CO_2, recorded by the Vaisala CO_2 sensor.

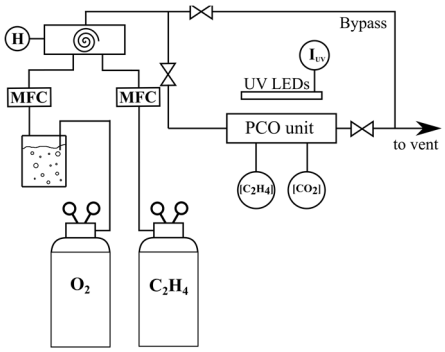

Figure 4-8 Schematic view of the experimental setup.(49)

Table 4-3 Experimental equipment numbered according to Figure 4-7.

(1)	Gas bottles (O_2; C_2H_4 in N_2)
(2)	Humidifier
(3)	Power supply
(4)	MKS GE50A mass flow controllers
(5)	Mixer
(6)	UV-A source
(7)	PCO unit
(8)	Vaisala GMP343 CO_2 probe
(9)	UV sensor
(10)	PC unit

For the second stage of the kinetic study the experimental setup was reconfigured. A VOC sensor was added, in order to monitor the levels of C_2H_4, in addition to CO_2. Moreover, the catalyst was placed at the bottom of the chamber, under the C_2H_4 sensor, where no shadow was casted by the CO_2 probe, as shown in Figure 4-10. This change conditioned the surface area of the Al plate, which had to be reduced to 40 x 25 mm^2. The author would like to emphasize that the VOC sensor is a non-selective photo-ionisation detector (PID), meaning that it targets all VOCs with a ionisation potential < 10.6 eV, amongst which C_2H_4, characterised by a ionisation potential of 10.5 eV, according to NIST (50).

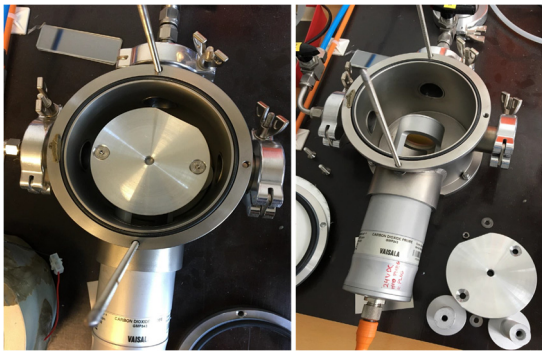

Figure 4-9 PCO unit with (left) and without (right) substrate table, where catalyst plate was placed.

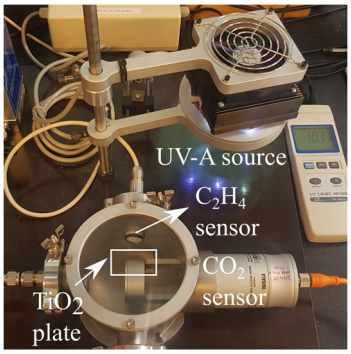

Figure 4-10 Top view of the reaction chamber and UV source. (49)

Regardless of setup configuration, each experiment followed the same procedure, summarised hereafter. The gas stream of oxidising agent, O_2, passed through the humidifier, in order to set the desired RH. Both gas streams, O_2 and C_2H_4, flowed through the mass flow controllers, where their mass flow was set according to the targeted concentration of C_2H_4 in the gas stream entering the PCO unit. The two

streams were mixed into one single main stream by the mixer, in order to obtain a homogeneous gas flow to be transported to the PCO unit for oxidation. Due to the non-selectivity of the VOC sensor, pure O_2 was be mixed with the C_2H_4 stream, to ensure that the recorded concentration corresponds to C_2H_4.

All experiments started with a precleaning stage, consisting of flushing the PCO unit with pure O_2 and irradiating it until the measured VOC concentration decreased to zero. In the example plotted in Figure 4-11 the concentration of VOC at the start of the precleaning stage was approx. 6 ppm. This means that C_2H_4 was present in the gas contained in the batch reactor, most likely from a previous experiment.

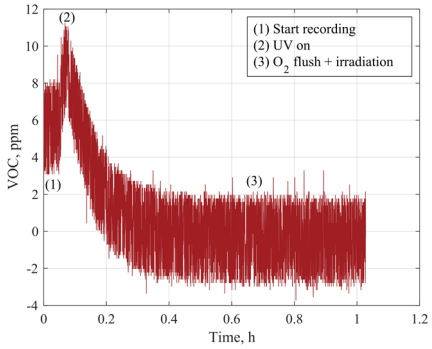

Figure 4-11 Example of precleaning stage.

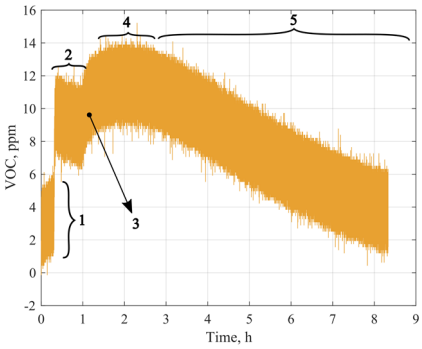

Figure 4-12 Typical experimental data. VOC concentration vs. time at C_0 = 10 ppm, RH = 80%, I_{UV} = 60 W/m^2.

When the chamber started being irradiated, the concentration of VOC began increasing for a short period, which was surprising. This behaviour was observed for all conducted experiments. It was assumed that VOC molecules adsorbed to the surfaces of the chamber desorb into the gas phase. At the same time the molecules are oxidized, as these come into contact with the activated TiO_2. When the VOC concentration approached zero, the UV source was turned off and a second flush was started. The chamber was flushed with the gas mixture containing the desired initial C_2H_4 concentration, C_0. As species concentration and RH value reached a steady state, the flushing was stopped. The chamber inlet and outlet were closed via installed valves, thus the chamber operated as a batch reactor from this point on. The irradiation was restarted and the degradation process initialised. This proposed experimental method contained 5 stages, excluding the pre-cleaning stage, as shown in Figure 4-12. The stages, numbered in accordance with Figure 4-12, are:

1. Equipment warm-up.
2. Reaching parameters steady state.
3. UV source turned ON.
4. Desorption.
5. Degradation.

4.2.2. KINETIC STUDIES

The kinetics of photocatalytic reactions were discussed in Section 2.4. The stoichiometric reaction and the Langmuir-Hinshelwood rate law are given here again for easy reference:

$$C_2H_4 + O_2 \rightarrow CO_2 + H_2O \qquad (4.1)$$

$$r = \frac{dC}{dt} = \frac{k_r K_{abs} C}{1 + K_{abs} C} \qquad (4.2)$$

This rate law was fitted to the experimental results, deriving the reaction constants k_r and K_{abs}.

Kinetic study I

The first set of experiments conducted for monitoring the degradation of C_2H_4 over TiO_2 in the batch reactor presented was handled at DTI, FRESH partner. The set contained three experiments operated under the conditions listed in Table 4-4.

Table 4-4 Experimental conditions for set 1.

Exp.	$\dot{q}_{air}$ cm^3/min	$\dot{q}_{C_2H_4}$ cm^3/min	$[C_2H_4]_0$ ppm	$[CO_2]_0$ ppm	RH %	I_{UV} W/m^2
1	400	100	2000	325		
2	125	250	6670	145	18.8	67
3	100	400	8000	92		

C_2H_4 was provided to the chamber from a gas bottle containing a mixture of 10 000 ppm of C_2H_4 in N_2. Considering the mass flow rates of the used MFCs and the C_2H_4 concentration of the gas bottle, the minimum C_0 achievable with the first setup configuration was 196 ppm. As previously mentioned, the degradation of C_2H_4 during the initial experiments was evaluated based on the production of CO_2. The curves describing the production of CO_2, as the photocatalytic degradation of C_2H_4 progressed are plotted in Figure 4-13.

The reaction rate expressed in terms of CO_2 gives the production and consumption of the other species, according to (4.1), as follows:

$$r = \frac{d[CO_2]}{dt} = -2\frac{d[C_2H_4]}{dt} = -\frac{2}{3}\frac{d[O_2]}{dt} = \frac{d[H_2O]}{dt} \qquad (4.3)$$

It has been discussed in Section 2.4 that the LH rate model can be reduced to a zero order rate law at sufficiently high pollutant concentrations.

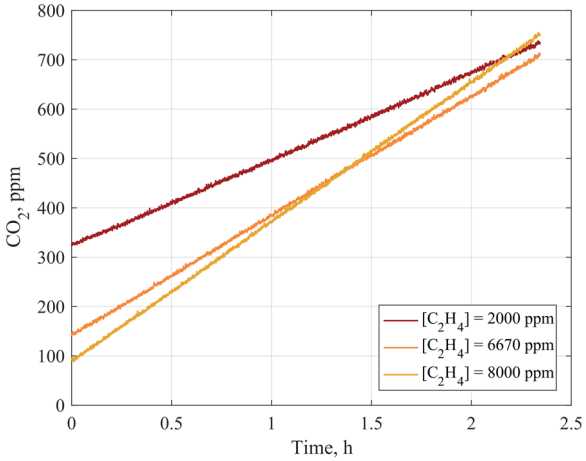

Figure 4-13 CO_2 production as a results of photocatalytic degradation of C_2H_4 under different initial concentrations. Experimental set 1.

The differential form of the rate law becomes:

$$r = \frac{d[CO_2]}{dt} = k_{r,zero} \qquad (4.4)$$

where $k_{r,zero}$, ppm/s, is the reaction rate constant corresponding to the zero order rate law. To be noted is that the reaction rate is positive due to handling a production of species, namely CO_2. Rearranging and integrating (4.4) allows the determination of product concentration at any time after the reaction start, according to

$$[CO_2] = [CO_2]_0 - k_{r,zero}t \qquad (4.5)$$

Figure 4-14 shows the fit of the zero order rate law to the experimental data for experiment 2 (see Table 4-4). The fit for the other two experiments can be seen in Appendix C.

The applied rate law estimates the production of CO_2 very well, however a few issues are to be discussed here. It was concluded based on these first experiments that at these high concentrations of compounds the degradation reaction follows a zero order rate law, making the kinetics independent of C_0. This is against expectations, as it has been many times reported that such photocatalytic reactions are affected by initial pollutant concentration, H_2O content and radiation intensity. This does not mean the investigated experiments are incorrect or that the applied kinetic approach was wrong. These results come to show that at high enough concentrations a shift in reaction rate towards a zero order rate law may happen, as it has been already observed by (16, 51).

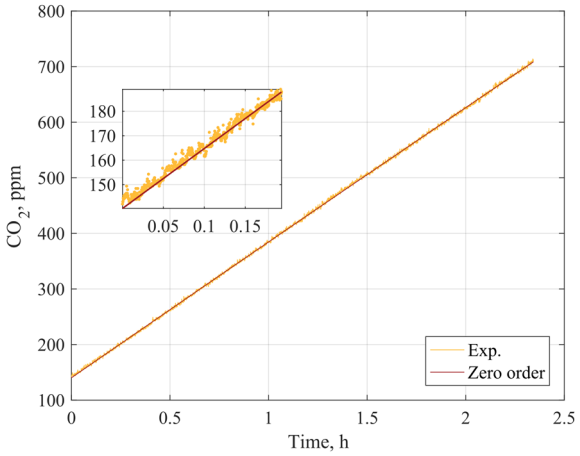

Figure 4-14 Zero order rate law fit to experimental data 2. $[CO_2]_0$ = 145 ppm, $[C_2H_4]$ = 6670 ppm, RH = 18.8%.

Moreover, due to the reaction shift the derived kinetic data are not valid for concentrations encountered in real life conditions. Hence, the kinetic study based on these three experiments is not reliable, when operating conditions change significantly. To be noted is the low RH at which the experiments have been performed: 18.8%. This was a few degrees of magnitude lower than the RH conditions fresh produce are stored at, approx. 80%. Lastly, the C_2H_4 concentrations considered are significantly higher than those recorded in storage facilities. It is important to derive kinetics at conditions under which fresh goods are stored or transported.

These findings caused a rethinking of the kinetic approach, in terms of experimental procedure. The configuration of the experimental setup used further was described in Section 4.2.1.

Kinetic study II

To achieve a more diluted gas stream, compared to the previous kinetic study, a 700 ppm C_2H_4 in N_2 gas bottle was used. This change to the setup allowed the concentration of the reactor inlet gas to be as low as 10 ppm. This value is far more appropriate than the concentrations used in the previous kinetic study. In addition, the installation of a VOC sensor allows the C_2H_4 concentration to be monitored, in contrast to the previous study.

Two investigations have been conducted during this kinetic study. In addition to describing the reaction kinetically, the effect of initial C_2H_4 concentration, C_0, and incident surface radiation, I_{UV}, have been analysed, under the conditions listed in Table 4-5.

Table 4-5 Experimental conditions for the kinetic study, and effect of parameters on kinetics. Reused from Paper B.

	C_0 (ppm)	I_{UV} (W/m^2)	$\dot{q}_{in}$ (cm^3/min)	RH (%)
Kinetic study and Effect of C_0	11.6 – 27	60	310 – 510	80
Effect of I_{UV}	10	39 – 57	510	80

The raw data of the recorded degradation of VOC for the five conducted experiments is plotted in Figure 4-15. Before using the degradation curves for kinetic purposes, the data has been smoothed out, due to the noise present in the data, which makes the fitting process cumbersome. The smoothing function applied to the data sets in MATLAB was based on a robust local regression using weighted linear least squares and a 2nd degree polynomial model. The smoothed data is plotted in Figure 4-16. Figure 4-15 and Figure 4-16 clearly show that the concentration has an effect on the degradation of C_2H_4 over TiO_2, visible in the change in slope of the degradation curves.

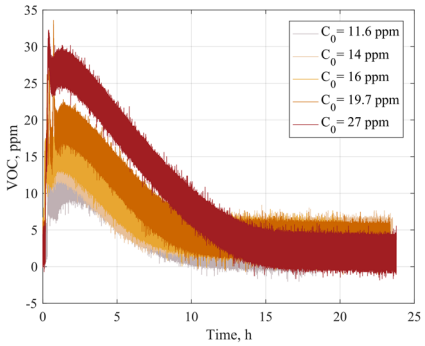

Figure 4-15 Raw degradation curves recorded during the photocatalytic process, for kinetic study and initial concentration effect upon kinetics.

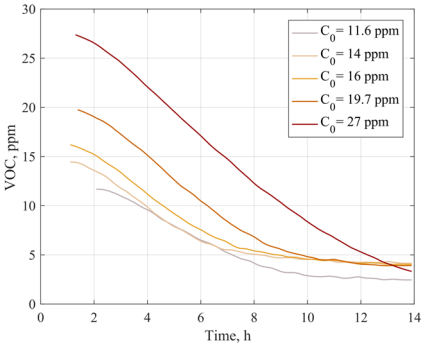

Figure 4-16 Smoothed degradation curves. Data plotted from UV source turn on up to concentration reaching a constant lower value.

The same kinetic approach as before has been applied, but the reaction has been evaluated in terms of recorded VOC, thus the rate law considered is:

$$-r = \frac{dC}{dt} = k_r \frac{K_{abs} C}{1 + K_{abs} C} \qquad (4.6)$$

Integrating Eq. (4.6) results in:

$$\frac{1}{k_r K_{abs}} ln\left(\frac{C_0}{C}\right) + \frac{1}{k_r}(C_0 - C) = -t \qquad (4.7)$$

The linearized form of Eq. (4.6) brings along numerical constrains when evaluating the concentration of species *C*, due to the variable being both inside and outside of the logarithm. Thus, an explicit solution to Eq. (4.7) does not exist. A method of solving Eq. (4.7) explicitly was proposed and evaluated in Paper A and it will not be reiterated here. To avoid solving Eq. (4.6) explicitly one can fit it to the experimental data through a non-linear curve-fitting algorithm after integrating the differential equation using an Ordinary Differential Equation (ODE) solver. Both the LH law and a pseudo-first order rate model were fitted to the experimental data, in order to verify if one is superior to the other in estimating the degradation of pollutant. As previously explained, when the molar concentration of model compound is sufficiently low, Eq. (4.6) can be reduced to a pseudo-first order reaction rate, reiterated here for easy reference.

$$r = \frac{dC}{dt} = k_{app}C \qquad (4.8)$$

The experimental and modelled degradation curves are plotted in

Figure 4-17 and Figure 4-18, for the pseudo-first order and the LH rate models, respectively. The determined kinetic parameters, resulted from fitting the rate laws are listed in Table 4-6, together with the R^2-value corresponding to each data set for judging the goodness-of-fit. It should be emphasized that the kinetic parameters derived in the present study are intrinsic. Hence, these are inherently dependable on the conditions under which these have been determined.

Table 4-6 Derived kinetic parameters and R^2-values corresponding to the kinetic models being fitted to experimental data. Data partly reprinted from Paper B with unit change.

C_0 (ppm)	k_{app} (s^{-1})	R^2_{app}	k_r (ppm s^{-1})	K_{abs} (ppm^{-1})	R^2_{LH}
11.6	4.304e-05	0.9715	9.602e-04	1.698e-02	0.9696
14	3.700e-05	0.9433	9.077e-03	1.200e-02	0.9525
16	3.871e-05	0.9695	3.631e-03	9.587e-03	0.9703
19.7	4.021e-05	0.9709	1.223e-01	3.261e-04	0.9698
27	3.434e-05	0.9473	1.981e-01	1.720e-04	0.9459

The high R^2-values listed in Table 4-6 demonstrate that the photocatalytic degradation can be modelled by using either the LH rate model or a pseudo-first order rate law, with high accuracy. For the next two studies, the LH model was employed.

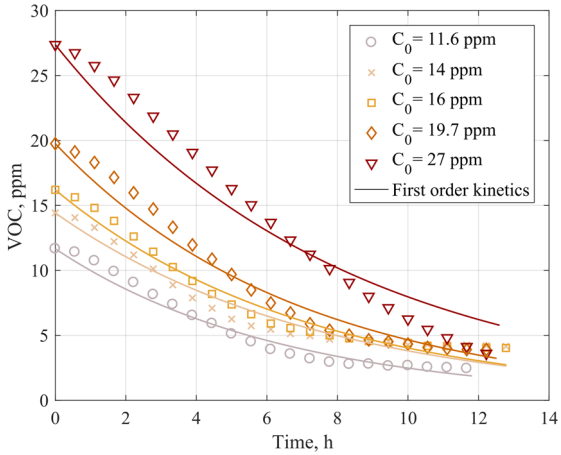

Figure 4-17 Degradation curves estimated by pseudo-first order rate law vs. experimental data for varying initial concentration. (49)

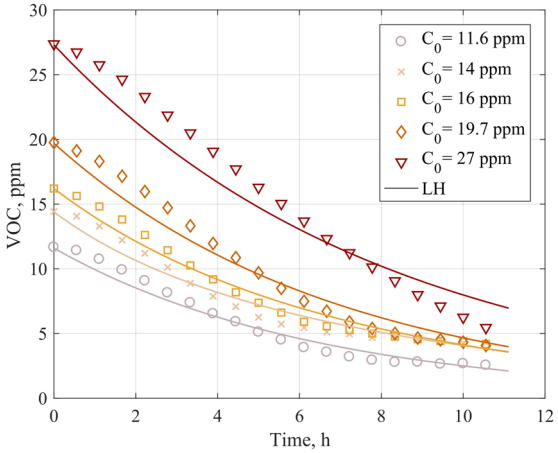

Figure 4-18 Degradation curves estimated by LH rate model vs. experimental data for varying initial concentration. Reprinted from Paper B.

To extend the capability of the derived kinetic model, its response to different initial concentrations and radiation intensities was investigated. The results are presented in the following.

Effect of C_0 and I_{UV}

To investigate the effect of C_0 on the reaction kinetics the same degradation data generated for deriving the kinetic parameters (Figure 4-16) were analysed. Hence, the determined kinetic parameters listed in Table 4-6 were used for this investigation. The

five kinetic parameter pairs (k_r, K_{abs}) were plotted against the corresponding initial concentration of C_2H_4 in Figure 4-19. A dependence that incorporates both kinetic parameters, through the reaction rate, is graphically presented in Figure 4-20.

The dependence of the two kinetic parameters, k_r and K_{abs}, is well approximated by exponential fit, with R^2-values of 0.8287 and 0.913, respectively. The derived mathematical relations that describe the influence of C_0 on reaction kinetics are:

$$k_r = 3.02e - 03e^{0.151C_0} \quad (4.9)$$

$$K_{abs} = 0.1864e^{-0.1987C_0} \quad (4.10)$$

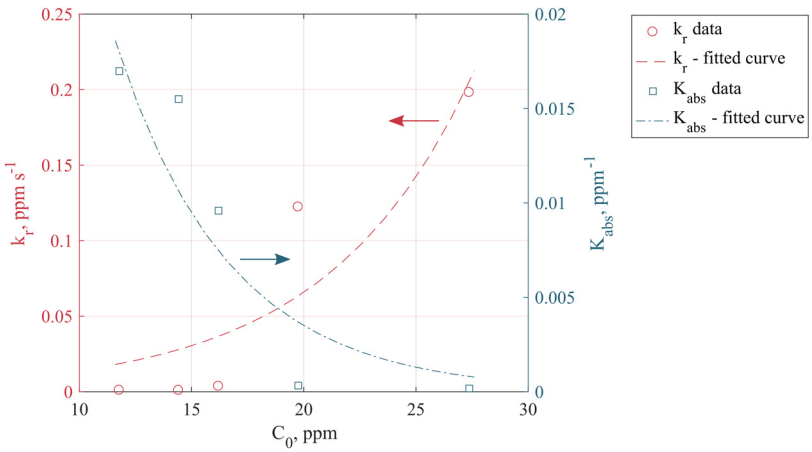

Figure 4-19 Dependence of kinetic parameters on initial C_2H_4 concentration, C_0. Plot generated by using data from Paper B.

The reaction rate, calculated using the derived kinetic parameters, increases with increasing concentration of C_2H_4, as seen in Figure 4-20. This dependence is in agreement with findings reported in literature where photocatalytic reactions were studied (52, 53). Furthermore, the steep rise of the reaction rate with increasing initial concentration at low levels of VOC, followed by a milder variation is a common behaviour for LH-type reactions (53). This increase is attributed to a higher availability of C_2H_4 molecules at the active surface, due to the higher concentration. However, as the catalyst surface becomes oversaturated, the reaction rate curve is expected to reach a plateau. While conducting studies of the photocatalytic oxidation of four different VOCs, Kim and Hong (53) have reached this plateau during their experiments.

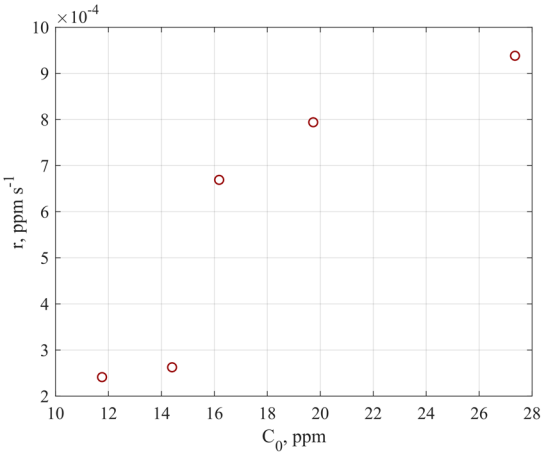

Figure 4-20 Dependence of reaction rate, r, on initial C_2H_4 concentration, C_0. Plot generated by using data from Paper B.

Based on the literature review, it was observed that although irradiation modelling is conducted when simulating photoreactors, only the distribution of the radiation on the catalyst is targeted. Many times the dependence of reaction rate on surface incident radiation is disregarded. One of the objectives of studying the photocatalytic reaction was the derivation of a mathematical relation linking the radiation to the rate of reaction. For this study, the radiation of the catalyst was considered of high importance because it is the physical phenomenon, which generates the oxidizing species, the hydroxyl radicals $OH^{\cdot}$. Figure 4-21 summarizes the mechanism considered here, emphasizing the importance of accounting for the influence of radiation.

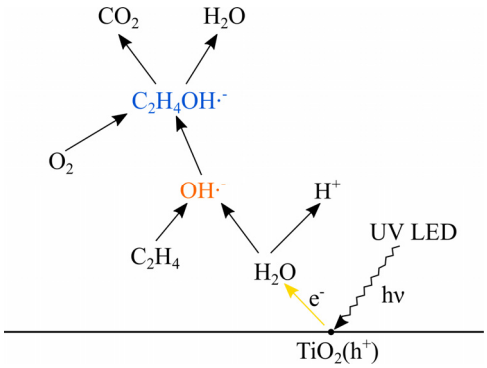

Figure 4-21 Reaction mechanism considered for the kinetic study.

According to this mechanism the photons generate an e^--h^+ pair in the catalyst, which further reacts with the H_2O molecules present at the catalyst surface to produce the $OH^{\cdot}$ radical, capable of reacting with the adsorbed C_2H_4.

As the kinetics are intrinsic, depending on reaction conditions, many of the models presented in literature are not valid for the present application. Employing the batch reactor, a relationship between rate and irradiation was successfully derived. As listed in Table 4-5, the experiments conducted for observing the effect of surface incident radiation on the reaction rate, took place at constant C_0 = 10 ppm and varying incident radiation, ranging from 39 to 57 W/m^2. The recorded degradation curves are shown in Figure 4-22.

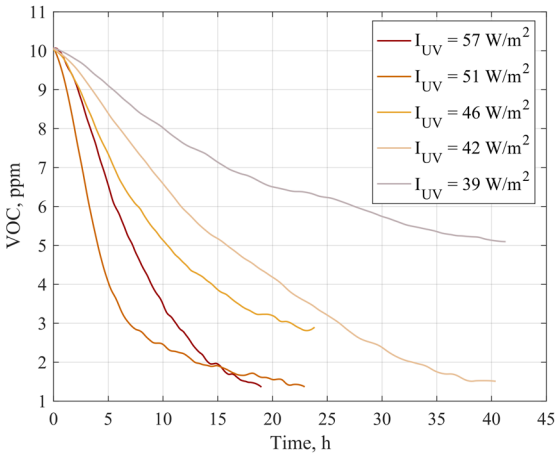

Figure 4-22 Degradation curve as a function of varying surface incident radiation for constant initial concentration, C_0.

The experiments were run for different time intervals. However, it can be observed that the slope of the degradation increases with increasing radiation incident on the TiO_2 surface. Plotting the reaction rate as a function of the surface incident radiation (Figure 4-23) allows for a mathematical relation to be derived. The linear fit estimates the dependence between the two parameters with R^2 = 0.966, according to:

$$r = 5.105e-06 I_{UV} - 1.582e-04 \qquad (4.11)$$

Besides allowing the reaction to be described kinetically, the experimental study revealed potential deactivation of the TiO_2 thin films coated on the Al substrate. This was a setback during the study conducted, as a number of used plates have diminish their activity before experimental sets could be finalised. Unfortunately, due to this, the influence of water vapour on the reaction rate could not be investigated.

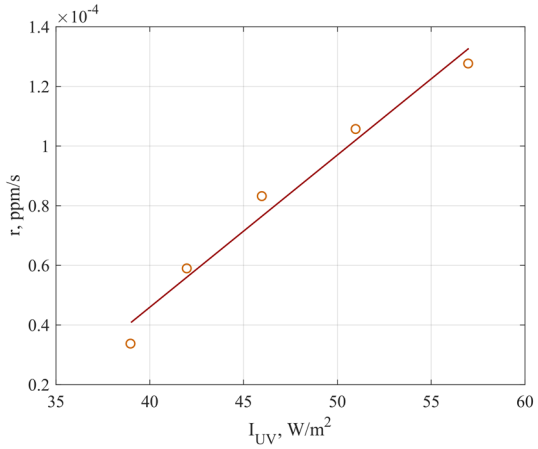

Figure 4-23 Linear dependence between reaction rate and surface incident radiation at constant C_2H_4 initial concentration. Plot generated by using data from Paper B.

However, the storage facility case studies showed an average humidity of approx. 80%, under which all fresh produce were stored. Thus, considering the humidity for intrinsic kinetic investigations was not regarded to be of paramount necessity. Figure 4-24 shows two degradation curves recorded under conditions of suspected catalyst deactivation obtained with two different catalyst plates.

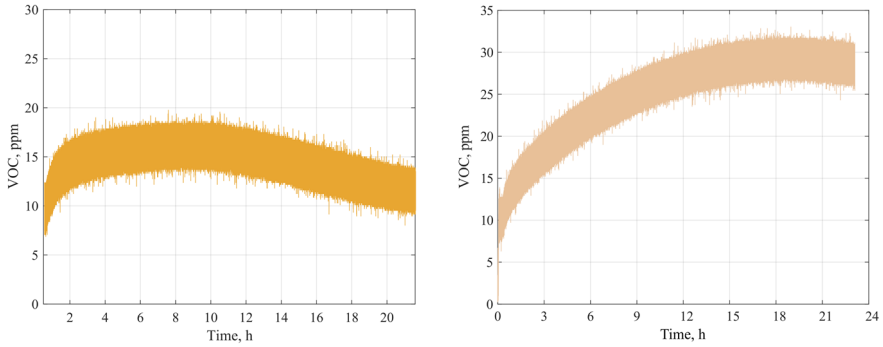

Figure 4-24 Degradation curve of C_2H_4 over TiO_2 catalyst suspected of deactivation.

The TiO_2 catalyst still appears to show oxidation potential. However, the degradation rate is significantly slower. In both aqueous and gas phase systems reactions intermediates and products tend to accumulate on the catalyst surface. In aqueous phase systems, water tends to remove the accumulated species from the surface (54). However, this is not the case for gas phase systems, where unremoved species decrease the activity of the catalyst, by poisoning the semiconductor surface and occupying active sites (55). This phenomenon has been described in literature, by

researchers that have experienced the deactivation of used TiO_2 catalyst, regardless of organic pollutant degraded (54–59). Interesting is the increase of VOC levels after the irradiation of the catalyst started. This increase has previously been mentioned as being a desorption phenomenon of VOC species from the surfaces of the enclosure. As these desorb into the gas phase, the activated catalyst oxidizes them. In the case of catalyst deactivation the released VOC species are not degraded fast enough as the desorption takes places, thus a build-up was recorded. As in depth investigations of the reaction in terms of intermediates and by-products were not conducted, the explanation given above is speculative. Thus, more research is needed to confirm or demount these assumptions.

4.3. CONCLUDING REMARKS

The kinetic study lead to the following main conclusions:

- The substrates used for TiO_2 coating had little to no influence on the morphological structure of the resulted catalyst, as both XRD and Raman spectroscopy procedures showed. The employed substrate materials affected the photocatalytic properties of the catalyst, however to a negligible extent. The thickness of the deposited film also played a role for the photocatalytic potential of the catalyst, where an increase in thickness translated into higher activity. It can be stated that the choice of catalyst substrate is ultimately a trade-off between deposition time, cost, mechanical stability and optical properties. Although optical properties have not been investigated, choosing a substrate material that can induce reflective properties to the photocatalyst can enhance the use of irradiation in a photoreactor.
- The photocatalytic oxidation of C_2H_4 over TiO_2 thin films can accurately be modelled by both the Langmuir-Hinshelwood rate model and by a first-order reaction rate. It was emphasized that the derived kinetic parameters are intrinsic and changes in reaction conditions dictate different kinetics. A shift in reaction order has been experienced when working with high C_2H_4 concentrations, in the order of a few thousand ppm.
- The intrinsic kinetic parameters depend exponentially on the initial concentration of C_2H_4, resulting in an enhancement of reaction rate as the concentration increases. Similarly, a better or more intense irradiation of the catalyst results in a more efficient degradation of pollutant. Studying the photocatalytic reaction under varying levels of C_2H_4 and irradiation resulted in comprehensive kinetic model that can be applied for predicting the degradation of C_2H_4 over TiO_2 under similar reaction conditions. The derived kinetic model can readily be employed for photoreactor CFD modelling as a tool for virtual prototyping.
- Linking the reaction rate to the intensity of the surface incident radiation was regarded as a step forward for the photocatalytic degradation of C_2H_4 over

TiO_2. Many of the models presented in literature are not directly applicable, as the oxidised VOC was different, or the reaction was studied under different conditions. Moreover, oftentimes photocatalytic studies do not link the rate to the intensity of the irradiation.

CHAPTER 5. PHOTOREACTOR DESIGN

The main goal of the FRESH project was the minimisation of food waste by enabling efficient monitoring and control of C_2H_4 levels. As a pathway towards reaching this goal a photoreactor that can safely and efficiently degrade C_2H_4 on TiO_2 via UV-A light was considered. The postharvest industry being diverse, the reactor had to be designed to accommodate a variety of end-users with different requirements. The process of developing the reactor started with establishing design criteria.

5.1. DESIGN CRITERIA

The efficient operation of the photoreactor was regarded to be dependent on the good operation of three different processes: mass transfer, photocatalytic reaction and radiation. Thus, design criteria have been established relative to these three processes.

The photochemical reaction is interconnected to the mass transfer, as the C_2H_4 molecules need to be present at the surface in order to be degraded. Increasing the mass transfer through turbulent mixing will consequently increase the probability of C_2H_4 molecules being exposed to the active TiO_2 surfaces.
Early in the design development, the influence of turbulence on conversion efficiency and residence time was acknowledged, as it is well known that turbulent mixing enhances chemical reactions. Therefore, it was considered to be of importance to establish if flow mixing would also enhance the surface reactions in the case of photocatalysis. Two simple, yet insightful CFD simulations of a continuous flow cylindrical reactor were made. At this stage, the geometry used for the simulations did not impose any design considerations for the future photoreactor. The simulation was purely used to gain insight into the influence of turbulence on the kinetics. Figure 5-1 shows the geometry used for this simulation. The following dimensions describe the geometry:

Table 5-1 Geometry dimensions for turbulent mixing simulations.

Reactor length	0.6
Reactor diameter	0.3
Tube diameter	0.05
Distance reactor center – tube center	0.08

It was considered that the five tubes placed along the length of the reactor are coated with TiO_2, meaning that the reaction took place at the surfaces enclosing these tubes. Moreover, it was assumed that the shell of the reactor was transparent, in order to allow the internal tubes to be irradiated.

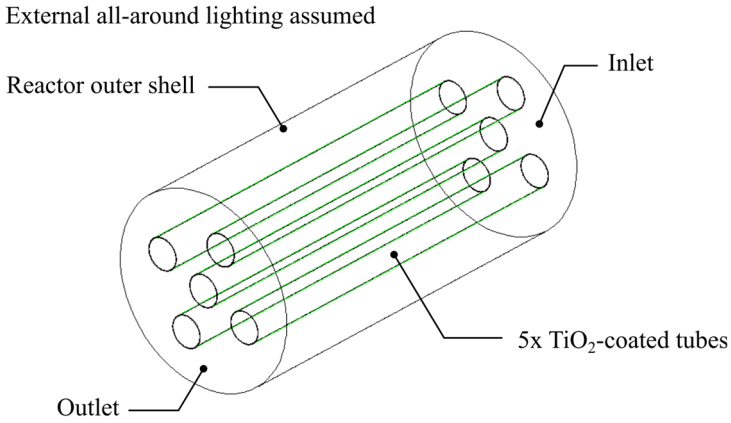

Figure 5-1 Geometry used for simulating turbulent mixing for observing its effect on conversion efficiency.

To quantify the influence of mixing on the conversion efficiency, two simulation cases were considered:

- Case 1: Axial flow, entering the domain normal to the inlet boundary
- Case 2: Swirling flow, entering the domain in a rotating motion.

For both cases the velocity of the flow entering the domain was u = 3.5 m/s, resulting in a Reynolds number (Re) of 6700, thus turbulent flow. The axial flow and the swirling flow were modelled by the standard k-ε and the realizable k-ε turbulence models, respectively. The realizable k-ε turbulence model gives improved results for swirling flows, compared to the standard model. The spatial discretization scheme used for both simulation cases was the second order upwind scheme.

Pathlines displayed in Figure 5-2 show that there is no flow disturbance, when an axial flow is simulated. It can be easily concluded, just by observing the pathlines that only the molecules in the proximity of the TiO_2 tubes can be degraded, while those further away, such as at the reactor's walls, will not be oxidised. Thus, it can be assumed that the swirling flow will enhance the conversion due to the swirling motion, which increases the probability for C_2H_4 – TiO_2 contact.

The transport of radiation was not modelled here, however the species transport and the oxidising reaction (1.1) were implemented. The C_2H_4 concentration of the gas entering the reactor domain was 5 ppm. As previously mentioned, the surface reaction was defined at the surfaces of the tubes. Because reaction kinetics at low concentrations were not studied when the simulation was ran, the zero-order kinetics (Kinetic study I, Section 4.2.2) were implemented to describe the conversion of species.

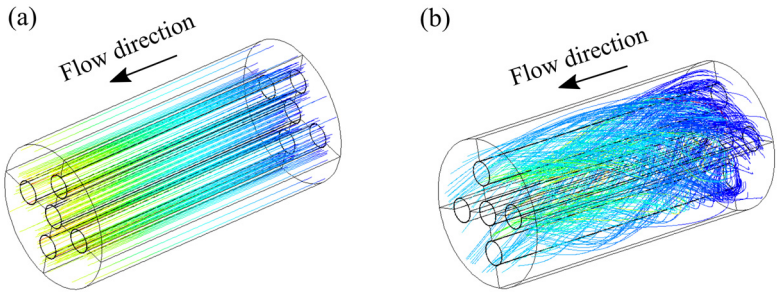

Figure 5-2 Flow pathlines. (a) Axial flow; (b) Swirling flow.

To observe and compare the degradation of C_2H_4 resulting from different flow characteristics, concentration data was exported from three different locations, along the reactor's length, between reactor wall and one of the coated tubes. These three locations, P1, P2, P3, from inlet to outlet, are shown in Figure 5-3.

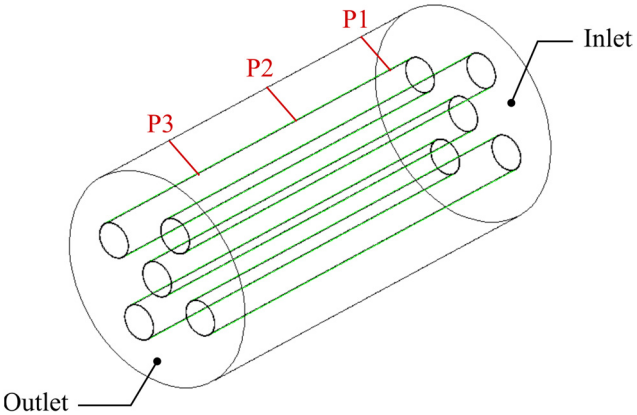

Figure 5-3 Display of the three locations used for data extraction, for C_2H_4 distribution visualisation.

The data extracted from these locations was plotted against the normalized distance between the reactor's wall and one of the TiO_2-coated tubes. The results are shown in Figure 5-4 for both flow simulations to ease the comparison. The normalized position 0 corresponds to the catalyst and the normalized position 1 denotes the wall. It becomes clear, that the mixing of the C_2H_4-contaminated flow is beneficial in terms of conversion efficiency. Imposing a disturbed motion to the fluid resulted in an 18% higher reduction.

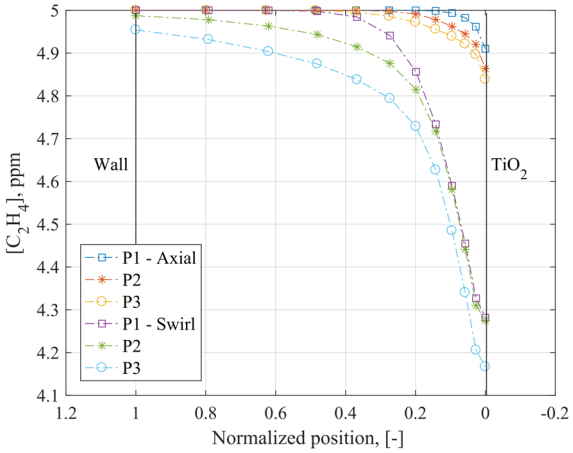

Figure 5-4 C_2H_4 concentration distribution between reactor wall and TiO_2-coated tube - axial vs. swirling flow.

Moreover, another factor that affected the conversion positively, alongside the high tortuosity of the fluid path, was the increased residence time. Increasing the residence time of the fluid particles in the reactor increased the likelihood of the C_2H_4 molecules to be directed towards and come into contact with the active catalyst, by the turbulent mixing. The average residence time of the fluid particles in the axial flow was below 1 s, whereas particles reached the outlet of the reactor in an average of 10 s when swirls were present. Of course, the residence time highly depends on the velocity of the fluid entering the reactor. However, the difference in residence time between the two flow types is significant and underlines the positive influence of mixing on the surface reaction.
This simple study on the effect of mixing on the photocatalytic surface reaction concludes in establishing the first design criteria for the development of the photocatalytic reactor: enhanced species – catalyst contact.

Radiation is also a key factor for the initialisation of the degradation. It has already been discussed that an increase in surface incident radiation enhances the conversion efficiency, by increasing the reaction rate. At the same time, it was mentioned that the increase in rate as a function of radiation is limited. In addition to the use of an UV-A light sources with high power, it is of equal importance to obtain a uniform distribution of the generated radiation, with minimised shadow zones. Therefore, optimizing the contact of photons to the photocatalyst was determined as the third design criteria.
Not related to the actual process itself, are the design aspects of ease of installation and scalability.
Figure 5-5 relates the photoreactor processes and the established criteria upon which the design of the photochemical reactor was based.

According to the CFD study conducted in Section 3.2.3, C_2H_4 molecules diffuse slowly from the source to the surrounding bulk atmosphere. This was mainly due to a poor flow entrainment inside the facility, as comfortable air conditions were imposed for the workers. This is a common case for storage facilities and transportation trucks. At this point, C_2H_4 not reaching the photoreactor was a concern. Several options were considered, among which having battery-driven small scale reactors that could be installed inside packaging or a system of several reactors that can be placed at the level of the packages. The idea behind this being to bring the reactor to the pollutant if vice versa is troublesome. However, it was decided, considering the requirements of potential end-users involved in the FRESH project (Salling Group, PKM, Alex Andersen), to focus on developing a single air-cleaning unit.

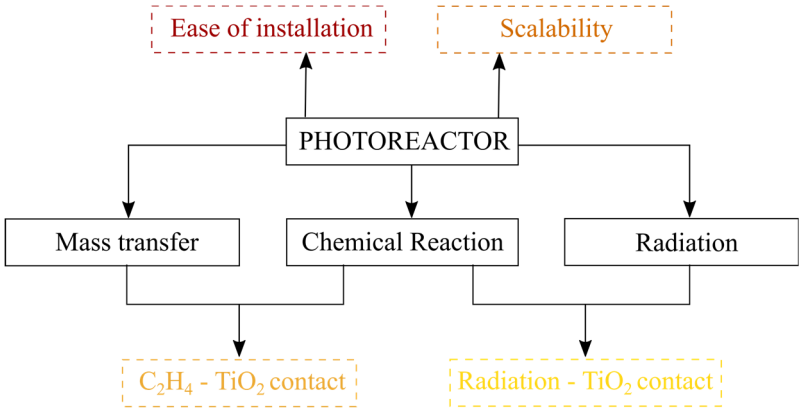

Figure 5-5 Processes describing the operation of the photoreactor and established design criteria (dashed contour).

Having one single unit reduces the price of such a system and the effort of installation. The focus was then shifted to the ventilation system, which is based on recirculation and not air exchange. Recirculating the contaminated air was considered an advantage, as the air could be cleaned as it passed through. Thus, two options have been considered. The heat exchanger used for cooling is manufactured for maximum air-surface contact. Thus, it easily satisfies the design criteria of increasing the contact between C_2H_4 molecules and TiO_2 catalyst, while at the same time making use of systems already present. However, the issues here were multiple:

- Coating of the tubes, plates or fins, depending on heat exchanger type.
- Illumination of the internal coated surfaces.
- Manufacturing the heat exchangers for this specific application. Thus, increased cost.

Further exploiting the option of using the ventilation system, it was decided to design the reactor as an integrating part of the ventilation system, in the same way a fan can be an integrating part of a duct system. This approach allows the free design of the

reactor to accommodate the criteria previously stated. Thus, the cleaning unit was based on standard galvanised stainless steel ventilation ducts, with the least possible number of custom parts. Using standard ventilation elements reduces the manufacturing process and its cost. Moreover, this reactor could be easily installed in all types of enclosures storing fresh produce and it can be scaled up or down, depending on requirements, as duct parts come in multiple dimensions. Hence, the criteria of ease of installation and scalability have been reached. To be noted is that the ventilation elements have a circular cross section, creating a cylindrical reactor.

The enhancement of reaction rate via increased mass transfer can be achieved through turbulent mixing and flow obstruction. Three different methods for increasing the contact between species and active surface have been designed and implemented. Firstly, to obtain a swirling motion of the gas entering the reactor, its inlet and outlet have been placed tangentially. The resulting outer shell of the reactor is depicted in Figure 5-6.

Figure 5-6 Top view of the reactor shell with tangential inlet and outlet.

Secondly, to increase the surface area of catalyst and the contact surface between species and active sites, baffles are placed radially on the inner shell wall. These baffles are coated with TiO_2 thin films. These are fitted on four threaded rods. Three rods are radially and equally distributed along the length of the reactor, while one is placed centrally along the length. In between the rods, distributed in the same manner, are three UV-A tubes.

The third method of increasing the species contact to the catalyst is flow obstruction. This was achieved by the design of TiO_2-coated perforated plates with triangular shape, installed on the same threaded rods. It is expected for the turbulence created with the tangential inlet to be dampened by the perforated plate. Thus, to maintain a certain flow disturbance across the length of the reactor, the baffles are placed at an angle relative to the axial direction.

In addition to enhanced species – catalyst contact, the presence of turbulence will increase the residence time of the species inside the reactor. This is an important parameter for increasing the conversion efficiency, as the probability of pollutant molecules being oxidised increases.

The internal design of the reactor, including the support-threaded rods, the UV-A tubes, baffles and perforated mesh elements, is presented in Figure 5-7. The number of baffles and perforated plates can vary, offering the reactor the property of modularity and scalability. As previously mentioned, it was of interest to use as few custom parts as possible, hence standardised perforated plates were used, the outer shell was a standard duct and the UV-A tubes can be easily purchased in the desired length and diameter. The baffles were specifically designed for this reactor out of aluminium. Drawings with dimensions of the elements depicted in Figure 5-7 are found in Appendix D.

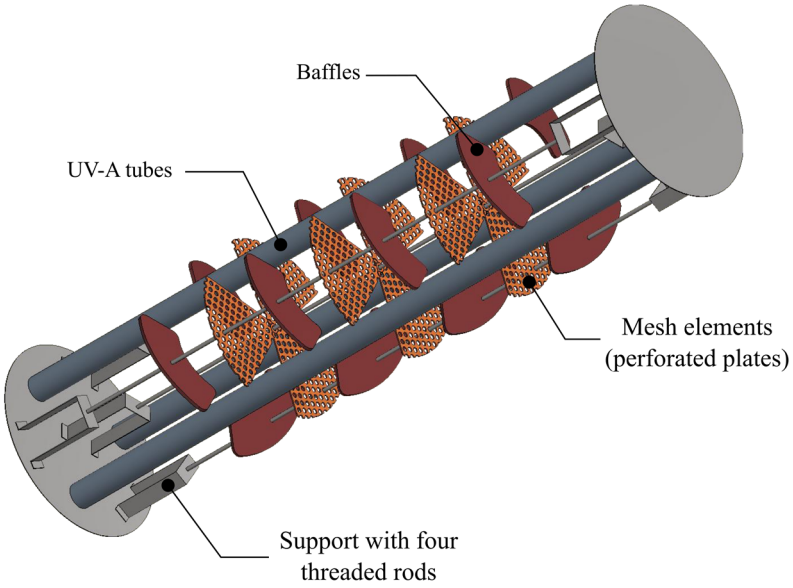

Figure 5-7 Internal elements of photoreactor. Number of mesh elements and baffles can vary. Number of UV-A tubes is fixed. Colours used for representation only.

To exemplify the placement of the baffles at an angle relative to the axial direction the top view in Figure 5-8 was generated.

The reason behind placing UV-A tubes along the whole length of the reactor was to ensure the irradiation of all the internal elements of the reactor, coated with TiO_2. This will results in few shadow spots, allowing the maximization of the contact between photons and TiO_2 catalyst deposited on the baffles, mesh elements and the internal walls of the reactor.

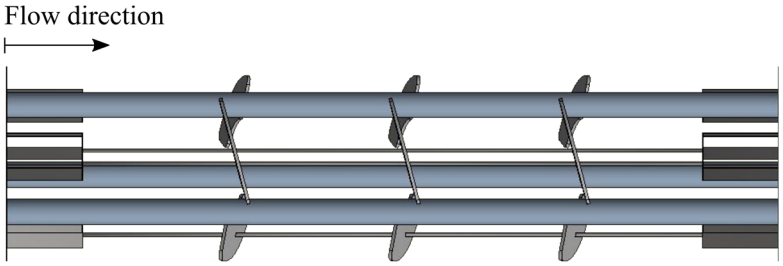

Figure 5-8 Photoreactor top view. Baffles placed at an angle relative to flow direction.

The design here described was manufactured into a prototype to be used for experimentation and model validation. The prototype is briefly presented in the following.

5.2. PHOTOREACTOR PROTOTYPE

As previously mentioned, a prototype of the photoreactor was manufactured in order to be used for experimental and validation work. Figure 5-9 shows the prototype as part of a loop system. The system can be divided in three parts:

- Photoreactor
- Closed loop
- Fan module.

The reactor unit was constructed from galvanized steel ventilation ducts with a diameter of D_r = 0.315 m. The total length of the reactor, from one end cap to the other is L_r = 1.67 m. Internally, the reactor unit has the design depicted in Figure 5-7 and Figure 5-10.

The inlet and outlet are standardised tangential saddles with 0.315 to 0.2 m reduction in diameter. These give the inlet and outlet a diameter of $D_{in} = D_{out}$ = 0.2 m. The support, on which the internal elements sit (Figure 5-7), has a length of $L_{support}$ = 1.2 m. The difference in length between reactor shell and support is dedicated to the AC ballasts and wiring of the UV-A tubes. It is of high importance to protect these from UV radiation.

The fan module houses an energy-saving axial fan from Ebmpapst, type W1G230-EB91-01, with a maximum volumetric flow rate of 1000 m^3/h. Detailed fan data can be found at (60). A standard regulator enables the control of the fan speed and thereby the air flow.

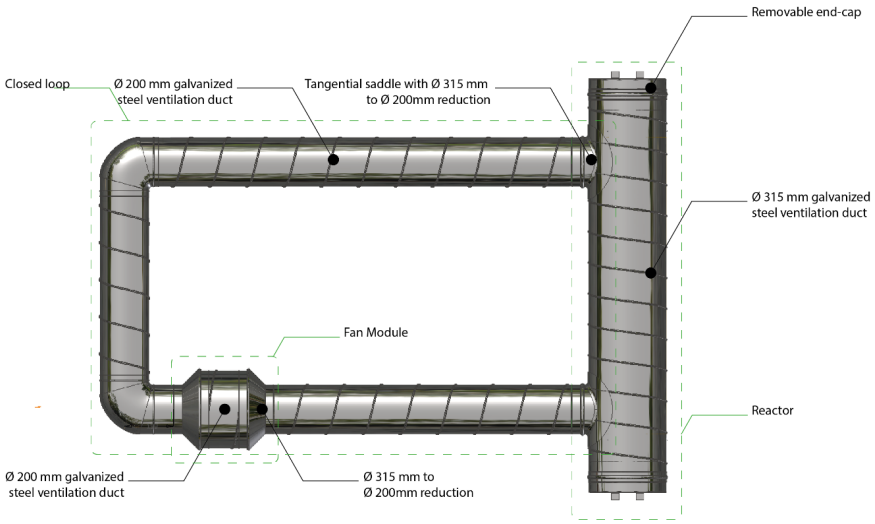

Figure 5-9 Drawing of the photoreactor prototype integrated in a closed loop system used for experimental work.

Figure 5-10 Internal elements of the photoreactor. Picture taken at DTI before installation for experiments.

The reactor unit connected to part of the closed loop, as defined in Figure 5-9, is shown in Figure 5-11, when in progress of being installed for experimental work.

The UV-A tubes are standard off-the-shelf products. The choice was based on factors that include length according to reactor size, intensity, price, and simplicity in the overall design. The chosen tubes are three Philips TL 60W/10-R SLV/25 UV-A lamps, from the Flexo Print range. The tubes have a length of $L_{UV\text{-}A\ tube} \approx 1.2$ m and diameter of $D_{UV\text{-}A\ tube} = 0.0405$ m. These generated UV-A light at 15.8 W. Technical data can be found at (61). Manufacturer-recommended AC ballasts power the tubes. The overall design configuration for the three tubes is:

- One double ballast, powering 2 UV-A tubes
- One single ballast, powering a single UV-A tube.

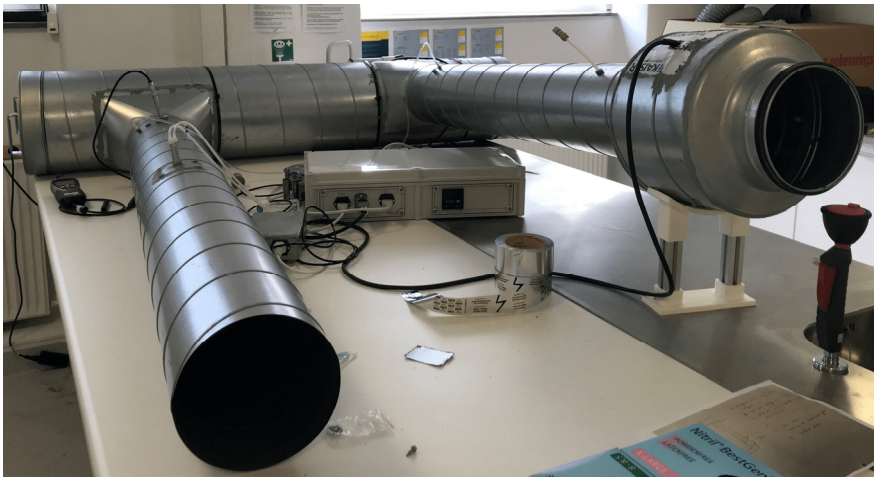

Figure 5-11 Partial experimental setup. Reactor and side ducts, fan module and power box.

Since the axial fan and the UV-A tubes are driven by 230 VAC, a control and power box was assembled to engage the reactor and provide the necessary power and control supply to the system.

It was previously mentioned that among the coated surfaces lie the internal walls of the reactor. The chosen coating technology imposes for the targeted surfaces to be fully exposed. Hence, in order to ensure coated internal walls and maximize the conversion efficiency, TiO_2 was deposited on thin Al foils with dimensions corresponding to the unfolded reactor cylinder. These were rolled and introduced inside the reactor, covering the internal walls of the photoreactor.

The prototype setup can be operated both as a closed loop system, as depicted in Figure 5-9, and as an open loop system by disconnecting the U-shaped duct.

To test the prototype and investigate its operation and behaviour, screening tests were performed. The screening tests were conducted at the Tribology Center, DTI by two Bachelor students from Aarhus University for their Bachelor thesis. The trials were conducted to identify the factors with most influence on the behaviour of the reactor – concentration, flow and UV-A radiation. For the initial experimental screening, the system was used in closed loop mode. C_2H_4 was supplied by adding approx. 50 mL 5000 ppm C_2H_4 via a syringe to the closed prototype. The addition was ceased when the concentration reached the desired value. The RH and CO_2 levels were kept at ambient levels. The gas stream was sampled by removing about 70 mL/min from the prototype for concentration monitoring via PTR-MS (Proton-transfer-reaction mass spectroscopy).

The experimental series were randomly set up using the Minitab statistics software, to avoid systematic errors. The experiments were designed according to two sets of 2x2 factorial design, with three centre points, resulting in 14 trials. One set corresponded to UV-A irradiation on, while one to UV-A irradiation off. The parameter space allows for an investigation of combined high and low levels of flow and concentration, as well as an intermediate value. Low, high and intermediate correspond to specific values of volumetric flow rate and C_2H_4 concentration as listed in Table 5-2. The flow-concentration combinations, with acronyms corresponding to values given in Table 5-2, are represented in Figure 5-12.

Table 5-2 Experimental conditions for screening tests.

	$\dot{q}$, [m^3/h]	$[C_2H_4]$, [ppm]
Low (L)	40	1
Intermediate (I)	355	5
High (H)	393	10

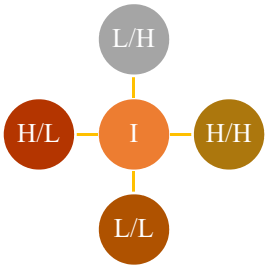

Figure 5-12 Flow -concentration combinations used for 2x2 factorial experiments.

The sampling of the contaminated gas causes a dilution of the gas stream, considering that the system operates in closed loop mode without continuous addition of C_2H_4. Thus, to ensure sufficient C_2H_4 conversion and at the same time avoiding significant dilution each experiment was run for only 2 hours.

The PTR-MS detected the concentration of C_2H_4, as well the development of a fragment defined as “M43”. This fragment was a trace of several larger organic compounds and hence an indication of the presence of contamination. The degradation curve of C_2H_4 and the development of M43 for the L/H combination is plotted in Figure 5-13. The low traces of M43 indicate that the gas stream is almost free from contaminants. The rate of degradation of the reactor, r_r, for this experiment was 0.0049 ppm/min.

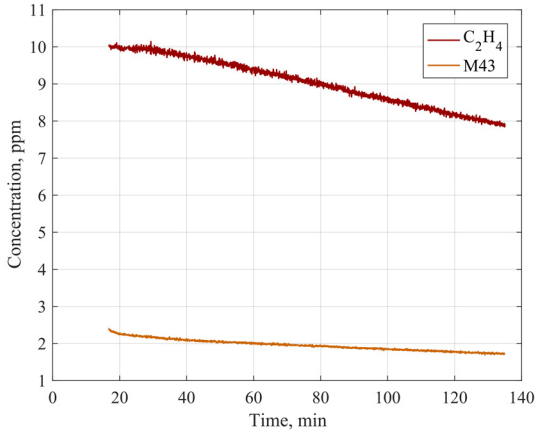

Figure 5-13 Degradation of C_2H_4 and evolution of fragment M43 for L/H experimental set.

The degradation curve can be easily fitted to a first order polynomial, which was not added to Figure 5-13, due to an overlap, which would make reading the data difficult. However, the Eq. (5.1) estimates well the concentration of C_2H_4 over time with an R^2 value of 0.99.

$$C = -0.019t + 10.482 \qquad (5.1)$$

Based on the findings it can be concluded that the degradation rate in this case can be readily modelled via first-order rate law. This is in agreement with the kinetic studies conducted in Section 4.2.2.

Table 5-3 Experimental conditions and results of the screening tests.

Definition	$\dot{q}$ m^3/h	$[C_2H_4]$ ppm	UV-A setting	r_r ppm/min
L/L	40	1	On	0.0049
			Off	0.0002
L/H	40	10	On	0.0190
			Off	0.0022
H/H	393	10	On	0.0210
			Off	0.0107
H/L	393	1	On	0.0038
			Off	0.0014
I	355	5	On	0.0107
			On	0.0140
			On	0.0123
			Off	0.0052
			Off	0.0060
			Off	0.0064

The degradation curves resulted from the rest of the experimental flow-concentration combinations given in Figure 5-12 are graphically represented in Appendix E. Table 5-3 gives the details of the rest of the experiments and the resulted degradation rate, r_r.

At intermediate point, three repetitions were conducted for both light and dark conditions. Mean values are listed in Table 5-4.

Table 5-4 Mean values of degradation rate at intermediate conditions.

Definition	$\dot{q}$ m^3/h	$[C_2H_4]$ ppm	UV-A setting	r_r ppm/min
I	355	5	On	0.0131
			Off	0.0059

Based on the results presented several conclusions can be drawn. Firstly, it can be observed that the degradation takes place even under dark conditions. The decrease in concentration while the UV irradiation is not present can be attributed to different processes:

- Molecules adsorb to reactor surfaces, causing a slow decrease in concentration.
- The catalyst is able to degrade under dark conditions.
- The system is not airtight.

It is assumed that by subtracting the degradation curves under dark conditions from those obtained under light conditions the adjusted degradation curves are obtained. The adjusted degradation rates, $r_{r,adj}$, are listed in Table 5-5 and graphically represented in Figure 5-14.

Table 5-5 Adjusted degradation rates.

Definition	$\dot{q}$ m^3/h	$[C_2H_4]$ ppm	$r_{r,adj}$ ppm/min
L/L	40	1	0.0047
L/H	40	10	0.0168
H/H	393	10	0.0103
H/L	393	1	0.0024
I	355	5	0.0072

Secondly, it can be noted that the increase in volumetric flow rate does not affect the degradation significantly, considering the notable difference in flow rate between the two settings. This becomes obvious when comparing the degradation rates for L/H and H/H. Although, increasing the velocity increases the Reynolds number of the flow, and in turn, the turbulence mixing, the residence time decreases. This causes the contaminated flow to spend less time in the reactor unit, which consequently decreases the probability of the C_2H_4 molecules to be exposed to active sites.

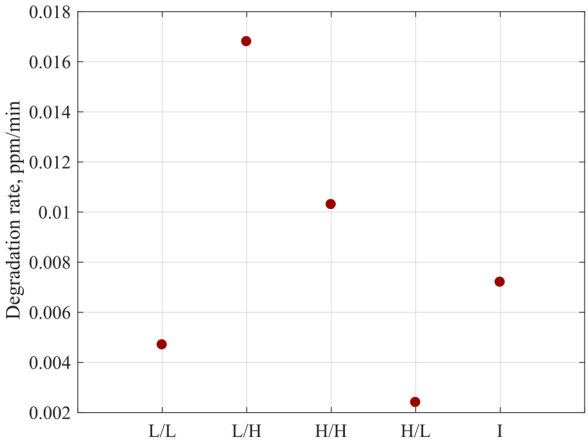

Figure 5-14 Plot of adjusted degradation rates, $r_{r,adj}$.

Hence, a trade-off between volumetric flow rate and residence time needs to be considered. This might not be possible always, as end-users already have a ventilation unit that runs at specific flow rates. However, guidelines can be offered, upon which the end-users can decide if changes are possible and beneficial.

Lastly, as previously observed, an increase in concentration translates into a faster degradation rate, due to the increased number of molecules available to be degraded at the catalyst surface. Again, if looking at Figure 5-14 for $r_{r,adj}$ corresponding to L/L and L/H this effect becomes clear.

More screening tests have been performed to observe if the photoreactor behaves as expected. The effect of and RH was investigated.
The RH of the gas stream is increased from ambient conditions and maintained at approx. 85%, slightly higher than RH measured in storage facilities. The initial C_2H_4 concentration was 10 ppm and the $\dot{q} = 40$ m^3/h. The degradation curve was plotted in Figure 5-15 and the adjusted rate of C_2H_4 oxidation was 0.0022 ppm/min. For the same concentration and flow rate conditions, r_r is 8 times slower in the case of increased RH. This is expected behaviour, as it is well known that H_2O molecules compete with C_2H_4 molecules for free active sites on TiO_2 catalyst surface. The experiments with the prototype unit showed a continuous decrease in degradation capability over time, due to a decreased activity of the catalyst surfaces. This led to the opening of the system to get access to the reactor's internal elements. Investigating the TiO_2 coatings revealed that a deactivation of the surfaces took place due to oxidizing surface phenomena. Although difficult to capture in a picture, Figure 5-16 depicts the coating after elements were removed from the reactor shell, showing rust-like spots and shadows.

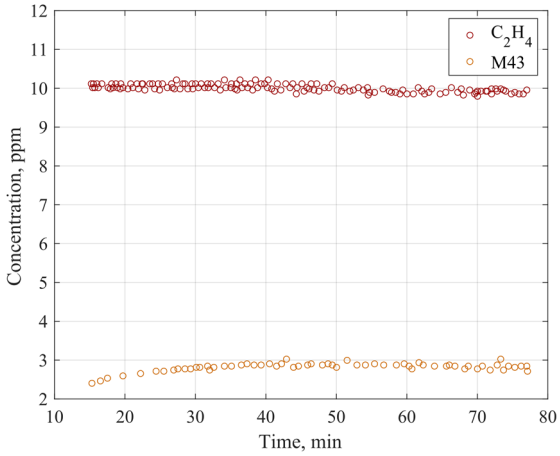

Figure 5-15 Concentration evolution for C_2H_4 and fragment M43 for RH screening test at RH = 85%, $[C_2H_4]$ = 10 ppm and q = 40 m^3/h.

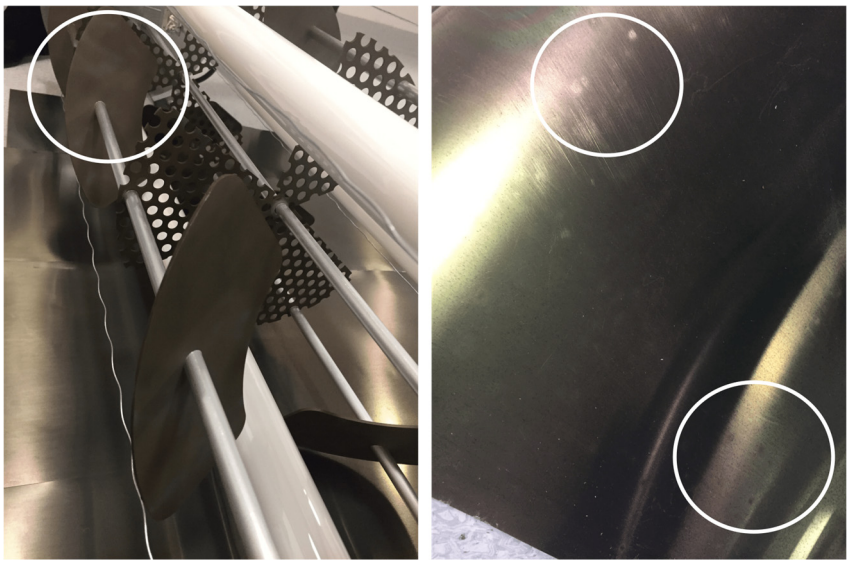

Figure 5-16 TiO_2-coated surfaces showing signs of deactivation through oxidation patches (left) and spots (right).

Although the reactor's behaviour has been in agreement with expectations, based on the previously conducted kinetic studies in a batch reactor, the experimental work on the prototype was ceased. This decision was made due to the deactivation phenomena and due to the financial and time limitations to manufacture and coat new elements. Consequently, the prototype unit was no longer an option for calibrating and validating the CFD model intended to be developed. Despite this major setback, the

prototype was modelled through CFD with the academic purpose of investigating how the reaction is affected by design, operating conditions and ultimately to derive optimisation options. The models set up and the results are presented in the next section.

5.3. CFD SIMULATIONS

The CFD simulations were carried out as a Design of Experiments (DOE), by conducting parametric studies on different design variations. All CFD simulations, although different in geometry and/or initial conditions, were numerically approached in a similar manner. This was possible thanks to the use of the same numerical models to describe the multiphysics behind the photocatalytic process: flow, radiative transfer and species transport. ANSYS Fluent, customised with User-Defined Functions (UDFs), was used for simulating the photocatalytic reactor.

5.3.1. SIMULATION CASES

To reduce computational efforts and time the design of the reactor used of simulations did not include the mesh elements, placed radially along the length. Thus, the internal elements modelled are the UV-A tubes and the baffles.

The simulation cases investigated, as part of the DOE, are defined based on design considerations and flow conditions. Table 5-6 gives an overview.

Table 5-6 Definition of CFD simulation cases in terms of geometry and flow conditions.

Simulation case	Baffles stages	Baffle angle, °	$[C_2H_4]_0$, ppm	Inlet velocity	Incident radiation, W/m^2	Acronym
1	4	20	10	0.36 1 2.3 3	88	S1-V1 S1-V2 S1-V3 S1-V4
2	4	15 20 25 30 40	10	0.36	88	S2-A1 S2-A2 S2-A3 S2-A4 S2-A5
3	4	20	10	0.36	88	S3-M

Each simulation case is identifiable by the acronym, which defines the simulation case number (e.g. S1) and the variation in flow condition or design: V – velocity, B – baffle stages number, A – baffles inclination angle, and M – static mixer geometry. The simulation case S3-M was generated on a different geometry than that of the

prototype. In order to obtain better mixing and C_2H_4-TiO_2 contact the baffles were placed so that the reactor resembles a static mixer. Figure 5-17 and Figure 5-18 show the two geometries used.

The simulations were first made on the original geometry, S1, S2 and S3, comparing trends in C_2H_4 concentration (C), residence time (τ) and turbulent kinetic energy (k), under steady state, as flow and geometry configurations are varied. It is important to emphasize that the results presented here are trends of investigated parameters. Although a meshing approach and residual behaviour were taken into account to ensure reliable results, the high accuracy of results was not targeted due to the lack of experimental data for validation, as well as time limitations.

The CFD simulations were run on an Intel(R) Xeon (R) CPU E5-2687W v3 processor with 20 cores. Multiple cores allowed the simulations to be run in parallel, speeding the computations significantly. For each simulation 18 cores were used. The DOM was accelerated by an NVIDIA Quadro P5000 graphics processing unit (GPU) with 2560 CUDA cores and a GPU Memory of 16 GB DDDR5. Thus, computational efforts on the 18 used cores was minimized by employing the GPU.

General considerations will be made in the following, that are valid for all simulations conducted, listed in Table 5-6. Also, the governing equations of the models used will be presented.

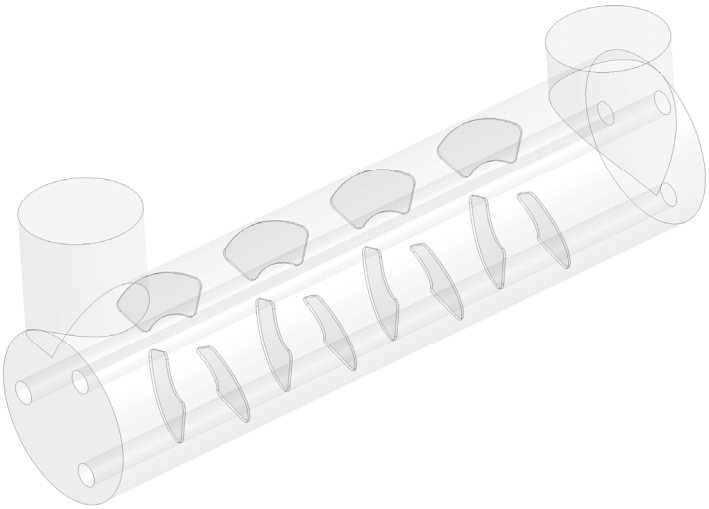

Figure 5-17 Prototype geometry used for CFD simulations. Tangential inlet - outlet and four stages of baffles placed at a 20° angle relative to axial direction. Number of stages and angle vary.

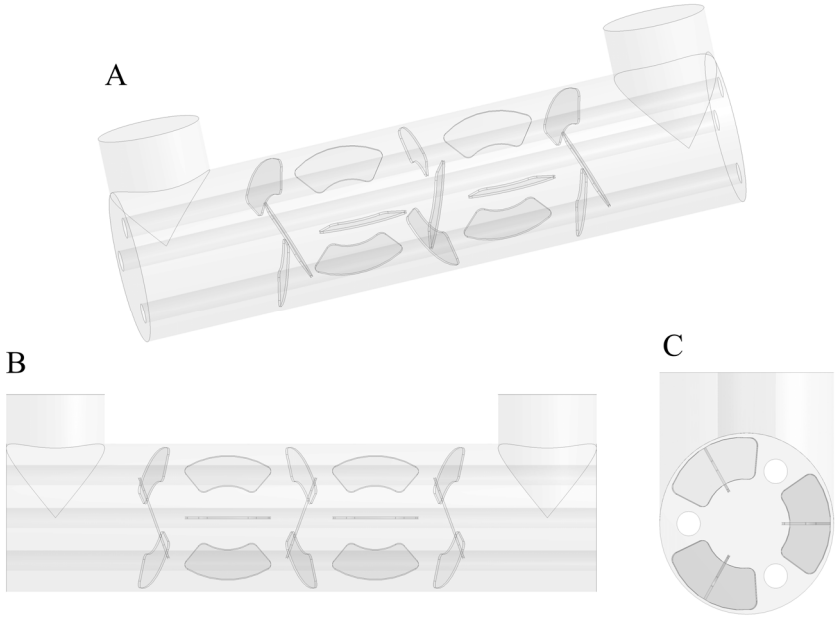

Figure 5-18 Geometry modified to achieve a resemblance to a static mixer, to enhance mixing and C_2H_4 - TiO_2 contact. Five baffles stages, out of which three have a 20º angle relative to axial direction. A – isometric view, B – side view, C – front view.

5.3.2. GOVERNING EQUATIONS AND CONSIDERATIONS

Considering the small diameter of the inlet of 0.2 m, and the velocity range simulated, the flow is characterised by Reynolds numbers ranging from 4600 to 40470. Thus, the simulations in this study were based on turbulent flow.
The governing equations were numerically solved by a segregated implicit steady state solution algorithm. Second-order upwind discretization scheme was employed. The convergence criterion for continuity, momentum and turbulence parameters was selected to be 10^{-4} and for the species concentration and radiation model (Discrete Ordinate Model, DOM) 10^{-6}. No under-relaxation for stabilizing the calculations was necessary.

Turbulent flows are characterized by fluctuating velocity fields. The fluctuations affect the transported quantities, such as momentum, energy and species concentrations, causing these to fluctuate as well. The fluctuations are generally too computationally expensive to simulate directly, as oftentimes these are of small scales but high frequency. Instead, the instantaneous governing equations can be time-

averaged, Reynolds-averaged, or manipulated to remove the resolution of the small scales, resulting in a modified set of equations that are less computationally heavy. (62) With modifications come additional unknown variables, which can be solved by employing turbulence models. The turbulence model chosen for these simulations to determine the unknown variables by means of known quantities is the shear-stress transport (SST) *k-ω* model. Here *k* stands for turbulent kinetic energy and *ω* for turbulent specific dissipation. The *k-ω* model is one of the several two-equation models, defined as being complete models, due to their ability of solving the turbulent viscosity and length scales independently. For engineering applications, the models including two or more transport equations are the most successful because two quantities are needed to describe the length and velocity scales of turbulent flows (63). In the case of the *k-ω* model, the length-determining quantity is the specific turbulent dissipation, *ω*, defined as the inverse of the time scale on which dissipation occurs. Relative to the most commonly used two-equation model, *k-ε* model, the *k-ω* model has the advantage of performing well in regions of low Re, where both *k* and *ε* approach zero. This can become troublesome, as both parameters need to approach zero at the correct rate because the dissipation term is defined in terms of both *k* and ε^2. Moreover, the *k-ω* model can reliably predict the law of the wall when the model is applied in the viscous sub-layer. Hence, there is no need of employing near-wall treatment. However, because no wall functions are used in combination with the *k-ω* model, it is necessary to consider placing the first grid point at $y^+ < 5$. It has been already mentioned that the SST version of the *k-ω* model has been employed for all simulations. The SST model differs from the standard version as follows (62):

- Ability of interchanging between the *k-ω* model in the inner region of the boundary layer and a high-Re-number *k-ε* model in the free stream. Thus, the SST version takes advantage of the qualities of both turbulence models.
- Formulation of the turbulent viscosity is modified, in order to account for the transport effects of the turbulent shear stress, hence its name.

The governing equations for the SST *k-ω* model are presented below (63). The continuity and Reynolds-averaged Navier-Stokes (RANS) equations for incompressible flow can be written as:

$$\frac{\partial \boldsymbol{U}_i}{\partial \boldsymbol{x}_i} = 0 \qquad (5.2)$$

$$\frac{\partial \langle \boldsymbol{U}_i \rangle}{\partial t} + \langle \boldsymbol{U}_j \rangle \frac{\partial \langle \boldsymbol{U}_i \rangle}{\partial \boldsymbol{x}_j} = -\frac{1}{\rho}\frac{\partial}{\partial \boldsymbol{x}_j}\left\{ \langle P \rangle \delta_{ij} + \mu \left(\frac{\partial \langle \boldsymbol{U}_i \rangle}{\partial \boldsymbol{x}_j} + \frac{\partial \langle \boldsymbol{U}_j \rangle}{\partial \boldsymbol{x}_i} \right) - \rho \langle \boldsymbol{u_i u_j} \rangle \right\} \qquad (5.3)$$

where $\boldsymbol{U}$ – Velocity vector
$\boldsymbol{x}$ – direction vector
ρ – density, [kg/m^3]
P – pressure, [Pa]
δ_{ij} – Kronecker delta
μ – dynamic viscosity, [kg/m s]

$\boldsymbol{u}$ – velocity fluctuation vector
i, j – tensor notation

The Kronecker delta is defined as

$$\delta_{ij} = \begin{cases} 1, i = j \\ 0, i \neq j \end{cases} \quad (5.4)$$

The brackets ⟨ ⟩ denote averaged quantities. The term $-\rho\langle \boldsymbol{u}_i \boldsymbol{u}_j \rangle$ defines the Reynolds stresses and it introduces a coupling between the mean and fluctuating parts of the velocity field. In order to close Eq. (5.3) it is necessary to model the Reynolds stress, which is the purpose of RANS turbulence modelling. For detailed tensor notation please refer to (63).

The modelled transport equations for the turbulent kinetic energy, *k*, and the turbulent dissipation rate, *ω*, are:

$$\frac{\partial k}{\partial t} + \langle \boldsymbol{U}_j \rangle \frac{\partial k}{\partial \boldsymbol{x}_j} = \mu_T \left[\left(\frac{\partial \langle \boldsymbol{U}_i \rangle}{\partial \boldsymbol{x}_j} + \frac{\partial \langle \boldsymbol{U}_j \rangle}{\partial \boldsymbol{x}_i} \right) \frac{\partial \langle \boldsymbol{U}_i \rangle}{\partial \boldsymbol{x}_j} \right] - \beta k \omega + \frac{\partial}{\partial \boldsymbol{x}_j} \left[\left(\mu + \frac{\mu_T}{Pr_k} \right) \frac{\partial k}{\partial \boldsymbol{x}_j} \right] \quad (5.5)$$

$$\frac{\partial \omega}{\partial t} + \langle \boldsymbol{U}_j \rangle \frac{\partial \omega}{\partial \boldsymbol{x}_j} = \alpha \frac{\omega}{k} \mu_T \left[\left(\frac{\partial \langle \boldsymbol{U}_i \rangle}{\partial \boldsymbol{x}_j} + \frac{\partial \langle \boldsymbol{U}_j \rangle}{\partial \boldsymbol{x}_i} \right) \frac{\partial \langle \boldsymbol{U}_i \rangle}{\partial \boldsymbol{x}_j} \right] - \beta^* \omega^2 + \frac{\partial}{\partial \boldsymbol{x}_j} \left[\left(\mu + \frac{\mu_T}{Pr_\omega} \right) \frac{\partial \omega}{\partial \boldsymbol{x}_j} \right] + \mathcal{D}_\omega \quad (5.6)$$

where μ_T – Turbulent viscosity, [kg/m s]
Pr_k, Pr_ω – Turbulent Prandtl number for k and ω, respectively, [-]
α, β – Model constants, [-]
$\mathcal{D}_\omega$ – Cross-diffusion term

The turbulent (eddy) viscosity is determined by

$$\mu_T = \frac{k}{\omega} \quad (5.7)$$

The SST *k-ω* model, as previously mentioned, is based on both the standard *k-ω* model and the standard *k-ε* model. To blend these two models together, the transport equations of the standard *k-ε* model have been transformed into equations based on *k* and ω, which introduces a cross-diffusion term, $\mathcal{D}_\omega$ (62). For further details on the model constant and the calculation of the cross-diffusion term please refer to the Fluent Theory Guide (62).
The SST *k-ω* model approximates the Re stresses by using the Boussinesq approximation (62), which is based on the assumption that the components of the Re

stress tensor, $\boldsymbol{\tau}_{ij}$, are proportional to the mean velocity gradients. The Boussinesq approximation proposes that the transport of momentum by turbulence is of diffusive nature and that the Re stresses can be modelled by means of the turbulent eddy viscosity, as given in Eq. (5.8) (63).

$$\boldsymbol{\tau}_{ij} = -\rho\langle \boldsymbol{u_i u_j} \rangle = \mu_T \left(\frac{\partial \langle \boldsymbol{U}_i \rangle}{\partial \boldsymbol{x}_j} + \frac{\partial \langle \boldsymbol{U}_j \rangle}{\partial \boldsymbol{x}_i} \right) - \frac{2}{3} k \delta_{ij} \qquad (5.8)$$

The species present in the modelled flow were introduced as an ethylene-air mixture. These were C_2H_4, CO_2, O_2, H_2O and N_2. The mixing and transport of chemical species was modelled by solving the conservation equations describing convection, diffusion, and reaction sources for each component species, given by Eq. (5.9).

$$\frac{\partial y_n}{\partial t} + \boldsymbol{U}_j \frac{\partial y_n}{\partial \boldsymbol{x}_j} = \frac{\partial}{\partial \boldsymbol{x}_j} \left(\mathcal{D}_n \frac{\partial y_n}{\partial \boldsymbol{x}_j} \right) + r(y, T) + S_n \qquad (5.9)$$

where y_n – mass fraction of species n, [-]
r – reaction rate, [kmol/m^3 s]
S_n – source term for species n

A wall surface reaction was enabled to account for the photodegradation of ethylene. The photocatalytic reaction was modelled as a wall surface reaction through the laminar finite-rate model. Under the laminar finite-rate model the effect of turbulent fluctuations are ignored and the reaction rates are determined by Arrhenius kinetic expressions, unless these are overwritten by kinetics introduced through User-Defined Functions (UDFs), as it has been done for the simulations discussed here. As the species present in the flow do not need to interact with each other to initiate the reaction, but need to be present at the TiO_2 surface, it was chosen to use the laminar finite-rate model and neglect the effect of turbulence on the reaction kinetics.

The distribution of surface incident radiation was predicted by the Discrete Ordinate Model. DOM solves the radiative transfer equation (RTE) over a finite number of discrete solid angles, each associated with a vector direction $\vec{\mathbf{s}}$ in the global Cartesian coordinate system (x, y, z). Ray tracing cannot be performed with DOM. Instead, the model transforms the RTE into the number of transport equations corresponding to the number of solid angles. Fluent uses the same method of solving the RTE as for solving the momentum and energy equations. The DOM considers the RTE in the direction $\vec{\mathbf{s}}$ as a field equation (62). Thus, the RTE is written as follows

$$\nabla \cdot (I(\vec{\boldsymbol{p}}, \vec{\boldsymbol{s}})\vec{\boldsymbol{s}}) + (a + \sigma_s) I(\vec{\boldsymbol{p}}, \vec{\boldsymbol{s}}) = an^2 \frac{\sigma T^4}{\pi} + \frac{\sigma_s}{4\pi} \int_0^{4\pi} I(\vec{\boldsymbol{p}}, \vec{\boldsymbol{s}'}) \Phi(\vec{\boldsymbol{s}} \cdot \vec{\boldsymbol{s}'}) d\Omega' \qquad (5.10)$$

where $\vec{p}$ – position vector
$\vec{s}$ – direction vector
$\vec{s'}$ – scattering direction vector
s – path length, [m]
a – absorption coefficient, [-]
n – refractive index, [-]
σ_s – scattering coefficient, [-]
σ – Stefan-Boltzmann constant, σ = 5.672e-08 W/m^2K^4
I – radiation intensity, [W/m^2]
T – local temperature, [K]
Φ – phase function
Ω – solid angle, [rad]

For this application, scattering was neglected, and the temperature was globally set to a constant value of 1 K to avoid solving the thermal emission term. Fluent offers the possibility of modelling non-grey radiation using up to 10 grey bands to account for spectral dependencies. Although the prototype's UV-A tubes emit radiation at a range of wavelength between 340 and 440 nm (61), in this study a single-band model was used, representing only the peak wavelength of 365 nm.

5.3.3. MESHING APPROACH

The meshing approach adopted for discretizing the computational domain was straightforward, with a few global characteristics/settings, defined for all simulation cases, regardless of Re.

The generated mesh was an unstructured mesh composed of a multitude of element types: tri, tetra, quad, hexa, wedge. This mix of elements stems from the generation of inflation layers at the reactor's shell, baffles and UV-A tubes. The reason behind using inflation layers is twofold. On one hand, as it is generally the case, inflation layers are generated to accurately resolve the boundary layer in wall-bounded flows and to capture the near wall physics. This was critical for the current application as the surface reaction defined at the boundaries generates and consumes species, which interact with the flow in the low-Re boundary layer region and are transported and mixed by the turbulent flow in the free stream. On the other hand, the inflation layer facilitated the manipulation of the mesh to obtain the desired y^+ value, dictated by the SST k-ω turbulent model employed. It has already been mentioned in section 5.3.2, that the SST k-ω model requires a $y^+ < 5$, due to the absence of wall functions. Thus, a $y^+ = 1$ has been considered for the meshes of all simulation cases. All used inflation layers had 6 stages with a growth ratio of 1.4.

The maximum element size and maximum face size were adjusted in order to obtain a smooth transition from the inflation layers to the unstructured mesh. In addition, the

aforementioned parameters were decreased with each simulation case. This increased the size of the mesh and the computational efforts. However, this was a trade-off as a finer mesh gave better convergence for the simulation cases with increased inlet velocity and helped reach convergence criteria in just a few hundred iterations with no need of lowering under-relaxation factors for stability. Moreover, decreasing the element size was also beneficial in terms of element quality and skewness.

Table 5-7 lists the size of the used meshes and their corresponding element quality for each simulation case.

Table 5-7 Statistics of generated meshes for the simulation cases investigated.

Simulation case	No. of elements, x 10^{-6}	Average element quality Standard deviation, χ
S1-V1	22	0.8, χ = 0.18
S1-V2	24	0.72, χ = 0.22
S1-V3	38	0.746, χ = 0.235
S1-V4	40.4	0.732, χ =0.25
S2-A1	30.2	0.82, χ = 0.124
S2-A3	30.7	0.82, χ = 0.124
S2-A4	30.67	0.82, χ = 0.12
S2-A5	30.65	0.823, χ = 0.123
S3-M	35.8	0.817, χ = 0.136

5.3.4. MODEL SETTINGS AND BOUNDARY CONDITIONS

Velocity-inlet and pressure-outlet were specified as the inlet and outlet boundary conditions, respectively. The inlet velocity was specified according to the simulation case targeted (Table 5-6), with the direction normal to the boundary, thus in the –y direction. As previously mentioned, the temperature was fixed in the fluid domain at constant value of 1 K. Hence, the temperature of the entering fluid was also set at 1 K. To define the flow in terms of turbulent characteristics, the turbulent intensity and the turbulent length scale were specified, calculated according to the approximations given in Eqs. (5.11) and (5.12), respectively (63).

$$Int = 0.16Re^{-1/8} \quad (5.11)$$

$$l = 0.07D_h \quad (5.12)$$

where D_h is the hydraulic diameter, [m].
The incoming flow was composed out of an ethylene-air mixture with the species concentrations listed in Table 5-8, applied to all simulation cases, given as mass fractions. The CO_2 concentration was defined based on the measured levels inside the storage facility at Aarstiderne and the H_2O concentration corresponds to RH = 80%, calculated by means of a psychrometric chart. The O_2 concentration was set according

to the average concentration in atmospheric air. The N_2 concentration was calculated by subtracting the concentration of the other species from the total of 1.

Table 5-8 Species mass fraction at inlet.

Species	Mass fraction, [-]
C_2H_4	1e-05
O_2	0.2
CO_2	1.6e-03
H_2O	3.75e-03
N_2	0.7946

Due to the impossibility of investigating the prototype experimentally, the kinetics of the reaction under the prototype settings could not be derived. As already mentioned, flow conditions and reactor design affect the kinetics of the reaction. It is expected for the continuous flow reactor, where mixing and flow entrainment is present, to dictate other reaction kinetics than those already derived in the batch reactor. Thus, it was considered that using the batch reactor kinetics was erroneous and not suited for the system investigated here. Because chemistry is of paramount importance, it was decided to implement one of the reaction rates determined experimentally, before catalyst deterioration was observed.

The photocatalytic reaction was defined as a surface reaction at the walls corresponding to the baffles and the reactor's shell. The L/H flow-concentration setting was considered with C_0 = 10 ppm and a degradation rate of $r_{r,adj}$ = 0.0168 ppm/min on a volume basis. This allowed the investigation of kinetics under different flow rates and geometry settings in the prototype, with the possibility of making concluding remarks towards the design. The reaction rate was modelled by fitting the Langmuir-Hinshelwood rate law to the corresponding experimental data, presented in Figure 5-13. As it can be observed in Table 5-6 the concentration of C_2H_4 across simulation cases was kept constant at 10 ppm. Thus, a dependence of reaction rate to initial concentration of contaminant was not implemented.

Unfortunately, it was not possible to observe the effects of radiation intensity on the reaction rate by applying the prototype, due to catalyst degradation. Therefore, another approach was needed, as this dependence was considered be one of the key elements influencing the overall efficiency of the reactor, as previously explained in section 4.2.2. Although deriving the relationship between kinetics and radiation employing the batch reactor was considered fundamental and successful, its applicability to the prototype was questionable. The main reason behind this being the different reaction conditions, despite using TiO_2 thin films coated through the same process. Neglecting the effect of radiation on the overall efficiency of the prototype was not desired, as it was still considered a key phenomenon, which can help understand the design.
It has been often times discussed in literature that the dependence of VOC degradation

rate to surface incident radiation follows a power law, with the exponent, α, taking values between 0 and 1 (64–69), in continuous flow reactors. The LH rate model becomes:

$$r_{r,CFD} = I^{\gamma} \frac{k_r K_{abs} C}{1 + K_{abs} C} \qquad (5.13)$$

Wang et. al (65) have adopted the simple mathematical form of power law, given in Eq. (5.14). The power law states that at sufficiently low intensities, the modelled reaction rate is linearly proportional to the irradiation intensity, and shifts to a half-order above 10 W/m^2. This decrease in order is due to the limited activity of the photocatalyst, which can be saturated by both VOC concentration and irradiance.

$$\gamma = \begin{cases} 1.0 \ (0 < I_{UV} \leq 10 \ W/m^2) \\ 0.5 \ (10 \ W/m^2 < I_{UV}) \end{cases} \qquad (5.14)$$

Fitting the LH rate model to the data in Figure 5-13 resulted in the determination of the two kinetic parameters: k_r = 0.3513 ppm/s and K_{abs} = 0.005 ppm^{-1}. Because the kinetic data was determined based on a prototype with additional TiO_2 surface area given by the presence of the coated perforated plates, the reaction rate was adjusted to the model's geometry with no such elements. Thus, the implemented reaction rate is given by:

$$r_{r,CFD} = I^{\gamma} \frac{k_r K_{abs} C}{1 + K_{abs} C} \frac{A_{cell}}{A_{perf.plate}} \frac{10^{-6} \rho_n}{M_n} \frac{V_r}{A_{cell}} \qquad (5.15)$$

where A_{cell} – area of a computational domain grid cell, [m^2]
V_r – reactor volume, [m^3]
$A_{perf.plate}$ – total area of perforated plates (as seen in Figure 5-7), [m^2]
ρ_n – density of species n, [kg/m^3]
M_n – molar weight of species n, [kg/kmol]

The third element on the right hand side of Eq. (5.15) allows the conversion from ppm to kmol/m^{3}s. The reaction was defined in the software as a surface reaction with units of kmol/m^{2}s. Hence, it was necessary to adjust the units accordingly. This was achieved through the last element on the right hand side of Eq. (5.15).

Figure 5-19 shows the definition of the polar and azimuthal angles, θ and ϕ, respectively, used to define the number of solid angles, N_θ *and* N_ϕ in the DOM. In three-dimensional space each octant of the angular space 4π at any spatial location is discretized into a total of 8 x N_θ *x* N_ϕ solid angles (62). A discretization resulting in too few discrete ordinates can cause the so-called ray effect, which can be remediated by increasing the number of modelled solid angles, thus obtaining a uniformly

distributed radiation field. For this particular application, for all simulations cases, a discretization of 5 x 5 was chosen. No ray effect was observed.

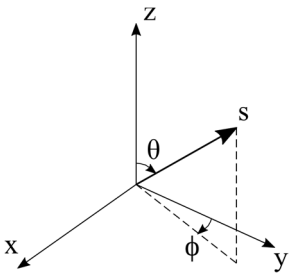

Figure 5-19 Angular coordinate system used for solid angle discretization in DOM. Reproduced from (62).

As an unstructured mesh was used to discretize the computational domain, control volume faces do not always align with the global angular discretization, as exemplified in Figure 5-20. Consequently, control angles straddle the control volume faces, partially incoming and outgoing to the face. Overhanging angles can also be a result of reflection and refraction, according to the Fluent Theory Guide (62).

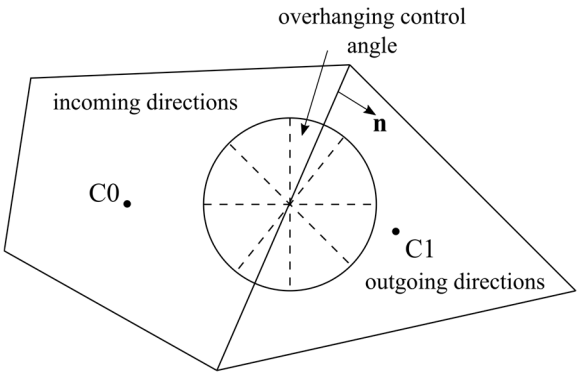

Figure 5-20 2D example of global and angular discretization not being aligned, resulting in an overhanging control angle. Reproduced from (62).

It becomes of importance to account for the overhanging fraction correctly. This can be controlled by pixelation. The overhanging control angles are divided into $N_{\theta p} \, x \, N_{\phi p}$ pixels, allowing thus to treat the energy of each pixel as incoming or outgoing. The pixelation chosen for the DOM was of 3x3, as recommended by the Fluent Theory Guide.

All walls in the computational domain, except for those defining the UV-A tubes, have been set to opaque walls with internal emissivity equal to unity. Thus, radiation was not transmitted through these walls and no reflection was modelled. To model the emission of UV-A radiation from the tubes the emitted irradiation was calculated from

the tube power, in W, divided by the surface area of the tube's sleeve, in m^2, accounting for a 15% UV depreciation. The used data can be found in the product's data sheet (61). The calculated irradiation for each tube was 88 W/m^2, defined with a diffuse fraction of 1 to apply the irradiation circumferentially.

In the following, the results of the simulation cases are presented and compared.

5.3.5. SIMULATION RESULTS

The first set of simulation cases investigated the effect of inlet velocity on turbulent parameters and reaction rate. The inlet velocity was varied from 0.36 to 3 m/s.
All the parameters plotted and referred to in this section, apart from the residence time and inlet velocity, were averaged over the area these correspond to.

Figure 5-21 show that the increased velocity, at both TiO_2-covered surfaces, baffles and reactor shell enhanced the area-averaged reaction rate. The resulted area-averaged reaction rates have the same order of magnitude as those determined using the batch reactor and the prototype.

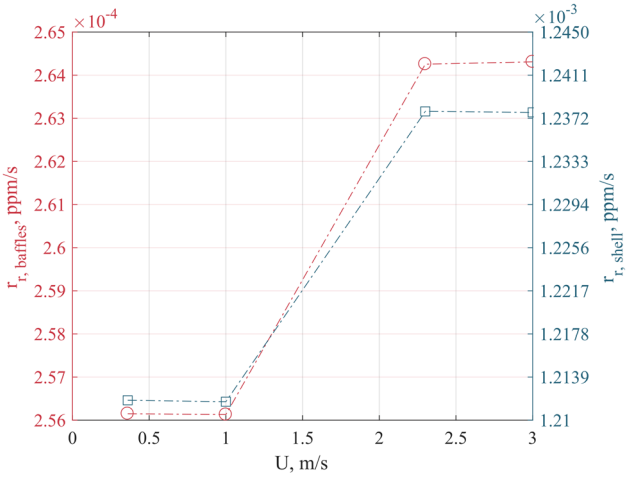

Figure 5-21 Area-averaged reaction rate at the baffles and shell surface, $r_{r,baffles}$ and r_{rshell}, respectively, as a function of inlet velocity, U.

Evaluating the C_2H_4 concentration, plotted in Figure 5-22, and the reaction rates simultaneously, at first glance it might appear counterintuitive that at faster rates the conversion was lower. The answer can be found in the average residence time of the molecules in the photocatalytic reactor.

A less beneficial effect of an increased velocity was the decrease in residence time, as presented in Figure 5-23. A low residence time retarded the exposure of molecules to

the active catalyst, as the species were fast transported to the outlet, away from the catalyst. Due to this, the C_2H_4 concentration levels remained high at $U = 2.3$ m/s and $U = 3$ m/s, which in turn dictated a high reaction rate. It has already been demonstrated and discussed that the more molecules are present at the surface the faster the reaction proceeds.

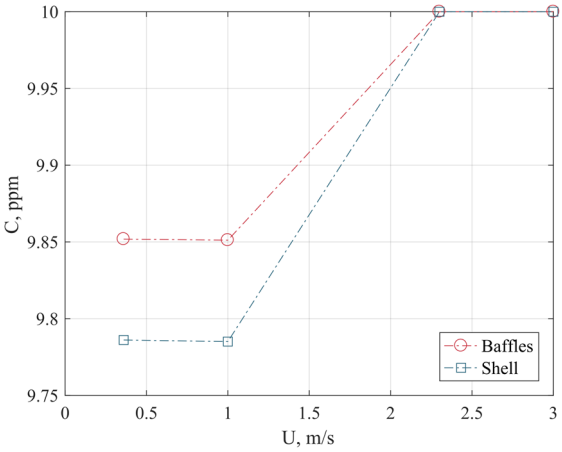

Figure 5-22 C_2H_4 concentration averaged over the TiO_2-coated baffles and shell surfaces.

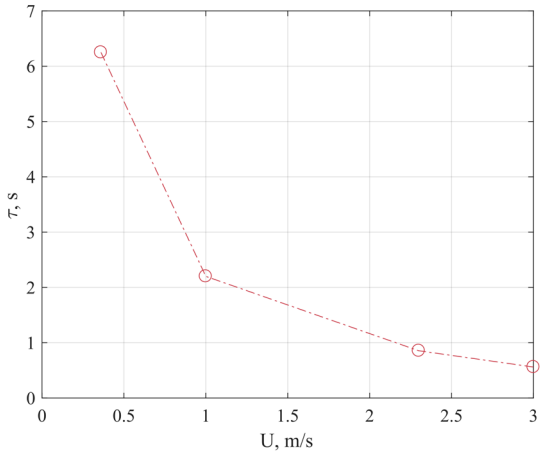

Figure 5-23 Residence time, τ, as a function of inlet velocity, U.

As expected, the intensity of the turbulence is increased with increasing velocity. This becomes obvious when plotting the turbulent kinetic energy, k, against the inlet velocity, U, given in Figure 5-24. The intensification of k can be correlated with the enhancement of the reaction rate, r_r, as the increase in velocity has the same effect on

both. To be noted is that the reaction differences in reaction rates, across the velocity range, are not substantial, due to the nature of the reaction. In spite of this, as a general guideline, turbulent mixing should be considered for this type of applications.

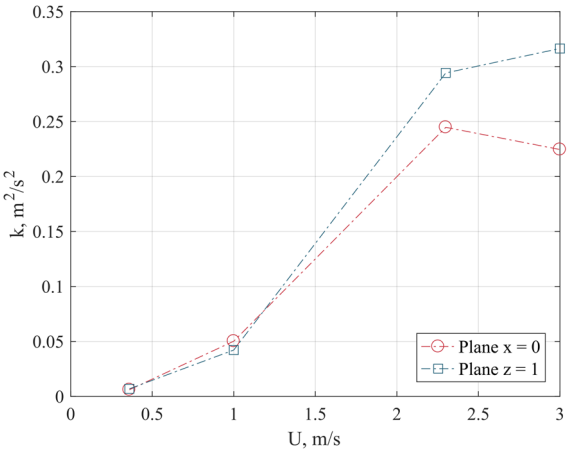

Figure 5-24 Turbulent kinetic energy, k, averaged over two different planes, versus inlet velocity, U. x = 0 – cuts the geometry longitudinally in half; z = 1 – placed before the reactor's outlet.

Observing the effect of velocity on reaction rate, it can be concluded that there is a trade-off between turbulence and residence time, when it comes to an optimal conversion. Moreover, it can be stated that a fast reaction, does not necessarily translate into a better conversion.

For the second set of simulations, the angle of the baffles relative to the axial coordinate (*y*-axis) was varied. The objective was to observe if this change in angle allows for a better radiation distribution. As listed in Table 5-6, the angle of the baffles was varied from 15 to 40 degrees, in five different simulations. The area-averaged radiation incident on the baffles and the shell of the reactor was plotted against the corresponding angle in Figure 5-25 and Figure 5-26, respectively. Indeed, an increase in angle results in a larger area of the surface being irradiated at slightly higher intensities. The differences in area-averaged surface incident radiation and consequently reaction rate, across the investigated angle range, are negligible. Therefore, it cannot be stated that the conversion efficiency can be influenced by the baffles angles. Similarly, although not represented here, the effect of baffles inclination on turbulent parameters, such as turbulent kinetic energy and turbulence intensity, was not significant. One could also argue that the small differences in area-averaged surface incident radiation and reaction rate could have been a consequence of numerical error. Thus, the variation of the inclination angle had no influence on the efficiency of the reactor, whether it was judged from a photonic or conversion efficiency point of view.

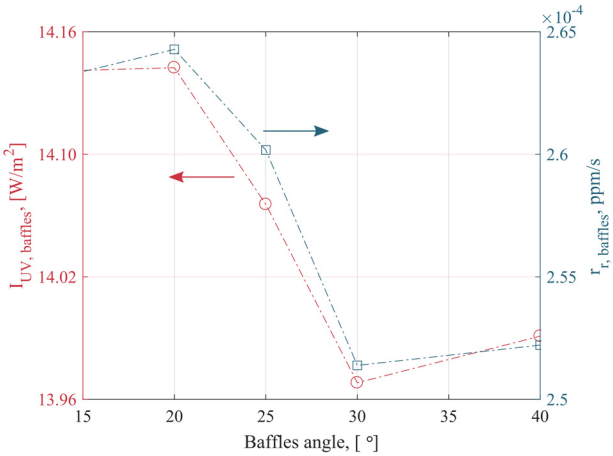

Figure 5-25 Area-averaged incident radiation on baffles surface as a function of baffles inclination angle and resulting area-averaged reaction rate.

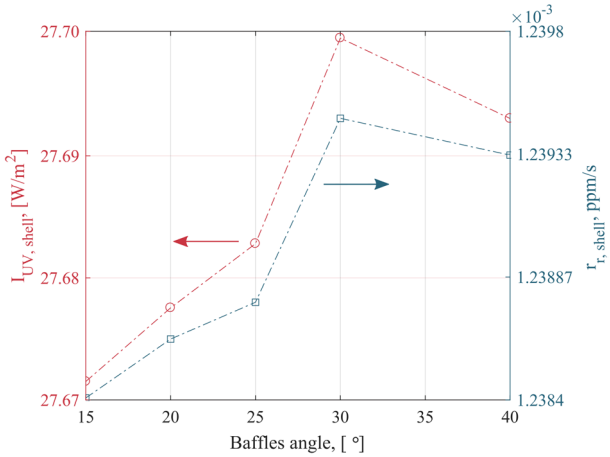

Figure 5-26 Area-averaged incident radiation on shell surface as a function of baffles inclination angle and resulting area-averaged reaction rate.

Figure 5-27 shows the distribution of the surface incident radiation on the baffles and the shells, respectively. The baffle inclination was 15°. The regions of these surfaces closest to the UV-A tubes were irradiated at a higher intensity. However, the area-averaged values of I_{UV} do not reflect the fact that there are small areas irradiated at > 40 W/m^2, while most of the baffles and shell surfaces were irradiated between 12-20 W/m^2 and 25-35 W/m^2, respectively. This could contribute to the observed low conversion, but no justified statement can be made. It was not possible to experimentally evaluate the irradiation limit at which the catalyst's activity would

have been significantly reduced, in this particular setting. As already mentioned, experiments could not be continued due to the deactivation of the catalyst surfaces. Nevertheless, the radiation was distributed well, with no shadow zones, due to the longitudinal and radial placement of the light sources.

Changing the geometry of the reactor to that represented in Figure 5-18 did not bring any major improvements in terms of conversion, compared to the simulation ran at the same flow conditions with the original geometry, S1-V1. The absence of turbulent mixing enhancement was attributed to the low velocity of 0.36 m/s. Thus, the conversion could be positively affected by the change in geometry at higher velocities. Time limited the simulation of further cases.
The radiation was distributed at the same extent as for S1-V1, which was considered a satisfactory distribution. This is t to the placement of the UV-A tubes, which allows the radiation of the enclosure efficiently, regardless of baffles angles or whether these are in line with the flow direction or perpendicular to it.

This ends the section on the CFD simulations. Conclusions are drawn at the end of the chapter.

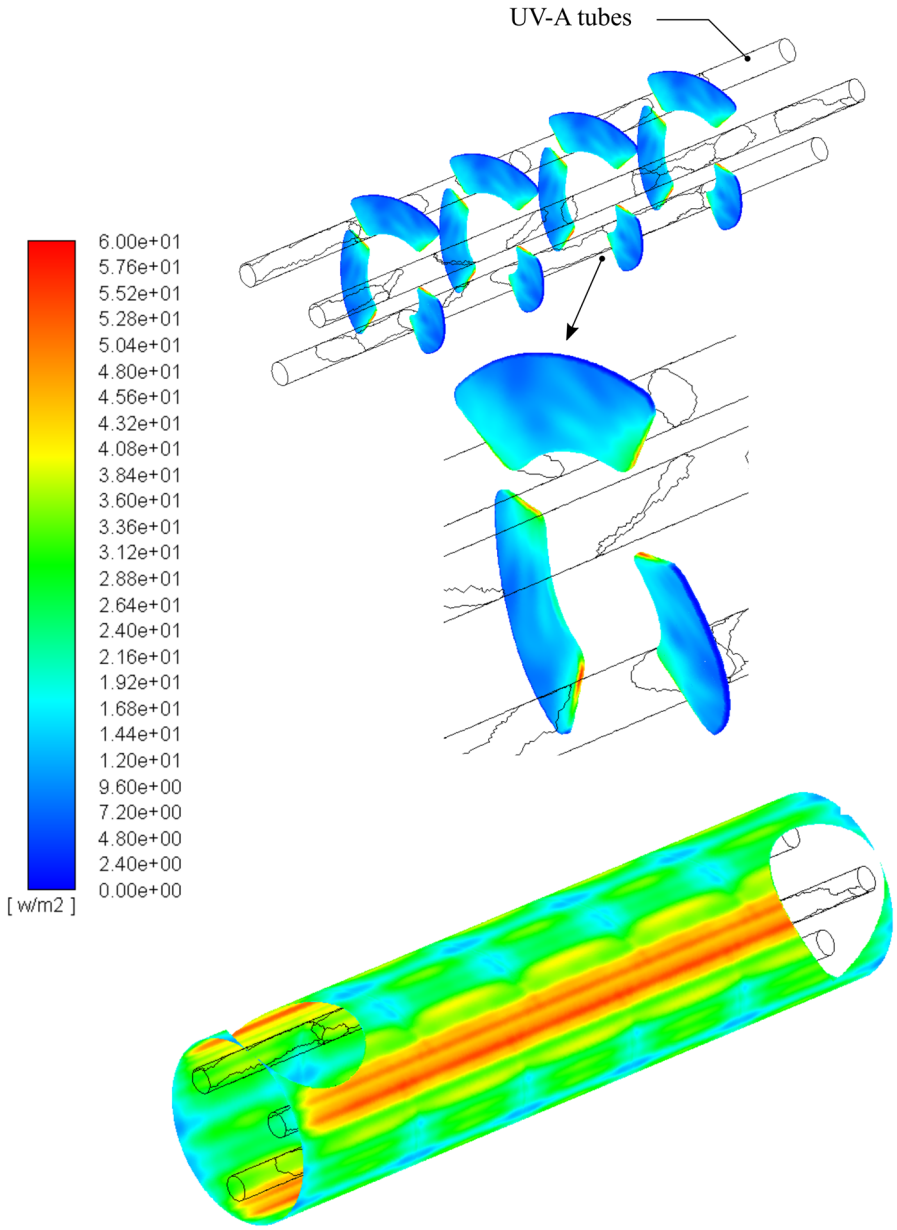

Figure 5-27 Contours of surface incident radiation on the baffles and shell. The inclination of the baffles was 15°. UV-A tubes shown for representation only.

5.4. TESTING A COMMERCIAL PRODUCT

The slow reaction rate and consequently low conversion, revealed by the CFD simulations, correlated with the high level of gas dilution in the facilities' atmosphere, led to the assumption that the efficiency of the device placed in a storage facility would be low. With this in mind and with the knowledge that products claiming to reduce VOC levels in enclosures are already on the market, it was decided to investigate the performance of a commercialized air-cleaning device. The product tested was the Jimco MAC500 from Jimco A/S, marketed as a household air-cleaning device *"specialized in combating odors by using patented UV-C and Ozone technology"*, according to their website. A test was conducted with the purpose of investigating the ability of the Jimco air-cleaning unit to degrade C_2H_4 in a foil chamber at DTI.

The test was conducted in an airtight 20 m^3 room, where the background C_2H_4 decay was determined to be < 1%. The room is shown in Figure 5-28. The ventilation to the room was blocked, in order to ensure no air exchange during the test.

Figure 5-28 Airtight room where the performance of the Jimco MAC500 air-cleaning device was tested.

All walls of the chamber were coated with a foil specially designed for minimal absorption of chemical compounds. The air in the room was mixed regularly, several times per hour, by a fan to ensure some level of air entrainment and mixing. Referring to the CFD simulations of the storage facility presented in section 3.2.3 (page 49), flow entrainment is beneficial for the transport of species, due to slow diffusion of C_2H_4 in air. The C_2H_4 evolution was recorded by a PTR-MS from Ionico and additionally by the F-940 gas analyzer from Felix instruments, previously during the storage facility measurement campaigns. The test was completed over the course of 5 days, during which the air cleaner had operating cycle of 12 h on – 12 h off. The cycle was controlled by a programmed timer.

Before the performance of the device was recorded in the form of C_2H_4 concentration, a precleaning of the room was performed. For this the device was placed in the room, kept off for 12 h and then turned on for another 12 h to degrade present VOCs. After this 24 h stage, C_2H_4 was added to the room by pumping approx. 20 L of 0.5% C_2H_4

in N_2 from a sample bag through a small tube. For 10 h after the addition of C_2H_4 the device was kept off in order to ensure a homogeneous gas mixture inside the enclosure, after which the 12 h on/off cycle was initiated.

Figure 5-29 shows the C_2H_4 concentration evolution over time, as recorded by the PTR-MS. The red segments correspond to the device being turned off, while the blue to on.

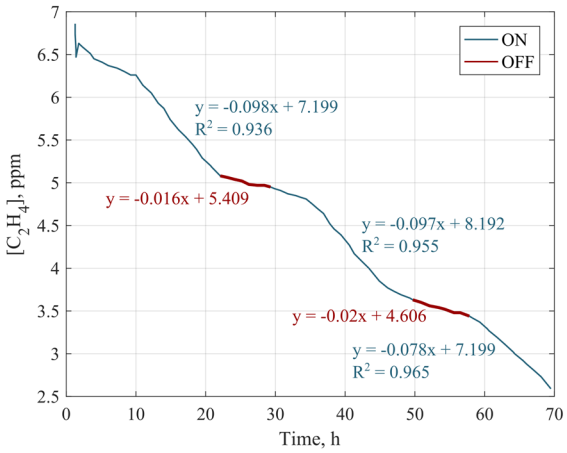

Figure 5-29 C_2H_4 concentration recorded by the PTR-MS during the Jimco test in the airtight room. Both on and off stages are represented.

A linear fit was associated to each segment. These reveal that the slope of the curves, indicating the magnitude of the C_2H_4 decay, is significantly higher when the device was on, compared to when it was off. Based on this, it can be stated that the Jimco air-cleaner degrades C_2H_4. Several tests allowed for the calculation of an average degradation rate of 0.19445e-04 ppm/s, with a maximum of 0.2278e-04 ppm/s. This rate is comparable to the reaction rate obtained in the batch reactor for the low initial concentrations investigated. Relative to the rate observed experimentally in the prototype, the decay rate of C_2H_4 due to the Jimco air-cleaner is an order of magnitude lower. It has to be kept in mind that the Jimco device was placed in a 20 m^3 room, not in a closed loop system, and that it is based on ozone and UV-C technology. Ozone technology cannot be used in the proximity of fresh produce as it is harmful to these.

An C_2H_4 level of 0.082 ppm in 20 m^3 at atmospheric pressure and room temperature corresponds to approx. 1.6 mL C_2H_4. Hence, the degradation was estimated to be maximum 1.6 mL/h. To put this into perspective, a quick estimate revealed that a degradation of 30 mL/h is needed in the engross storage facility at Aarstiderne.

Testing a commercial air cleaner brings forward the fact, that although technology-wise and design-wise air cleaners perform well, it is the transport of species to the device that causes inefficiency.

5.5. CONCLUDING REMARKS

A photocatalytic reactor was designed, targeting maximized contact between:

- C_2H_4 molecules and TiO_2 surface
- TiO_2 surface and photons, generated by the UV-A tubes.

In addition to this, modularity and ease of instalment were desired.

The physical prototype was tested under varying working conditions. The resulted behaviour was in agreement with expectations. Based on the screening tests performed with the physical prototype, the following observations were made.

The designed prototype is capable of degrading C_2H_4. Even though the observed reaction rate was slow, the device showed a conversion of 20% in 2 h, while working in closed loop regime. However, utilizing the prototype as an integrating part of a ventilation system means that the reactor needs a higher single-pass conversion, to lower the C_2H_4 concentration to acceptable levels. At this point, the low efficiency was justified by:

- Slow reaction rate, attributed to the high level of dilution of the gas phase.
- High RH – it is well known that H_2O molecules compete for the active sites of the catalyst, thus lowering the availability of free sites for C_2H_4 molecules to be degraded on.

Operating the prototype under different initial concentrations and varying volumetric flow rate, showed that the behavior of the prototype was in agreement with expectations. As previously experienced with the batch reactor, the prototype delivered a higher conversion with an increased initial C_2H_4 concentration. Similarly, increasing the volumetric flow rate, i.e. increased velocity, enhanced the reaction rate, however not significantly. This was attributed to a lowered residence time, as a result of increasing gas velocity. Hence, it can be concluded that a low gas velocity is more beneficial for the conversion. However, lowering the velocity also decreases the level of mixing. Therefore, there will always be a trade-off between residence time and turbulent mixing.

Working with the physical prototype, a degradation of the TiO_2 thin films was observed. This was identifiable by the lowered efficiency with time, and by surface oxidation. Unfortunately, this is a common phenomenon that needs to be overcome

when working with gaseous photocatalytic reactions. Nevertheless, it was surprising how early in the lifetime of the prototype the degradation signs started to show. It can be stated, that the degradation of the photocatalyst became a third reason for the low efficiency of the reactor.

Based on the CFD simulations performed, the following conclusions were drawn:

- It is troublesome to enhance the reaction rate significantly, wheather it is through turbulent mixing or high radiation flux. This is mainly due to the nature of application, where the concentrations handled are very low. This causes for a slow rate, even though it has been shown that an increase in velocity can accelerate it.
- There is a compromise to be taken when it comes to increasing the velocity for conversion efficiency. While the turbulence is intensified, the residence time is lowered, which gives a poor conversion. it appears that an increase in reaction rate does not equate to higher degradation efficiency.
- A variation in the inclination angle of the baffles did not result in any significant positive changes. The reaction rate was negligibly affected by a more intense irradiation, as the distribution of area-averaged surface incident radiation remained almost constant. This was mainly due to the placement of the UV-A tubes. Therefore, it can be concluded that their placement was optimal for good irradiation of the catalyst, under the current design.
- As stated above, working with extremely low concentrations, dictates a slow photocatalytic process. However, a decrease of only 1 ppm can make a significant difference for various fresh produce.
- Although the degradation of ethylene was low, it cannot be stated that the design of the photocatalytic reactor was faulty. It is considered that the main reason for the low degradation is the dilute nature of the gas flow and the large dimensions of the reactor.
- To back up the last statement, the C_2H_4 degradation in a 20 m^3 chamber was investigated, by employing a commercialized air-cleaner. The experiment revealed that indeed, the process of reducing C_2H_4, from an initial concentration of 7 ppm is a time-consuming process. One could consider investigating the reactor further, but reducing its dimensions/volume significantly.

CHAPTER 6. CLOSURE

This chapter sums up the main results of this dissertation. Furthermore, suggestions for how to continue the work in various directions are given.

6.1. FINAL REMARKS

Studying reports on food loss and waste made it clear how much of the food produced is wasted before it even makes it to the plate. This is a mixture of several factors, which arise through the whole food chain, from production to postharvest to end-user. A large percentage of food loss, and in consequence of its environmental impact, is connected to fresh produce wastage. A key role in fresh produce spoilage is played by the plant hormone C_2H_4, which is essential in plant growth and ripening, but is also responsible for degradation. The majority of fresh produce and flowers are highly sensitive to C_2H_4. Even a build-up of 0.01 ppm can trigger the degradation process, visible as texture and color changes.

The case studies on food loss conducted as part of this project have shown that food loss translates into financial losses from 1.7 to a staggering of 60 million DKK per year. It was difficult to estimate the percentage attributed to C_2H_4. Nevertheless, measurement campaigns at a storage facility revealed that C_2H_4 is released and builds-up at harmful levels inside the enclosure. Concentrations of up to 37 ppm at packaging level and up to 1.5 ppm at the facility's environmental level have been recorded. For most fresh produce these levels are harmful, accelerating their degradation and thus, minimizing their shelf life. Therefore, based on the measurements and reports from the involved project partners, activating in the postharvest industry, an C_2H_4 monitoring and removing solution was reported to be useful. This solution was to be based on the photocatalytic degradation of C_2H_4 over TiO_2 thin films.

The kinetic model was of paramount importance for understanding the photocatalytic process employed, as well as for modelling-purposes. The kinetic studies demonstrated that the kinetics are highly dependent on compound initial concentration. Experiments have shown that depending on concentration level, a zero-order rate model or the popular Langmuir-Hinshelwood (LH) kinetic model can define the photocatalytic reaction. Moreover, kinetics studies revealed that for the current application the LH kinetic model could be reduced to a fundamental first-order rate law. As expected, the rate was enhanced by both increasing initial concentration and surface incident radiation. The derived kinetic parameters have an exponential dependence to initial concentration and a linear dependence to irradiance.

Investigating the possibility of utilizing a photocatalytic reactor for degrading C_2H_4 in storage facilities and transportation trucks led to the design and manufacturing of an air-cleaning prototype. This was designed to maximize species – catalyst and

photons – catalyst contact, and to prolong residence time. In addition, for ease of installment the reactor was configured to be an integrating part of a ventilation system. The studies conducted at the storage facility showed a very dilute mixture of contaminant in air, which in combination with the slow diffusion of C_2H_4 in air, uncovered a potential risk for employing an air-cleaning device. The dilute mixture translated into a slow reaction rate, as showed by both the kinetic studies in the batch reactor, as well as experiments and simulations of the prototype. Moreover, the slow diffusion translated into an inefficient transport of species to the device.

Computational investigation through CFD of the proposed prototype revealed a troublesome acceleration of the photocatalytic process, due to the slow reaction rate governing the process. Both altering the radiation distribution on the catalyst surfaces and intensifying the turbulence mixing, had little to no effect on the conversion efficiency. However, it was observed concluded that in this case a fast reaction does not necessarily result in high conversion efficiency. Moreover, when increasing the inlet velocity if the gas flow to obtain better mixing, one should be aware of the effect this can have on the species residence time. A low residence time has a retarding effect om the photocatalytic reaction rate.

A common issue of photocatalytic technologies is the deactivation of the photocatalyst, mostly noted for gaseous systems. This issue was encountered during this study as well, for both reactor types – batch and continuous flow. It was considered that the kinetics derived using the batch reactor were not affected by the deactivation, as multiple TiO_2-coated plates were available, all from the same coating batch. Hence, the catalyst plate was changed when showing signs of deactivation. When the prototype exhibited a decrease in efficiency, due to catalyst deactivation the tests were ceased, as it was time and financially consuming to change all the internal elements coated with TiO_2. Due to this, a kinetic study of the prototype, as well as generating data for model validation were not possible.

Summing up, the main contributions of this work are:

- Derivation of a kinetic model, describing the photocatalytic degradation of C_2H_4 over TiO_2 thin films, under varying initial concentration of C_2H_4 and incident surface radiation.
- Development of the design of a photocatalytic reactor.
- Parametric study of the proposed design through Computational Fluid Dynamics simulations.

6.2. OUTLOOK AND FUTURE WORK

If one single statement were to be made regarding the kinetics of the photocatalytic oxidation of C_2H_4 over TiO_2 thin films is that these are intrinsic.
Experimental investigations of the reaction rate were conducted under low concentrations between 10 to 27 ppm. However, it can be argued that kinetics should be studied at even lower concentrations, in order to emulate storage conditions at a higher degree. A shift in reaction order has been experienced during the present study. Thus, the possibility of another shift for lower C_2H_4 levels is to be taken into account. Moreover, different reactor types and different reaction conditions, such as temperature and relative humidity, can impose different kinetics. Due to this intrinsic nature of the reaction kinetics, it can be suggested that a separate kinetic study applied to the prototype is necessary. To extend the rate model, the reaction needs to be investigated under sets of different reaction conditions. In addition, research studies on deriving a generally valid rate model could also be conducted.

It has become quite clear through this study, that operating one single C_2H_4-degrading unit in large enclosures is not an optimal solution, due to the slow diffusion of species and highly diluted gas mixtures. Nevertheless, testing the already manufactured prototype in a storage facility would have been interesting.
As a future work suggestion, other designs and/or implementation strategies of air-cleaning devices could be investigated. To give an example, multiple small-scale reactors (mini-reactors) could be installed at average heights corresponding to stored fresh produce packages. This would eliminate the need of transporting the contaminant species to a device, installed at a significant distance from the contamination source.

Addressing the issue of catalyst deactivation – an in-depth study of the produced TiO_2 coating, on a nanostructure level, could give an insight into potential issues and at the same time solutions. Several substrate materials could be investigated, as already done in this study, but on a longer period or under higher radiation conditions, to accelerate potential deactivation.

LITERATURE LIST

1. FAO. Food wastage footprint. Impacts on natural resources. Summary Report. Food and Agriculture Organization of the United Nations (FAO). 2013.

2. FAO. Global initiative on Food Loss and Waste [Internet]. Rome, Italy; 2018. Available from: www.fao.org/platform-food-loss-waste

3. J. Gustavsson, C. Cederberg, U. Sonesson, R. van Otterdijk A, Meybeck. Global Food Losses and Food Waste - Extent, Causes and Prevention. Rome, Italy; 2011.

4. HLPE. Food Losses and Waste in the Context of Sustainable Food Systems. A Report by the High Level Panel of Experts on Food Security and Nutrition of the Committee on World Food Security [Internet]. Rome; 2014. Available from: http://www.fao.org/3/a-i3901e.pdf

5. Nahman A, de Lange W. Costs of food waste along the value chain: Evidence from South Africa. Waste Manag. 2013 Nov;33(11):2493–500.

6. Lipinski B, O'Connor C, Hanson C. SDG Target 12.3 on Food Loss and Waste: 2016 Progress Report [Internet]. 2016. Available from: https://champs123blog.files.wordpress.com/2016/09/sdg-target-12-3-progress-report_2016.pdf

7. United Nations. Goal 2: Zero Hunger [Internet]. 2019 [cited 2019 Jul 29]. Available from: https://www.un.org/sustainabledevelopment/hunger/

8. United Nations. Transforming our world: the 2030 Agenda for Sustainable Development. 2015.

9. Macheka L, Spelt E, van der Vorst JGAJ, Luning PA. Exploration of logistics and quality control activities in view of context characteristics and postharvest losses in fresh produce chains: A case study for tomatoes. Food Control. 2017 Jul;77:221–34.

10. Kader A, Rolle R. The Role of Post-Harvest Management in Assuring the Quality and Safety of Horticultural Produce. Rome, Italy: Food and Agriculture Organization of the United Nations; 2004.

11. Burden J, Wills RBH, Smith K. Prevention of post-harvest food losses: fruits, vegetables and root crops. A training manual [Internet]. FAO; 2014. Available from: http://www.fao.org/docrep/t0073e/t0073e00.htm

12. Keller N, Ducamp MN, Robert D, Keller V. Ethylene removal and fresh product storage: A challenge at the frontiers of chemistry. Toward an approach by photocatalytic oxidation. Chem Rev. 2013;113(7):5029–70.

13. Pathak N, Caleb OJ, Geyer M, Herppich WB, Rauh C, Mahajan P V. Photocatalytic and Photochemical Oxidation of Ethylene: Potential for Storage of Fresh Produce—a Review. Food Bioprocess Technol. 2017;10(6):982–1001.

14. Thompson AK. Controlled Atmosphere Storage. In: Fruit and Vegetable Storage: Hypobaric, Hyperbaric and Controlled Atmosphere. Huddersfield, United Kingdom: Springer International Publishing; 2016. p. 21–36.

15. Thompson AK. Hypobaric Storage. In: Fruit and Vegetable Storage: Hypobaric, Hyperbaric and Controlled Atmosphere. Huddersfield, United Kingdom: Springer International Publishing; 2016. p. 37–92.

16. Carp O, Huisman CL, Reller A. Photoinduced reactivity of titanium dioxide. Prog Solid State Chem. 2004;32(1–2):33–177.

17. Moseley PT. Solid State Gas Sensors. Meas Sci Technol. 1997;8:223–37.

18. Savage NO, Akbar SA, Dutta PK. Titanium dioxide based high temperature carbon monoxide selective sensor. Sensors Actuators B Chem. 2001 Feb 10;72(3):239–48.

19. Oh WS, Xu C, Kim DY, Goodman DW. Preparation and characterization of epitaxial titanium oxide films on Mo(100). J Vac Sci Technol A. 1997 May 1;15(3):1710–6.

20. Zhang F, Zheng Z, Chen Y, Liu X, Chen A, Jiang Z. In vivo investigation of blood compatibility of titanium oxide films. J Biomed Mater Res. 1998 Oct 1;42(1):128–33.

21. Hadjiivanov KI, Klissurski DG. Surface chemistry of titania (anatase) and titania-supported catalysts. Chem Soc Rev. 1996;25(1):61–9.

22. Kittel C. Introduction to Solid State Physics. 8th ed. Wiley; 2004.

23. Schneider J, Bahnemann D, Ye J, Li Puma G, Dionysiou DD. Photocatalysis: Fundamentals and Perspectives. The Royal Society of Chemistry; 2016. P001-436 p. (Energy and Environment Series).

24. Chang K-L, Sekiguchi K, Wang Q, Zhao F. Removal of Ethylene and

Secondary Organic Aerosols Using UV-C254 + 185 nm with TiO2 Catalyst. Aerosol Air Qual Res. 2013;13(2):618–26.

25. Hussain M, Bensaid S, Geobaldo F, Saracco G, Russo N. Photocatalytic degradation of ethylene emitted by fruits with TiO2 nanoparticles. Ind Eng Chem Res. 2011;50(5):2536–43.

26. Hauchecorne B, Tytgat T, Verbruggen SW, Hauchecorne D, Terrens D, Smits M, et al. Photocatalytic degradation of ethylene: An FTIR in situ study under atmospheric conditions. Appl Catal B Environ. 2011;105(1–2):111–6.

27. Yamazaki S, Tanaka S, Tsukamoto H. Kinetic studies of oxidation of ethylene over a TiO2 photocatalyst. J Photochem Photobiol A Chem. 1999;121(1):55–61.

28. Fu X, Clark LA, Zeltner WA, Anderson MA. Effects of reaction temperature and water vapor content on the heterogeneous photocatalytic oxidation of ethylene. J Photochem Photobiol A Chem. 1996;97(3):181–6.

29. Park D-R, Zhang J, Ikeue K, Yamashita H, Anpo M. Photocatalytic Oxidation of Ethylene to CO2 and H2O on Ultrafine Powdered TiO2 Photocatalysts in the Presence of O2 and H2O. J Catal. 1999 Jul 1;185(1):114–9.

30. Ye S, Tian Q, Song X, Luo S. Photoelectrocatalytic degradation of ethylene by a combination of TiO2 and activated carbon felts. J Photochem Photobiol A Chem. 2010;208(1):27–35.

31. Sirisuk A, Hill CG, Anderson M a. Photocatalytic degradation of ethylene over thin films of titania supported on glass rings. Catal Today. 1999;54(1):159–64.

32. Deutschmann O, Knözinger H, Kochloefl K, Turek T. Heterogeneous Catalysis and Solid Catalysts. In: Ullmann's Encyclopedia of Industrial Chemistry. American Cancer Society; 2009.

33. Vincent G, Schaer E, Marquaire PM, Zahraa O. CFD modelling of an annular reactor, application to the photocatalytic degradation of acetone. Process Saf Environ Prot. 2011;89(1):35–40.

34. Obee TN, Hay SO. Effects of moisture and temperature on the photooxidation of ethylene on titania. Environ Sci Technol. 1997;31(7):2034–8.

35. Obee TN, Brown RT. TiO2 Photocatalysis for Indoor Air Applications : Effects of Humidity and Trace Contaminant Levels on the Oxidation Rates of

Formaldehyde, Toluene, and1,3-Butadiene. Environ Sci Technol. 1995;29(5):1223–31.

36. Obee TN. Photooxidation of Sub-Parts-per-Million Toluene and Formaldehyde Levels on Titania Using a Glass-Plate Reactor. Environ Sci Technol. 1996 Nov 1;30(12):3578–84.

37. Cao L, Spiess F-J, Huang A, Suib SL, Obee TN, Hay SO, et al. Heterogeneous Photocatalytic Oxidation of 1-Butene on SnO2 and TiO2 Films. J Phys Chem B. 1999 Apr 1;103(15):2912–7.

38. Zhang P, Liu J. Photocatalytic degradation of trace hexane in the gas phase with and without ozone addition: kinetic study. J Photochem Photobiol A Chem. 2004 Oct 1;167(2–3):87–94.

39. Li Puma G, Salvadó-Estivill I, Obee TN, Hay SO. Kinetics rate model of the photocatalytic oxidation of trichloroethylene in air over TiO2 thin films. Sep Purif Technol. 2009;67(2):226–32.

40. Ching W., Leung M, Leung DY. Solar photocatalytic degradation of gaseous formaldehyde by sol–gel TiO2 thin film for enhancement of indoor air quality. Sol Energy. 2004 Jan 1;77(2):129–35.

41. Shiraishi F, Toyoda K, Miyakawa H. Decomposition of gaseous formaldehyde in a photocatalytic reactor with a parallel array of light sources: 2. Reactor performance. Chem Eng J. 2005 Nov 15;114(1–3):145–51.

42. Pathak N, Caleb OJ, Rauh C, Mahajan P V. Effect of process variables on ethylene removal by vacuum ultraviolet radiation: Application in fresh produce storage. Biosyst Eng. 2017 Jul 1;159:33–45.

43. Walsem J Van, Verbruggen SW, Modde B, Lenaerts S, Denys S. CFD investigation of a multi-tube photocatalytic reactor in non-steady- state conditions. Chem Eng J. 2016;304:808–16.

44. Héquet V, Raillard C, Debono O, Thévenet F, Locoge N, Le Coq L. Photocatalytic oxidation of VOCs at ppb level using a closed-loop reactor: The mixture effect. Appl Catal B Environ. 2018 Jun 15;226:473–86.

45. Islam MA. Einstein – Smoluchowski Diffusion Equation : A Discussion. Phys Scr. 2004;70:120–5.

46. Bird RB, Stewart WE, Lightfoot EN. Transport Phenomena. 2nd ed. Wiley; 2006. 928 p. (Wiley International edition).

47. Mitcham EJ, Crisosto CH, Kader AA. Apples, Golden Delicious: Recommendations for Maintaining Postharvest Quality. 1999; Available from: http://postharvest.ucdavis.edu/Commodity_Resources/Fact_Sheets/Datastores/Fruit_English/?uid=3&ds=798

48. Nielsen MG, In S Il, Vesborg PCK, Pedersen T, Almtoft KP, Andersen IH, et al. A generic model for photocatalytic activity as a function of catalyst thickness. J Catal. 2012;289:62–72.

49. Stroe R-E, Rosendahl LA. Kinetic study of the photocatalytic oxidation of ethylene over TiO2 thin films. IOP Conf Ser Mater Sci Eng. 2019;628.

50. NIST. Ethylene. In: Standard Reference Database 69: NIST Chemistry WebBook [Internet]. 2018. Available from: https://webbook.nist.gov/cgi/cbook.cgi?ID=C74851&Mask=20#

51. Lee D-J, Park Y-K, Kim S-J, Lee H, Jung S-C. Photo-catalytic destruction of ethylene using microwave discharge electrodeless lamp. Korean J Chem Eng. 2015;32(6):1188–93.

52. Einaga H, Tokura J, Teraoka Y, Ito K. Kinetic analysis of TiO2-catalyzed heterogeneous photocatalytic oxidation of ethylene using computational fluid dynamics. Chem Eng J. 2015;263:325–35.

53. Kim SB, Hong SC. Kinetic study for photocatalytic degradation of volatile organic compounds in air using thin film TiO2 photocatalyst. Appl Catal B Environ. 2002 Jan 25;35(4):305–15.

54. González-García N, Ayllón JA, Doménech X, Peral J. TiO2 deactivation during the gas-phase photocatalytic oxidation of dimethyl sulfide. Appl Catal B Environ. 2004 Sep 8;52(1):69–77.

55. El-Alami W, Garzón Sousa D, Díaz González JM, Fernández Rodríguez C, González Díaz O, Doña Rodríguez JM, et al. TiO2 and F-TiO2 photocatalytic deactivation in gas phase. Chem Phys Lett. 2017 Sep 16;684:164–70.

56. Turchi CS, Ollis DF. Photocatalytic degradation of organic water contaminants: Mechanisms involving hydroxyl radical attack. J Catal. 1990;122(1):178–92.

57. Peral J, Ollis DF. TiO2 photocatalyst deactivation by gas-phase oxidation of heteroatom organics. J Mol Catal A Chem. 1997 Jan 29;115(2):347–54.

58. Sauer ML, Ollis DF. Catalyst Deactivation in Gas–Solid Photocatalysis. J Catal. 1996 Sep 15;163(1):215–7.

59. Piera E, Ayllón JA, Doménech X, Peral J. TiO2 deactivation during gas-phase photocatalytic oxidation of ethanol. Catal Today. 2002 Nov 15;76(2–4):259–70.

60. Ebmpapst. Energy-saving axial fan. W1G230-EB89-01 [Internet]. Available from: https://www.ebmpapst.co.uk/en/products/axialfans/axialfansdetail.php?pID=120930

61. Philips. Flexo Print TL 60W/10-R SLV/25 UV-A lamp. Available from: https://www.lighting.philips.com/main/prof/conventional-lamps-and-tubes/special-lamps/reprography/flexo-print/flexo-print/928008401003_EU/product

62. Fluent ANSYS. ANSYS FLUENT 19.1 Theory Guide. USA: ANSYS Inc.; 2019.

63. Andersson B, Andersson R, Håkansson L, Mortensen M, Sudiyo R, van Wachem B. Computational Fluid Dynamics for Engineers. Cambridge University Press; 2011.

64. Wang Z, Liu J, Dai Y, Dong W, Zhang S, Chen J. Dimethyl sulfide photocatalytic degradation in a light-emitting-diode continuous reactor: Kinetic and mechanistic study. Ind Eng Chem Res. 2011;50(13):7977–84.

65. Wang Z, Liu J, Dai Y, Dong W, Zhang S, Chen J. CFD modeling of a UV-LED photocatalytic odor abatement process in a continuous reactor. J Hazard Mater. 2012 May 15;215–216:25–31.

66. Yang R, Zhang Y-P, Zhao R-Y. An Improved Model for Analyzing the Performance of Photocatalytic Oxidation Reactors in Removing Volatile Organic Compounds and Its Application. J Air Waste Manage Assoc. 2004 Dec 1;54(12):1516–24.

67. Khodadadian F, de Boer MW, Poursaeidesfahani A, van Ommen JR, Stankiewicz AI, Lakerveld R. Design, characterization and model validation of a LED-based photocatalytic reactor for gas phase applications. Chem Eng J [Internet]. 2018 Feb 1 [cited 2018 Apr 19];333:456–66. Available from: https://www.sciencedirect.com/science/article/pii/S1385894717316078?_rdoc=1&_fmt=high&_origin=gateway&_docanchor=&md5=b8429449ccfc9c30159a5f9aeaa92ffb

68. Roegiers J, van Walsem J, Denys S. CFD- and radiation field modeling of a gas phase photocatalytic multi-tube reactor. Chem Eng J [Internet]. 2018 Apr 15 [cited 2018 Jun 13];338:287–99. Available from: https://www.sciencedirect.com/science/article/pii/S1385894718300470?_rdoc=1&_fmt=high&_origin=gateway&_docanchor=&md5=b8429449ccfc9c30159a5f9aeaa92ffb

69. Leblebici ME, Rongé J, Martens JA, Stefanidis GD, Gerven T Van. Computational modelling of a photocatalytic UV-LED reactor with internal mass and photon transfer consideration. Chem Eng J [Internet]. 2015;264:962–70. Available from: http://dx.doi.org/10.1016/j.cej.2014.12.013

70. Elektronika S.A. Friga-Bohn. Model TA 4R 4P. 2019; Available from: https://www.elektronika-sa.com.pl/tcmodel.php?line=XFCUB-TA-2005&model=TA 4 R 4P

APPENDICES

Appendix A. Aarstiderne Storage Facility

The following pictures present the storage facility where enclosure C_2H_4 levels have been monitored. Figure A-1 shows the layout of the whole facility, displaying dimensions and the division into multiple storage rooms. The middle storage room was the one used for placing the sensors that recorded C_2H_4 and CO_2 levels, as well as temperature and RH. The room contained a multitude of fruits and vegetables, expect bananas and avocados, as these were kept in so-called “ripening rooms”, where temperature was high and C_2H_4 was supplied to the air in order to initiate their ripening. Such a room is the small enclosure in the bottom right of Figure A-1. Figure A-2 and Figure A-3 show placement of produce stacks and examples of various fresh produce.

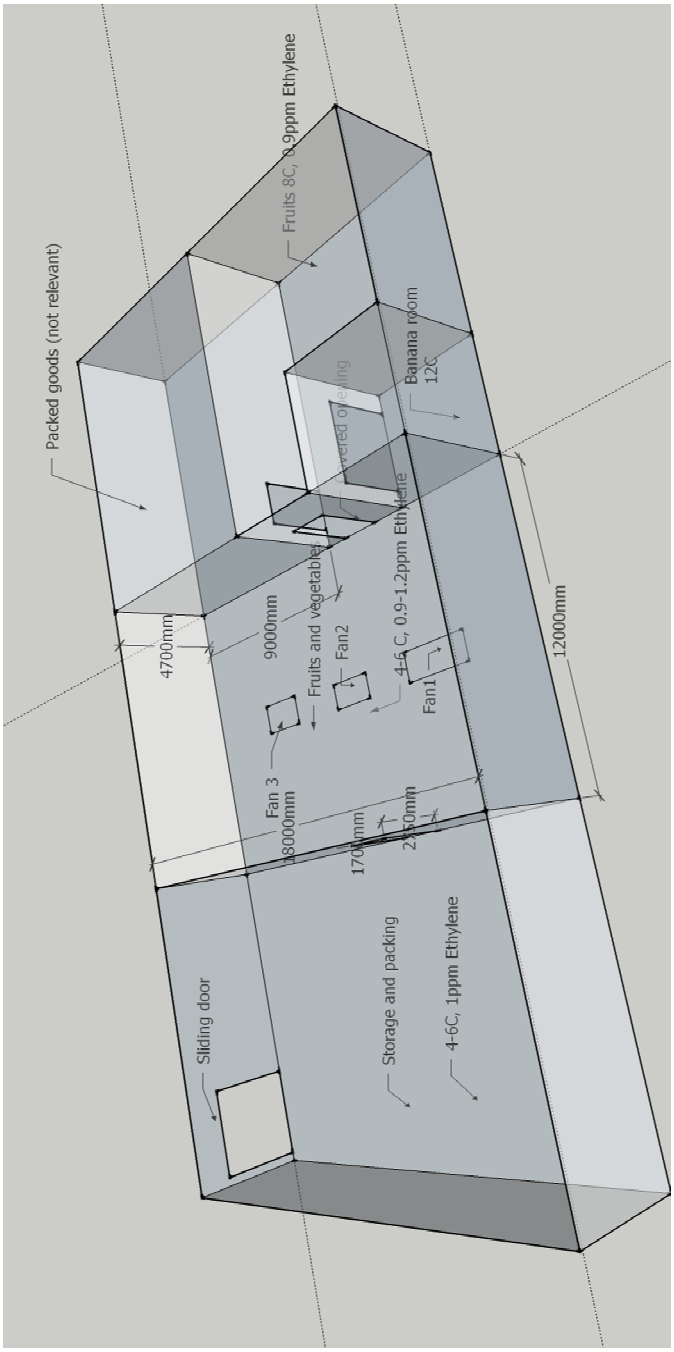

Figure A-1 Storage facility layout.

Figure A-2 Stacked fresh produce, dispersed throughout the whole storage room.

Figure A-3 Stacks of various fruits present at the beginning of the measurement campaign: (a) apples and pears; (b) pears, plums, apples; (c) apples, grapefruits.

Figure A-4 Stacks of various vegetables present at the beginning of the measurement campaign: (a) Romanesco broccoli, cabbage, bean pods; (b) tomatoes, squash.

Appendix B. Ventilation unit data sheet

The following data sheet is extracted from the product's documentation. The unit is a dual-discharge unit cooler, from Friga-Bohn, model TA 4R 4P. The document was accessed via (70). Only the relevant page is presented here and the chosen model feature is marked within the orange box.

R404A | **CO2** | **W** | tA1 | TA ... 4P | +E1K

+15 | +2 | -1°C

TA ... R 4P - 1,500 rpm — 3,63 mm

		TA ... R 4P	1	2	3	4	5	6	7
Capacity R404A (1)	DT1 = 10 K - SC 1 kW		5,20	7,97	9,87	10,78	14,97	18,34	21,86
	DT1 = 8 K - SC 2 kW		3,38	5,31	6,53	7,00	9,93	12,18	14,42
Capacity CO2 (7)	DT1 = 8 K - SC 2 kW		3,69	4,88	6,47	7,53	9,61	11,36	13,26
Acoustic	Lp 4 m (2) dB(A)		39	42	42	42	44	44	45
Surface	m^2		15,0	15,0	22,5	29,9	33,7	56,1	59,9
Circuit volume	dm^3		2,2	2,2	3,3	4,5	5,0	8,4	8,9
	Nb		1	2	2	2	3	3	4
Fan Ø 350 mm 230 V/1/50-60 Hz	Air flow	m^3/h	1920	4210	4010	3850	6020	5560	7700
	Air throw (3)	m	2 x 10	2 x 12	2 x 11	2 x 10	2 x 11	2 x 10	2 x 10
	230 V/1/50 Hz	W max	1 x 220	2 x 220	2 x 220	2 x 220	3 x 220	3 x 220	4 x 220
		A max	1 x 1,1	2 x 1,1	2 x 1,1	2 x 1,1	3 x 1,1	3 x 1,1	4 x 1,1
Electric defrost E1K (4)	230 V/1/50 Hz	W total	800	800	1200	1600	1800	3000	3200
		A total	3,5	3,5	5,2	7,0	7,8	13,0	14,0
	400 V/3/50 Hz	W total	-	-	-	-	-	3000	3200
		A total	-	-	-	-	-	6,5	6,9
Net weight	kg		23	25	28	33	36	45	55

TA ... L 4P - 1,500 rpm — 6,35 mm

		TA ... L 4P	1	2	3	4	5	6	7
Capacity R404A (1)	DT1 = 10 K - SC 1 kW		4,48	7,30	8,53	9,27	10,26	14,92	18,84
	DT1 = 8 K - SC 2 kW		2,92	4,89	5,66	6,08	6,75	10,01	12,45
Capacity CO2 (7)	DT1 = 8 K - SC 2 kW		3,46	5,07	6,16	6,98	7,64	9,97	12,16
Capacity W (8)	DT1 = 10 K (a) kW		4,83	-	-	9,84	-	15,62	20,02
	DT1 = 8 K (b) kW		3,14	-	-	6,50	-	10,53	13,20
Acoustic	Lp 4 m (2) dB(A)		39	42	42	42	44	44	45
Surface	m^2		11,2	13,5	18,0	22,5	20,2	33,7	45,0
Circuit volume	dm^3		2,8	3,3	4,5	5,6	5,0	8,4	11,2
	Nb		1	2	2	2	3	3	4
Fan Ø 350 mm 230 V/1/50-60 Hz	Air flow	m^3/h	1980	4210	4070	3950	6320	5930	7900
	Air throw (3)	m	2 x 11	2 x 12	2 x 11	2 x 11	2 x 12	2 x 11	2 x 11
	230 V/1/50 Hz	W max	1 x 220	2 x 220	2 x 220	2 x 220	3 x 220	3 x 220	4 x 220
		A max	1 x 1,1	2 x 1,1	2 x 1,1	2 x 1,1	3 x 1,1	3 x 1,1	4 x 1,1
Electric defrost E1K (4)	230 V/1/50 Hz	W total	800	800	1200	1600	1800	3000	3200
		A total	3,5	3,5	5,2	7,0	7,8	13,0	14,0
	400 V/3/50 Hz	W total	-	-	-	-	-	3000	3200
		A total	-	-	-	-	-	6,5	6,9
Net weight	kg		21	27	30	32	35	44	58

		TA ... 4P	1	2	3	4	5	6	7
Dimensions	A mm		872	1372	1372	1372	1872	1872	2372
	H mm		17,5	17,5	17,5	17,5	35	35	35
	X mm		560	1060	1060	1060	1560	1560	2060
Connections R404A	Inlet Ø (5)		D 5/8"	D 5/8"	D 5/8"	D 5/8"	D 5/8"	D 5/8"	D 5/8"
	Outlet Ø ODF (6)		5/8"	5/8"	7/8"	7/8"	7/8"	1"1/8	1"1/8

(1) Standard conditions (Eurovent) :
SC1 / +10°C (air inlet temp.) / 0 °C (evaporating temp.) / DT1 = 10K
SC2 / 0°C (air inlet temp.) / -8°C (evaporating temp.) / DT1 = 8K
(2) Average sound pressure level in dB(A) measured at 4 m, at fan height, in direct line of sight on a reflective surface, given for information only..
(3) Residual air speed: 0.25 m/s.
(4) Electric defrost option.
(5) Distributor: Male to be brazed.
(6) ODF: Female to receive a tube of the same diameter.
(7) Operating pressure 60 bar - Tube diameter to define the order.
(8) Glycol water:
(a) EG Percent. glycol = 30% - Fluid inlet temp. = -2°C - Fluid outlet temp. = +2°C
Inlet dry temp. = +10 - relative humidity = 85%
(b) EG Percent. glycol = 30% - Fluid inlet temp. = -8 - Fluid outlet temp. = -4
Inlet dry temp. = +2 - relative humidity = 85%
Other conditions: please contact us.

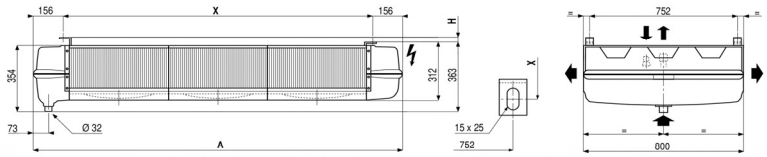

BAE	BXT	WCO	CO2	PRK	HGB	E1K	E1U	2TH	DMP	EEC
O	O			O	O	O	O	O	O	O

Figure A-5 Facility ventilation unit data sheet (70).

Appendix C. Zero Order Kinetic Data

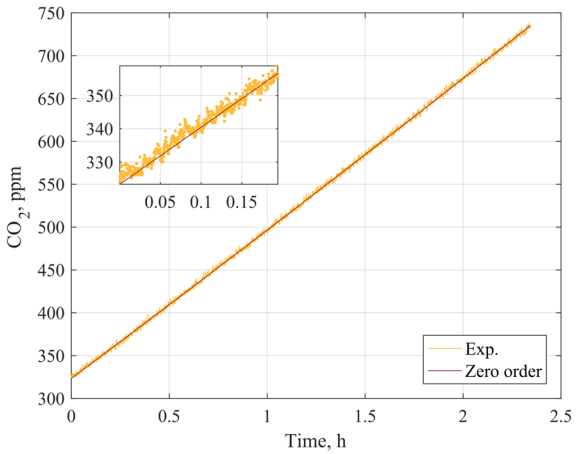

Figure A-6 Zero order rate law fit to experimental data 1. $[CO_2]_0$ = 325 ppm, $[C_2H_4]$ = 6670 ppm. RH = 18.8%.

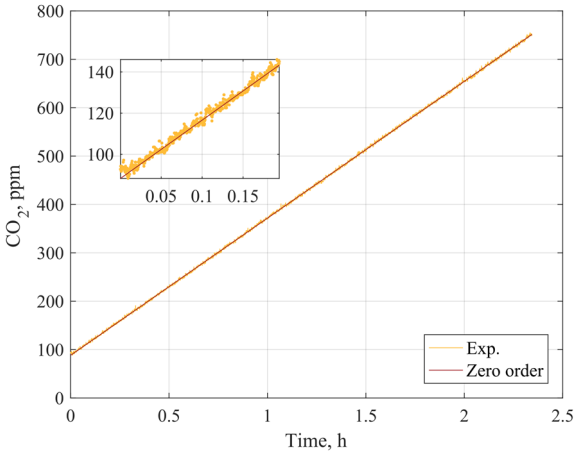

Figure A-7 Zero order rate law fit to experimental data 2. $[CO_2]_0$ = 92 ppm, $[C_2H_4]$ = 6670 ppm. RH = 18.8%.

Appendix D. Photoreactor Dimensions

All dimensions are given in mm and degrees.

Baffle

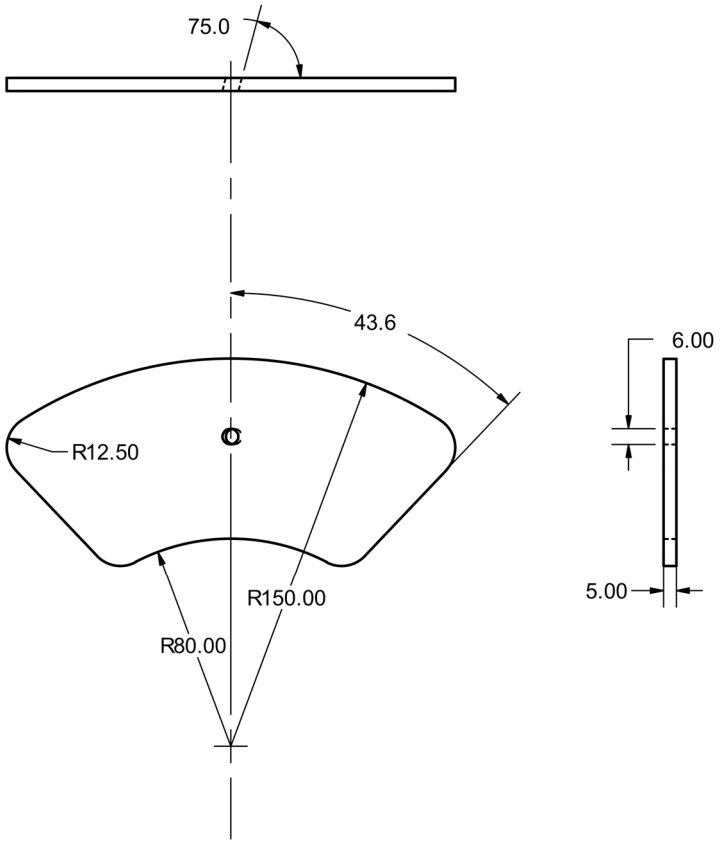

Figure A-8 Baffles used for prototype manufacturing.

Mesh

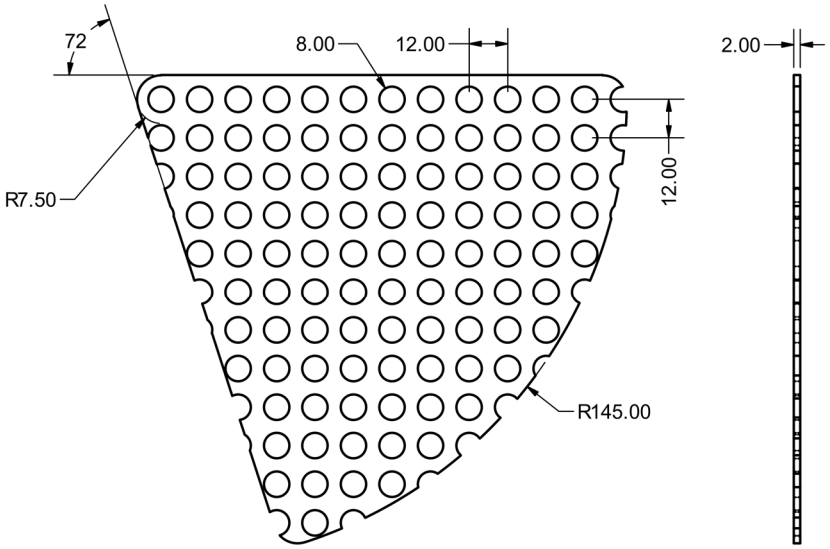

Figure A-9 Mesh element used for prototype manufacturing.

Support with threaded rods

Due to the limited space and inability of adding a proper technical drawing format, the geometry of the support and its corresponding dimensions will not be presented here. The interested reader is welcome to contact the author to obtain the technical drawings.

Appendix E. Prototype Degradation Curves

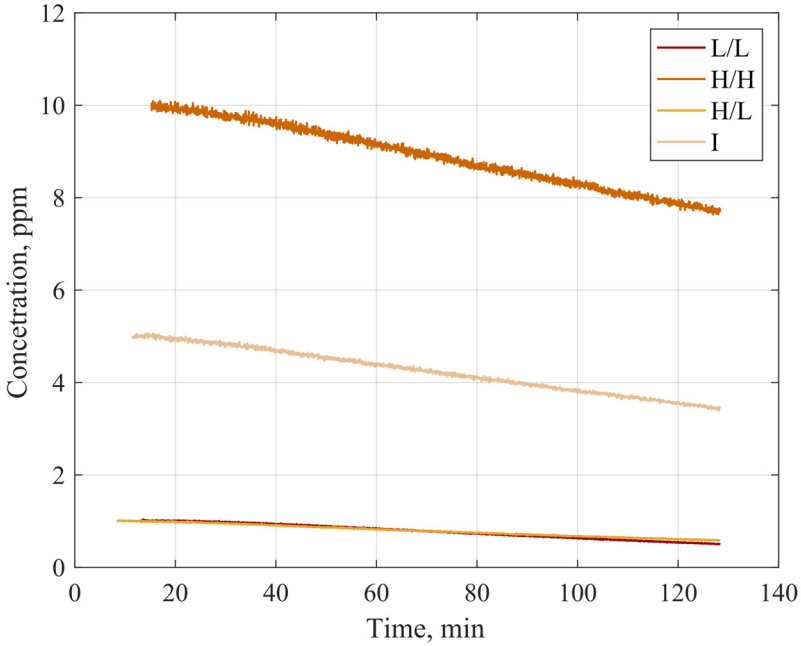

Figure A-10 Degradation curves obtained with the prototype. L/L - low flow and concentration; H/H - high flow and concentration; H/L - high flow and low concentration. I - intermediate flow and concentration.

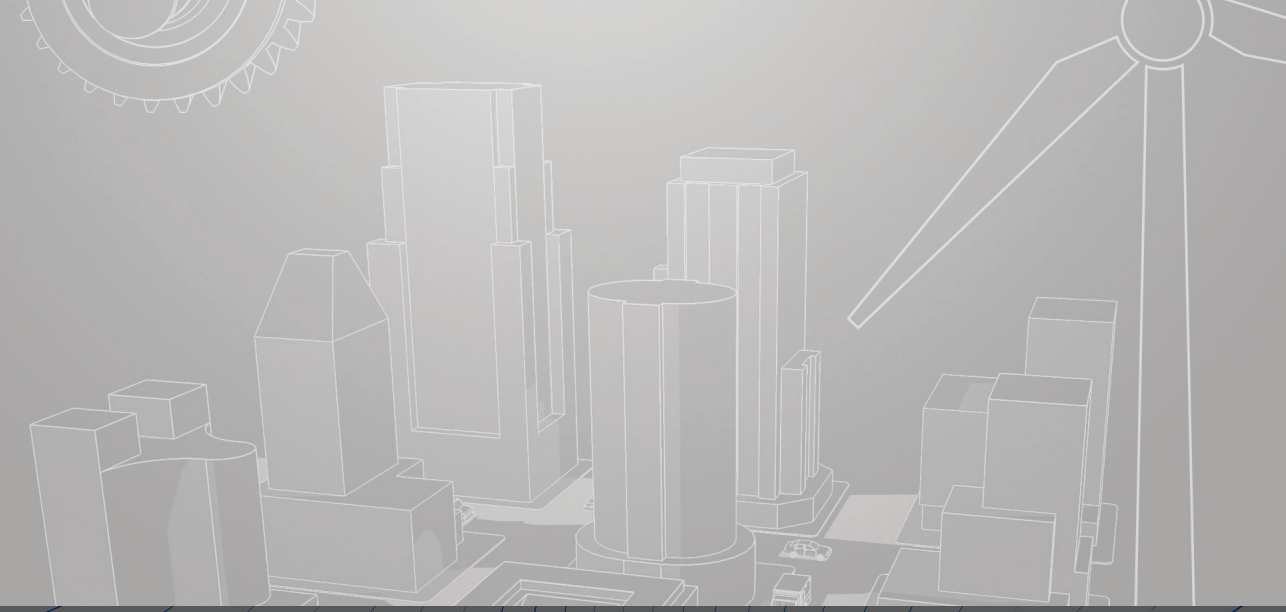

ISSN (online): 2446-1636
ISBN (online): 978-87-7210-589-5

AALBORG UNIVERSITY PRESS